CONTROLLED AGGREGATION OF GRAPHENE NANOSTRUCTURES USING NOVEL FUNCTIONALIZATION TECHNIQUES AND THEIR APPLICATION IN ELECTROCHEMICAL BIOSENSORS

A Thesis submitted
in partial fulfillment for the Degree of

Doctor of Philosophy

by

LAVANYA J

Department of Chemistry

INDIAN INSTITUTE OF SPACE SCIENCE AND TECHNOLOGY

THIRUVANANTHAPURAM

JUNE 2018

DECLARATION

I declare that this thesis entitled **Controlled aggregation of graphene nanostructures using novel functionalization techniques and their application in electrochemical biosensors** submitted in partial fulfilment of the degree of **Doctor of Philosophy** is a record of original work carried out by me under the supervision of **Dr. Gomathi N**, and has not formed the basis for the award of any other degree or diploma, in this or any other Institution or University. In keeping with the ethical practice of reporting scientific information, due acknowledgments have been made wherever the finding of others have been cited.

Lavanya J
SC12D005

Thiruvananthapuram-695 547
June 2018

ACKNOWLEDGEMENTS

This thesis is the summary of the past five years of my life, which is a journey consisting of patience and joy, profound knowledge and exciting achievements. The good fortune of working in my field of interest, the deep-rooted passion I acquired throughout these years gives me sense of satisfaction and happiness, for which I am fully indebted to Dr.N.Gomathi, my thesis supervisor, who inspires me in every way. Her scientific intuitions and firm belief influenced and helped me a lot to grow as an independent researcher at the end of this journey. She is always there when I need support in all matters relating to professional and personal life. I express my heartfelt gratitude for her guidance and encouragement, directed me to the successful completion of this thesis.

I extend my sincere gratitude to our Director Dr. V.K. Dhadhwal for providing me opportunity to work in the excellent ambience of IIST. I also thank with due regards the former Director, Dr. K.S. Dasgupta, Dr.Adimurthy, former Dean R & D, for his inspirational words when I first stepped to IIST as a student. I express my sincere gratitude to Prof. Kuruvilla Joseph, former HOD of Chemistry and Prof.Nirmala Rachael James, HOD, Chemistry for their readiness in finding solution for all our problems in the lab. I am very much indebted to my doctoral committee members for their critical and valuable suggestions. I render my thanks to the faculty members of Department of Chemistry and my fellow research students for their support. I appreciate staff members Jayasree L, Jayasree Dinesh, Bindu P C, Remya T, Mr. Loveson Albert and Mr. Sreekumaran Nair for helping me in every possible way.

My doctoral committee guided me through all these years. I thank all my doctoral committee members, Dr. S.Venugopal, Dr. S.Neogi, Dr. K.Srinivasan, Dr.S Anoop, Dr. Nirmala R James for their critical comments. I also thank all faculty members of the Department of Chemistry for their valuable guidance which enabled the successful completion of the research work.

I am thankful to Prof. S.Neogi, Department of chemical Engineering, Indian Institute of Technology, Kharagpur for providing the PECVD facility. I remember

with gratitude the warm hospitality rendered to me during my various visit to his lab. I am extremely thankful to SAIF, IIT Chennai for providing their facility for SEM analysis, Department of Aerospace, IIST for Raman and VSSC for XRD measurements, PSG College of Engineering, Coimbatore and NIIST, Thiruvananthapuram for TEM, IISc and AIMS for XPS analyses.

I remember with pleasure the time I spent with my fellow researchers who made my life at IIST pleasant and memorable. Special thanks to Nithyaa, Junior project fellow, Dr. Kiran and Dr. Linsha post-doctoral fellow for the fruitful discussions and healthy arguments. Special thanks to Arunmozhi, NIT Trichy who has been a pillar of support in all my hardships.

In no words I can express my gratitude for the love and care of my parents. I wish to thank them for their loving and patient support for all the endeavours in my life. Special thanks to my husband Mr.N Sathish kumar and my daughter S. Dhanshika who has been a pillar of support in all my joys, hardships and also for making my life more meaningful. Apart from them, I must acknowledge my main driving forces my brother, grandma, mother-in law and father-in law. Without my family, I would not have been able to preserve and accomplish this work.

(Lavanya J)

Abstract

Over past two decades, there has been an intense focus to understand and extend the technological boundaries of carbon-based nanomaterials such as graphene, carbon nanotubes and fullerene. Among these, due to the excellent electrical conductivity, tuneable band gap, fast electron transfer, facile synthetic routes, graphene have captivated the attention of electrochemical community. Despite the excellent properties, the restacking property of graphene limits its application. Although there was a substantial methods of functionalization, where functionalized graphene have scrutinized, there is still room for exploration. We have synthesised graphene *via* chemical method, functionalized by plasma functionalization method, and hybridized with nanomaterials, studied the electrochemical properties and demonstrated its biosensor applications for the detection of various bio analytes. The studies conducted using various forms of graphene given in this Thesis is briefed below.

Nitrite is an important molecule, which has both biological and environmental significance. An electrochemical sensor, which operates *via* direct electron transfer (DET) mechanism is explored for the nitrite detection using graphene functionalized by ammonia radio frequency (RF) plasma. Here, hemoglobin immobilized on functionalized graphene was used as the bioreceptor. The detection limit of this sensor system was 1.3 nM. Selectivity was demonstrated using other endogenous species like ascorbic acid, uric acid and hydrogen peroxide.

Hybridized graphene with enhanced surface area and excellent electrical conductivity was prepared by incorporating graphene nanoribbons (GNR) into graphene sheets (GS). A detailed microscopic, spectroscopic and surface area analysis confirms that the GNR was introduced into GS. A selective electrochemical sensor for the detection of ascorbic acid (AA) using GS/GNR was also accomplished with high sensitivity of 22 nA/μM cm^2 and detection limit of 230 nM.

The electrochemical performance of GS/GNR was enhanced by introducing nitrogen heteroatom *via* nitrogen/argon (N_2/Ar) RF plasma functionalization. N_2/Ar/GS/GNR has enhanced electrocatalytic activity and wide potential window

employed for simultaneous detection of ascorbic acid, dopamine and uric acid with well-resolved peak separation potential (ΔE_{AA-DA}= 220 mV, ΔE_{DA-UA}= 152 mV, ΔE_{AA-UA}= 372 mV). The detection limits of AA, DA and UA were estimated to be 5.3, 2.5 and 5.7 nM, respectively.

Nickel (Ni) nanoparticles with excellent electrocatalytic activity was incorporated into GS/GNR through chemical reduction method. A detailed characterization on crystallinity, morphology and spectroscopy confirms the incorporation of Ni into GS/GNR. Highly sensitive electrochemical sensor for the detection of glucose using Ni/GS/GNR was also accomplished at an applied potential of +0.5 V with a detection limit of 2.5 nM and sensitivity of 2.3 mA/mM cm^2.

Porous GNR, which increases rate of diffusion of ions, was synthesized by chemical etching of iron oxide nanoparticles. To enhance the electrochemical property and for providing an immobilization platform for biomolecules, porous GNR was electrochemically deposited by gold nanoparticles (AuNPs). Finally, a novel AuNPs/Porous GNR electrochemical immunosensor was fabricated to diagnose hepatocellular carcinoma with a wide range of linear response (0-60 ng/ml), detection limit (1 ng/mL), high sensitivity, good repeatability, and long-term stability.

GRAPHICAL ABSTRACT

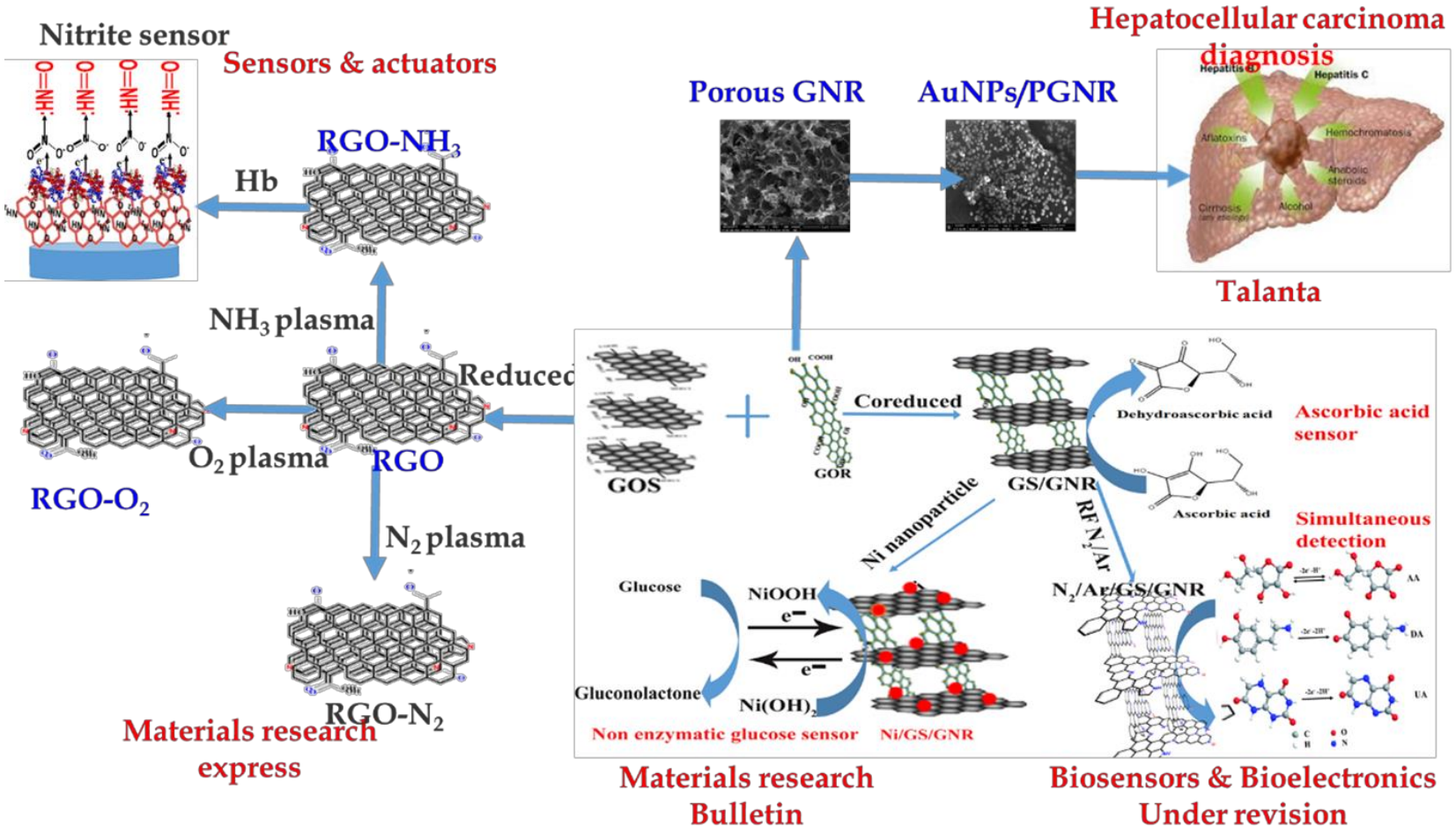

TABLE OF CONTENTS

LIST OF TABLES

ABBREVIATIONS

0D	Zero dimensional
1D	One dimensional
2D	Two Dimensional
3D	Three dimensional
AA	Ascorbic acid
AuNPs	Gold nanoparticles
Ar	Argon
BSA	Bovine serum albumin
BET	Brunauer-Emmet-Teller
BE	Binding energy
CE	Counter electrode
CME	Chemically modified electrode
CNT	Carbon Nanotubes
CVD	Chemical Vapour Deposition
RGO	Reduced graphene oxide
CV	Cyclic voltammetry
DA	Dopamine
DET	Direct electron transfer
DNA	deoxyribonucleic acid
DMF	Dimethylformamide
DPV	Differential pulse voltammetry
EC	Electrochemical
EDX	Energy Dispersive X-ray spectroscopy
EIS	Electrochemical Impedance Spectroscopy
FESEM	Field emission scanning electron microscopy
FTIR	Fourier Transform Infrared

GOS	Graphene oxide nanosheets
GS	Graphene nanosheets
GNR	Graphene nanoribbons
GCE	Glassy carbon electrode
GHz	Giga hertz
Hb	Hemoglobin
HOPG	Highly ordered pyrolytic graphite
HRTEM	High Resolution Transmission Electron Microscope
IHP	Inner Helmholtz plane
I_D	Intensity of D band in Raman spectrum
I_G	Intensity of G band in Raman spectrum
IR	Infrared
K	Kelvin
KE	Kinetic energy
LBL	Layer-by-Layer
LOD	Limit of detection
NIR	Near Infrared
OHP	Outer Helmholtz plane
PBS	Phosphate buffered saline
pH	Potential of Hydrogen
PVP	Poly vinyl pyrrolidone
RE	Reference electrode
RF	Radio frequency
RSD	Relative standard deviation
SAED	Selected area diffraction pattern
SEM	Scanning electron microscopy
TEM	Transmission Electron Microscope

UA	Uric acid
UV	Ultraviolet
Vis	Visible
WE	Working electrode
XPS	X-ray Photoelectron Spectroscopy
XRD	X-ray Diffraction

LIST OF FIGURES

NOTATIONS

λ	Wavelength
Å	Angstrom
D	Crystal lattice spacing
Θ	Angle of diffraction
c	Velocity of light
H	Planck's constant
A	transfer coefficient
T	Transmittance/Temperature
V	Voltage
E^0	Formal potential
R	Universal gas constant
F	Faraday constant
J	Flux
D	Diffusion coefficient
Z	Ionic charge
∅	Potential
i	Current
A	Surface area of the working electrode
C	Concentration of the electrolyte
V	Scan rate
I_p	Peak current
$I_{p,ox}$	Oxidation peak current
$I_{p,red}$	Reduction peak current
$E_{p,ox}$	Oxidation potential
$E_{p,red}$	Reduction potential
Φ	Phase shift
Z	Impedance
Z'	Real
Z''	Imaginary

R_p	polarization resistance
R_s	Solution resistance
R_{ct}	Charge transfer resistance
Z_w	Warburg impedance
β	full width half maximum

CHAPTER 1

INTRODUCTION

This chapter focusses on studies on synthesis, properties, functionalization and application of graphene nanosheets and graphene nanoribbons in the field electrochemical biosensor. It also demonstrates the overview of biosensor and presents a detailed study on the fundamentals of electrochemical process. Finally, it elucidates the scope and structure of the thesis.

1. Background

"Carbon" the most interesting material in the periodic table, has ability to form a variety of stable materials with different hybridizations namely, sp, sp^2, sp^3-hybridized bonds. The catenation property of carbon allows it to form a stable frameworks of allotropes, comprising charcoal, graphite, carbon fibers and diamond as well as newly discovered carbon based nanomaterials, such as graphene nanosheets (GS), fullerene, carbon nanotube (CNT) and graphene nanoribbons (GNR). Each individual carbon allotrope has innumerable excellent physical and chemical properties and thus fuel an enormous research interest in wide range of applications with interdisciplinary approach, especially in the field of electrochemical application from electroanalysis to energy conversion. Among them, GS and its derivatives, such as graphene oxide nanosheets (GOS), GNR and functionalized GS and its derivatives have been, and continue to play a major focus in the area of materials science research (Novoselov et al., 2004).

1.1 Graphene nanosheets

GS, a two-dimensional (2D) nanostructured material consists of sp^2 hybridized carbon atoms organized in a hexagonal pattern with a carbon-carbon distance of 1.42 Å and interlayer spacing of 3.4 Å (Meyer et al., 2007). This material can be considered as the basic structural element of other allotropes of carbon, like three-dimensional (3D) graphite, one-dimensional (1D) CNT and zero-dimensional (0D) fullerenes (Figure 1.1) (Pumera, 2009). Graphite, a 3D layered material, consists of carbon atoms, arranged in a honeycomb lattice, bonded by weak van der Waals interactions. A tubular-shaped carbon nanomaterial, with various boundaries results in 1D CNT of fluctuating chirality. The wrapping of GS, introducing curvature in

terms of intruding five membered rings leads to fullerene (Geim & Novoselov, 2007).

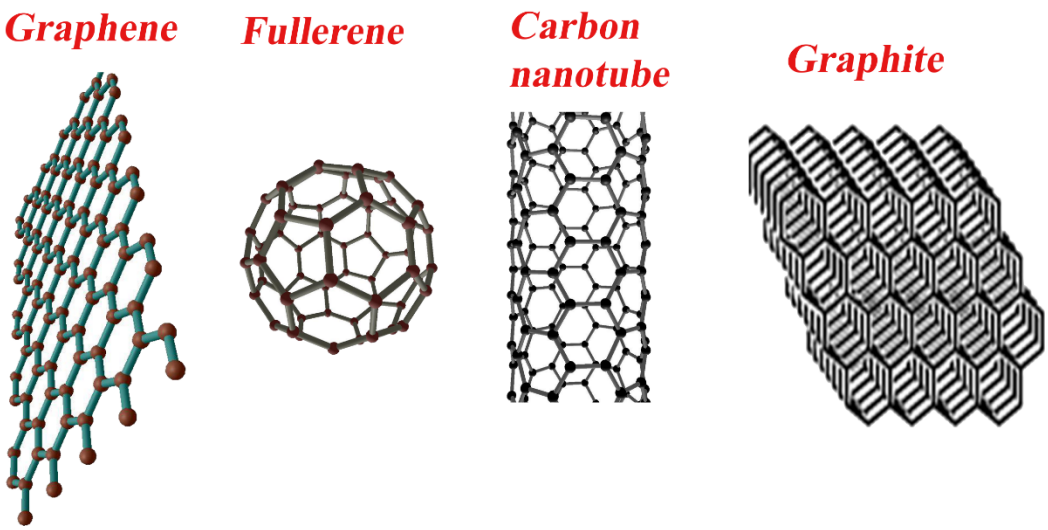

Figure 1.1 Structure of some representative carbon allotropes

Unlike other carbon allotropes, GS, a band gapless semiconductor, is the strongest and thinnest material reported up to now. Such a wondrous material with outstanding properties has been theoretically investigated since 1940s, but Landau and Peierls strictly claimed that 2D nanomaterial were too thermodynamically unstable to exist in the real world (Wallace, 1947). This argument was also supported by Mermin and Wagner with their theory revealing that the long-range interactions of crystal in $d \leq 2$ dimensional systems would be undermined by the surface fluctuations. But these outcomes didn't stop the scientists from exploring the GS. In 1947 Wallace predicted the electronic structure of GS, and McClure deduced the corresponding wave function equation in 1956. At last it was experimentally proved in 2004, by Geim and Novoselov *via* mechanical exfoliation of highly oriented pyrolytic graphite (HOPG).

The "thinnest" known material GS with a long range π- conjugate exhibits fascinating properties for instance large specific surface area (2630 m^2g^{-1}) greater than graphite (10 m^2g^{-1}) and CNT (1315 m^2g^{-1}) (Pumera, Šmíd, & Veltruská, n.d.), mechanical strength (1 T Pa) which is 200 times larger than steel, electrical conductivity which is 60-fold superior than single-walled CNT (SWCNT) and six orders of magnitude larger than copper (C. Liu, Alwarappan, Chen, Kong, & Li, 2010)(Xuan Wang, Zhi, & Müllen, 2008), extraordinary electronic properties with

high charge carrier mobility (230,000 $cm^2V^{-1}S^{-1}$) at room temperature, remarkable optical transparency of 97.7 % and excellent thermal conductivity (5000 W m^{-1} K^{-1}) (Sato, Harada, Kondo, & Ohfuchi, 2010),(Novoselov et al., 2012).

1.2 Graphene nanoribbons

Though GS behaves as a zero band gap semiconductor, it is indeed possible to control the electronic properties by introducing energy gap in GS through finite termination of GS to quasi one dimensional ribbon like structures commonly referred to as graphene nanoribbons (GNR) (M. Y. Han, Özyilmaz, Zhang, & Kim, 2007). GNR is a quasi 1D nanostructured stripes of GS with hexagonal carbon lattices and with ultrathin width (<50 nm) (Tejeda, 2016). This carbon based nanomaterial was theoretically explored by Nakada et al in 1996 i.e before the discovery of GS by Geim. Owing to the discrepancy in dimension and morphology, GNR with large amount of edge defects, are expected to possess distinctive structural and unique physico-chemical properties, which are quite different from CNT and GS. As a quasi 1D nanostructures, GNR are highly stable and maintain their high electrical conductivity. And it possesses two different possible edge geometries, namely zigzag and armchair, which are termed as zigzag graphene nanoribbons and armchair graphene nanoribbons, respectively and show very unique electronic properties arising from their contrasting boundary conditions (Dutta & Pati, 2010; Pacchioni, 2017). After the discovery of GS, different methods have been developed for synthesizing GS and its related materials. So, as a first step of this chapter, we discuss the existing methods of synthesizing GS and GNR by chemical and physical means.

1.3 Synthesis of graphene based nanomaterials

Synthesis of GS was attempted by B. Lang *et al*. in 1975 who demonstrated the growth of single and many-layered graphite through thermal decomposition of carbon on Pt substrates *via* chemical decomposition method (Lang, 1975). But due to insufficient results it was not designated as GS. After a long gap, Ruoff and co-workers in 1990 made an attempt to separate thin graphitic flakes on SiO_2 substrates *via* mechanical scrubbing of patterned islands on HOPG. This was followed by using a similar method by Geim and Novoselov, later achieved in 2004 through micromechanical cleavage, also known as micromechanical exfoliation, generally

denoted as “Scotch-tape method”. This method involves constant peeling off GS layers from HOPG by the help of an adhesive tape to give single GS layers, which can be transferred successively onto a suitable surface (e.g., SiO_2 wafers) through a wet or dry transfer technique (Novoselov et al., 2004).

Though, the above mentioned method gives the best quality GS, for bulk production, for the past few years, various other techniques have been established. GS can be synthesised by two different types of broad category *i.e* top-down method and bottom-up method (Edwards & Coleman, 2013). An outline of various techniques for the synthesis of GS is illustrated in the flow chart in Figure. 1.2.

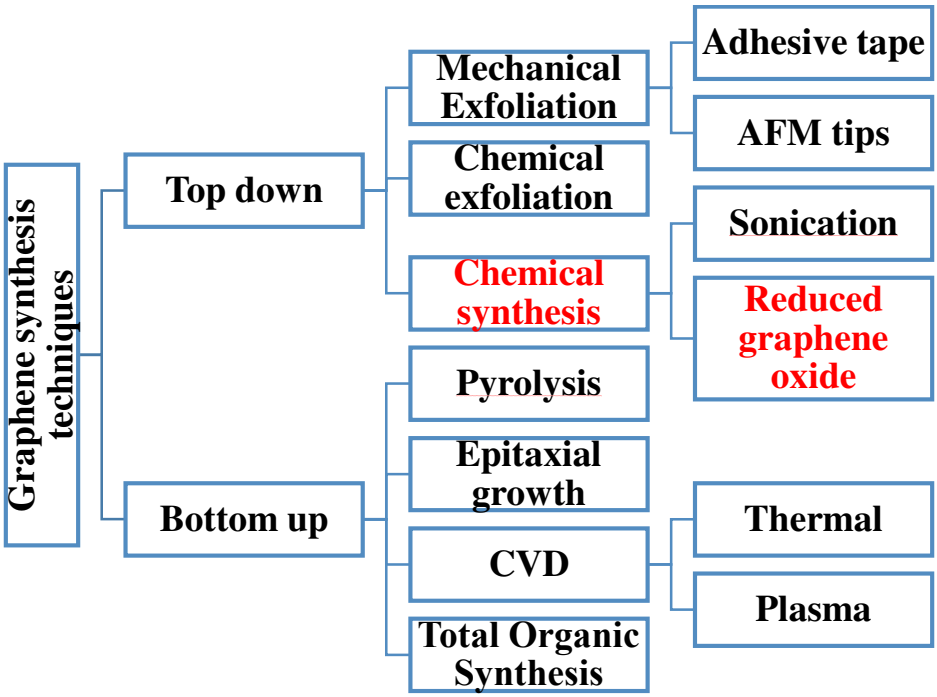

Figure 1. 2 A process flow chart of GS synthesis.

In contrast to pure GS, GS synthesized from chemical reduction method is strongly oxygenated with various functional groups like hydroxyl and epoxy on the basal planes, carbonyl and carboxyl groups on the edges of the GS. The presence of these functional groups makes GS more hydrophilic and more reactive with the environment. GS produced through reduction of graphene oxide nanosheets (GOS) displays a wrinkled structure with many lattice defects, which is different from the rippled structure observed in pristine GS. Compared to pure GS, GS and its derivatives synthesized from chemical reduction method possess more advantageous electrochemical property (Brownson & Banks, 2010). Therefore in

this thesis, among the aforesaid method, we have chosen to briefly study the most commonly employed synthesis methods namely synthesis of GOS, chemical reduction of GOS and unzipping of CNT.

1.3.1 Synthesis of graphite oxide

Graphite oxide is the basic material for the preparation of GS in bulk quantities (Park & Ruoff, 2009). Graphite oxide comprises of layered graphitic structure, with oxygen-containing groups, which not only increase the interspacing distance between the layers, but also make the material more hydrophilic. This graphite oxide can generally be synthesized by means of oxidation based on different methods including Brodie (Brodie, 1859), Staudenmaier (Staudenmaier, 1898), Hummers (Hummers & Offeman, 1958), improved Hummers and improved synthesis method (Marcano et al., 2010) (Figure 1.3) using various oxidants such as concentrated sulfuric acid, nitric acid, ortho phosphoric acid and potassium permanganate. As a result of ultrasonication, layered structured graphite oxide gets exfoliated to few layered material named GOS.

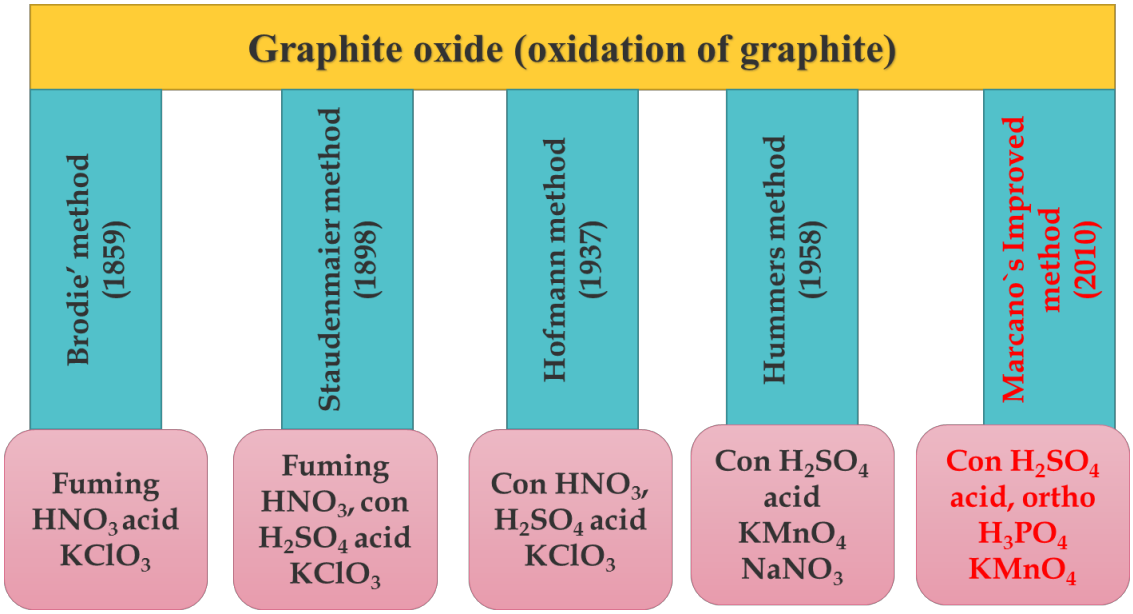

Figure. 1.3 Methods for synthesis of graphite oxide using graphite, acids and oxidizing agents.

Though, GOS has been well established, the exact chemical structure of it is still not well-defined. Due to the structure deformation during oxidation, the GOS with heavily decorated oxygen functional groups, consists of partly tetrahedrally

arranged sp^3 hybridized carbon atoms, which are dislocated slightly above or below the GS plane.

In terms of electrical conductivity, GOS is often described as an electrical insulator, due to the disruption of its sp^2 bonding networks with a sheet resistance of about 10^{12} Ω /sq or higher (Becerril et al., 2008; J. Zhao, Pei, Ren, Gao, & Cheng, 2010). The oxygen groups and lattice defects alter the electronic structure of GS and serve as strong scattering centres, which affect the electrical transport. So, the reduction of GOS is not only essential in removing the oxygen-containing groups bonded to the GS, but also to recover the electrical conductivity and other properties of GS (Pei & Cheng, 2012).

1.3.2 Synthesis of reduced graphene oxide (RGO)

At present, preparation of GS *via* chemical method using graphite as the precursor material is considered as one of the cost-effective method for the synthesis of GS without compromising its surface and electrical properties (Stankovich et al., 2007). This technique initially starts with oxidation of graphite to graphite oxide, followed by subsequent exfoliation of graphite oxide to GOS and further, reduction of GOS by using various reducing agents, including hydroiodic acid, sodium borohydrate, ascorbic acid and hydrazine hydrate (Fernández-Merino et al., 2010; Pei & Cheng, 2012; Pei, Zhao, Du, Ren, & Cheng, 2010; Shin et al., 2009). Since, the complete reduction has not yet been achieved, the obtained nanosheets was termed as RGO rather than "GS". The reduction can be performed through several other routes such as thermal (McAllister et al., 2007), solar (Mohandoss, Gupta, Nelleri, Pradeep, & Maliyekkal, 2017), chemical (Chua & Pumera, 2014), hydrothermal (Zheng et al., 2017), electrochemical etc (Ramesha & Sampath, 2009; M. Zhou, Wang, et al., 2009).

RGO based materials contain residual amount of oxygen and hydroxide functional moieties and certain amounts of defects on both basal and edges. The presence of these structural and functional defects in the RGO plays an important role in the field of electrochemical sensors, which enhance the rate of electron transfer and make the adsorption, pre-concentration of the electroactive species easier and it can effectively catalyse the redox reactions. Moreover, the presence of these defects enhances the chemical reactivity of RGO and provides an effective

functionalization platform for incorporation of various functional groups, which can enable the application of these excellent materials for electrochemical sensor with specific analytes (Punckt, Pope, Liu, & Aksay, 2016).

1.3.3 Synthesis of GNR

GNR can be synthesized by top–down or bottom–up approaches. As illustrated in Figure 1.4, it can be obtained by longitudinally unzipping CNT using gas-phase oxidation followed by sonication (Jiao, Wang, Diankov, Wang, & Dai, 2011), chemical attack by H_2SO_4 and $KMnO_4$ (Higginbotham, Kosynkin, Sinitskii, Sun, & Tour, 2010), lithium intercalation (Cano-Márquez et al., 2009), catalytic cutting by metal nanoparticles (Campos, Manfrinato, Sanchez-Yamagishi, Kong, & Jarillo-Herrero, 2009), plasma etching of CNT, which is partially embedded in a polymeric matrix (Jiao, Zhang, Wang, Diankov, & Dai, 2009), cutting by hydrogen (Talyzin et al., 2011), electrochemical unzipping (Shinde, Debgupta, Kushwaha, Aslam, & Pillai, 2011) and electrical unwrapping (Kim, Sussman, & Zettl, 2010), or laser cutting (P. Kumar, Panchakarla, & Rao, 2011).

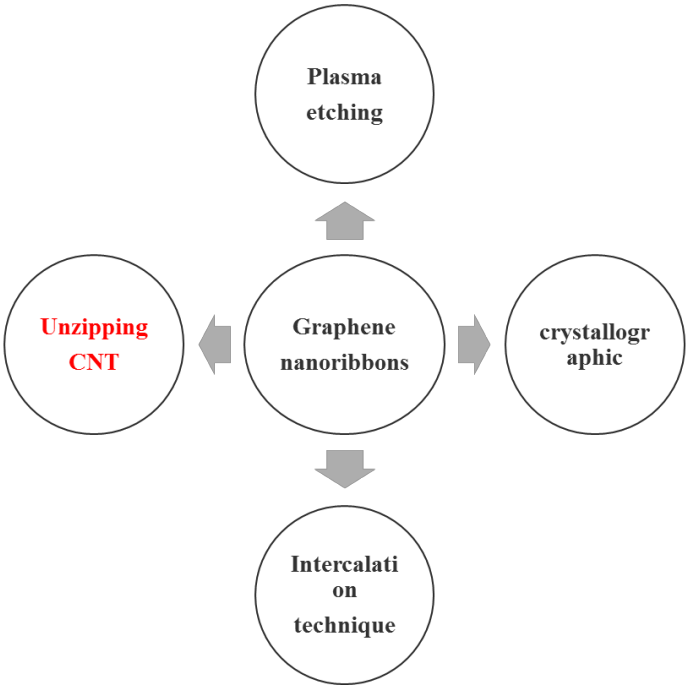

Figure 1.4 Synthesis of graphene nanoribbons

Alternatively, GNR can be produced by template growth on SiC (Sprinkle et al., 2010), surface-assisted bottom-up synthesis (H. Huang et al., 2012), or top-down lithographic fabrication (Zhihong Chen, Lin, Rooks, & Avouris, 2007). In this thesis, among the aforesaid methods, we reported a procedure for production of

large quantity of single and few layer GNR, through longitudinal unzipping of CNT. It was found that GNR obtained from CNT possesses straight edges and high aspect ratios.

1.4 Electrochemical property of GS and GNR

1.4.1 GS

Despite the fascinating properties of GS, the wide electrochemical potential window (M. Zhou, Zhai, & Dong, 2009), remarkable electron transport property and the oxygen moieties on GS and GNR make it a potentially useful electrode material in electrochemical biosensors. Besides, the large surface area along with high density edge-plane defect sites on these materials, provides numerous electrochemically active sites (Artiles, Rout, & Fisher, 2011), which enhance the adsorption and desorption of biomolecules, and as a result the performance of electrochemical biosensors can be enhanced. Furthermore its excellent electrical conductivity along with a zero band gap enhances its direct electron transfer (DET) between biomolecules and surface of the electrode (X.-H. Zhou, Liu, Bai, & Shi, 2013). Also, GS can interact with biomolecules easily by π-π stacking and hydrophobic interactions with negligible noise ratio.

In comparison with CNT, GS and GNR have many advantages, that is, these carbon based nanomaterials do not contain metallic impurities, which interfere with the material electrochemistry, and bulk quantities of GS with high surface area can be produced at low cost (Segal, 2009).

Surprisingly, high quality GS synthesized *via* CVD or mechanical exfoliation method are found to be not beneficial for electrochemical application (Brownson, Munro, Kampouris, & Banks, 2011). Various chemical methods are available for producing bulk quantities of GS, among them GS synthesized through chemical reduction of GOS are highly beneficial for electrochemical application. The defects in the form of various oxygen-containing functional groups like carboxyl, hydroxyl, or epoxy groups, alter the local density of electronic states and thereby can enhance the adsorption of the electroactive species and catalyze the electrochemical reactions. Furthermore, these functional groups act as anchoring sites for various biomolecules for biorecognizing the bioreceptor (Y. Wang, Li, et al. 2011). These excellent properties enable RGO as a potential electrode material for

electrochemical biosensors. In 2009 Zhou et al reported, GS synthesized from chemical reduction of GOS exhibits a wide electrochemical potential window of ca. 2.5 V in 0.1 M PBS (pH 7.0), lower charge-transfer resistance and very fast electron transfer rate, which are comparable to that of graphite and glassy carbon electrode (GCE) (M. Zhou, Zhai, et al., 2009)(Brownson & Banks, 2010).

1.4.2 GNR

The one dimensional nanostructured material GNR, obtained by unzipping of CNT has excellent properties like, non-zero band gaps, high length-to-width ratios and more reactive edges, which enhances the electrocatalytic property towards the molecules. In comparison with CNT and GS, GNR with reactive edges can increase the adsorption and electrocatalysis of certain molecules and provides large surface area for the loading of significant aromatic molecules *via* $\pi - \pi$ stacking interaction, or electrostatic or hydrogen bond interactions. Moreover, the open-ended graphene sheets improve the reactivity of GNR. Thus, GNR with such fascinating properties can act as a potential electrocatalytic material for preparation of electrochemical biosensors (S. Zhang, Tang, Lei, Dong, & Ju, 2011), (X. Huang et al., 2015).

1.5 Application of GS and GNR in electrochemical biosensor

Due to unique properties including excellent electrical conductivity, large surface area, large potential window, minimum charge-transfer resistance, fast electron transfer rate and excellent electrochemical activity, functionalized GS and GNR have potential application in the field of biosensors for the diagnosis of various deadly diseases at the earlier stage (Ambrosi, Chua, Bonanni, & Pumera, 2014; Pumera, 2009, 2013). The current section will discuss the application of GS and GNR in field of biosensors. The concept of biosensor was introduced by the pioneering work of Professor L C. Clark, in 1956, who invented the first oxygen sensor and later on in 1962 the first biosensor, a glucose sensor based on enzymatic amperometric technique (Clark & Lyons, 1962). The term biosensor can be defined as “a self-contained integrated device that is capable of providing specific quantitative or semi-quantitative analytical information using a biological recognition element (biochemical receptor), which is retained in direct spatial contact with a transduction element".

A biosensor must possess some of the following important characters:

- The biosensor must be highly specific to analyte, should be stable under normal storage conditions.
- The reaction should be independent of physical parameters such as stirring, pH and temperature.
- The output of the biosensor should be accurate, precise, reproducible and linear over the suitable concentration range. Especially it should be free from electrical noise.
- The biosensor device should be cheap, small, portable and capable of being used by semi-skilled operators.

Biosensor is usually composed of two main components: a bioreceptor and a transducer. The bioreceptor specifically recognizes the target analyte and translates information from the bio-recognition signal into a chemical or physical output signal, whereas the transducer converts the signal into a measurable signal. Depending upon transducer, biosensor can be classified into several types, for instance, thermal, optical, piezoelectric, calorimetric, electrochemical etc (Mehrotra, 2016). Compared to other analytical techniques, electrochemical is more powerful and versatile technique, which offers high sensitivity, selectivity, rapid response, accuracy and precision as well as a large linear dynamic range, ability to operate in turbid solutions and is flexible to miniaturization (Singh et al., 2013). Over past few decades many electrochemical biosensor have been developed to detect nucleic acids, proteins, and small molecules. Electrochemical methods are robust and can accurately detect biomarkers in complex sluggish heterogeneous biological samples. Electrochemical biosensors have been applied to many cancer and infectious disease biomarkers which have illustrated the utility of electrochemical biosensors for future medical diagnostic applications (Peng, Zhang, Soeller, & Travas-Sejdic, 2009), (Ahirwal & Mitra, 2010) &(Shiping Song, Wang, Li, Zhao, & Fan, 2008).

1.6 Electrochemical biosensor

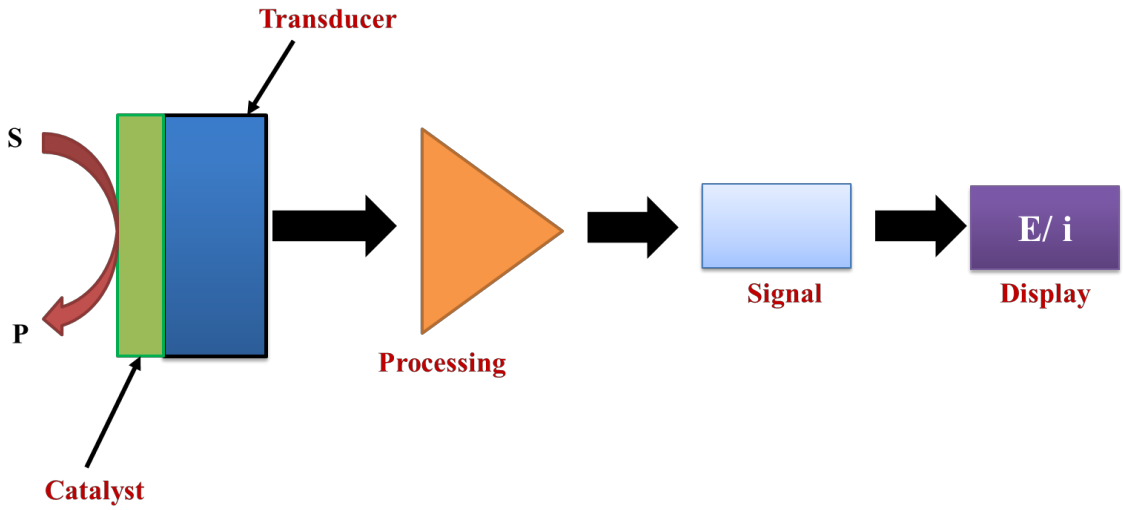

Figure 1.5 Flowchart of electrochemical sensor

Electrochemical biosensors is a biosensor that transforms biochemical information such as analyte concentrations into an analytically useful signal: current or voltage (Figure 1.5). This type of sensor does not require a separate transduction element. It directly detects the concentration of the analyte from the measured electrical response proportional to the analyte concentration obtained from the electrode. Based on their operating principle, the electrochemical biosensors may be further classified into voltammetric/amperometric, potentiometric, and impedimetric biosensor. Voltammetric biosensors are the principal class of electrochemical biosensor in which the data is obtained in the form of current obtained as a result of electrochemical oxidation or reduction of an electroactive species with respect to the applied potential. The corresponding oxidized or reduced current is proportional to the concentration of the analyte of interest. In amperometric biosensors there is no change in the potential, a fixed potential is applied, and the resultant change in current is typically expressed as a function of time. In the case of impedimetric biosensors, a small alternating potential is applied between the working and reference electrodes (e.g. ±5 mV) and the resultant impedance implies the interaction between the bioreceptor element and the target analyte. Where the impedance measurements are based on the ratio between the resultant current from the bioreceptor-analyte interaction and the applied voltage. Potentiometric biosensors measure the potential difference between the working electrode and a

reference electrode at zero current. It typically employs a two electrode system, comprised of an ion-selective electrode (the working electrode) and a reference electrode (Grieshaber, MacKenzie, Vörös, & Reimhult, 2008; Hammond, Formisano, Estrela, Carrara, & Tkac, 2016; Thévenot, Toth, Durst, & Wilson, 2001).

Among these, voltammetric sensors are the most commonly used technique. A special case of voltammetric sensor is the amperometric sensor where a fixed potential is applied and the current response is measured. The current response is directly proportional to the number of electrons transferred, which implies, the concentration of the electroactive species (Brett and Brett, 1998). The electrochemical cell used for voltammetry usually consists of a three electrode systems comprised of a working (WE), auxiliary/counter (CE) and reference electrode (RE) in contact of an electrolyte solution (Figure 1.6).

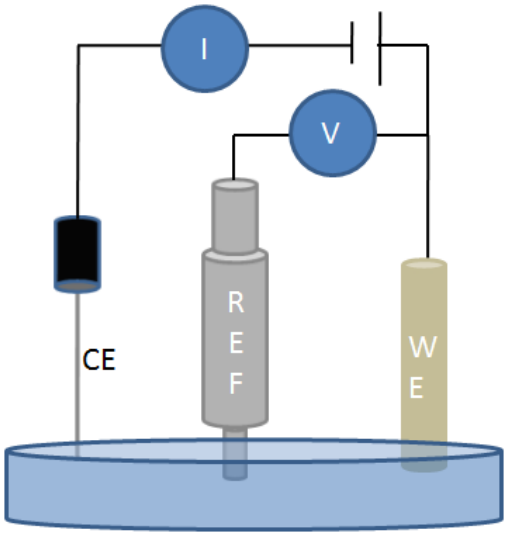

Figure 1.6 Three electrode electrochemical cell

The WE, referred as chemically modified electrode (CME) can be considered as the most important electrode because electrochemical reactions of interest occur on the surface of this electrode, where the receptor is immobilized and all the interactions with the analyte occur. The purpose of the counter electrode (CE) is to complete the circuit to measure current. Counter electrode is generally made of an inert and strong material, which is usually platinum or carbon. The RE is an electrode which has a stable and well known electrode potential. Its potential should not vary when an external potential is applied in the working electrode and must be insensitive to

the composition of the analyte solution. The most commonly used materials for each electrode type is presented in Table 1.1.

In this thesis all the electrochemical measurements are performed in a three electrode system consisting of the working electrode, counter electrode (Pt wire) and RE Ag/AgCl in 0.1 M KCl, which has a fixed potential of + 0.197 V vs. NHE at 25 ^{0}C , where its potential was maintained constant throughout the measurement. All the three electrodes are dipped into a sluggish solution consisting of excess amount of inert salt, called supporting electrolyte.

Table 1.1 Commonly used materials for the electrodes that comprise a typical three-electrode electrochemical system

Electrode	Commonly used materials	Key material requirements
Working	Gold, silver, platinum, carbon (a range of different types including GS, glassy carbon)	Chemically inert, chemical structural properties specific to biosensor ,chemical and/or biological binding
Counter	Gold, platinum, carbon	Chemically inert
Reference	Silver/Silver Chloride, saturated calomel electrode	Provide a stable electrode Potential

1.7 CME

Working electrode materials (the key component) play an important role in constructing high performance electrochemical sensor. The surface of this electrode is modified to enhance the properties of electrochemical sensor, which are either not possible or difficult to achieve using conventional electrodes. Enhancement in electrochemical properties include increased selectivity, sensitivity, chemical and electrochemical stability, as well as a larger usable potential window and improved resistance to fouling.

Hence, CME is a conducting or semiconducting material that has been coated with a conventionally available working electrode, which alters the electrochemical properties of the interface. One of the most important properties of CME is their ability to catalyze the oxidation or reduction of solute species that exhibits high

over voltages at unmodified surfaces. Thus CME plays an important role in reducing the high overvoltage required for the voltammetric determination of analyte without its major interferences (Foss Jr. & Martin, 1994). Various nanomaterials such as GNS, GNR, Nickel (Ni) nanoparticles, gold nanoparticles (AuNPs), polymer films, etc, can used for the modification of electrode surface. For the present study, the modification techniques are based on the modification of GNS, GNS/GNR and GNR (will be discussed in coming Chapters).

1.8 Fundamentals of electrochemical process

In electrochemical biosensor, the transfer of electrons takes place at the interface between an electrode and an electrolyte during reduction/oxidation (redox) reactions. The flow of electrons between them are measured in the form of current. A current in which electrons cross the interface from the electrode to the analyte in solution is a cathodic current, while electrons flow from the analyte into the electrode is an anodic current (Bard & Faulkner, 2015).

1.8.1 Electrode/Solution Interface

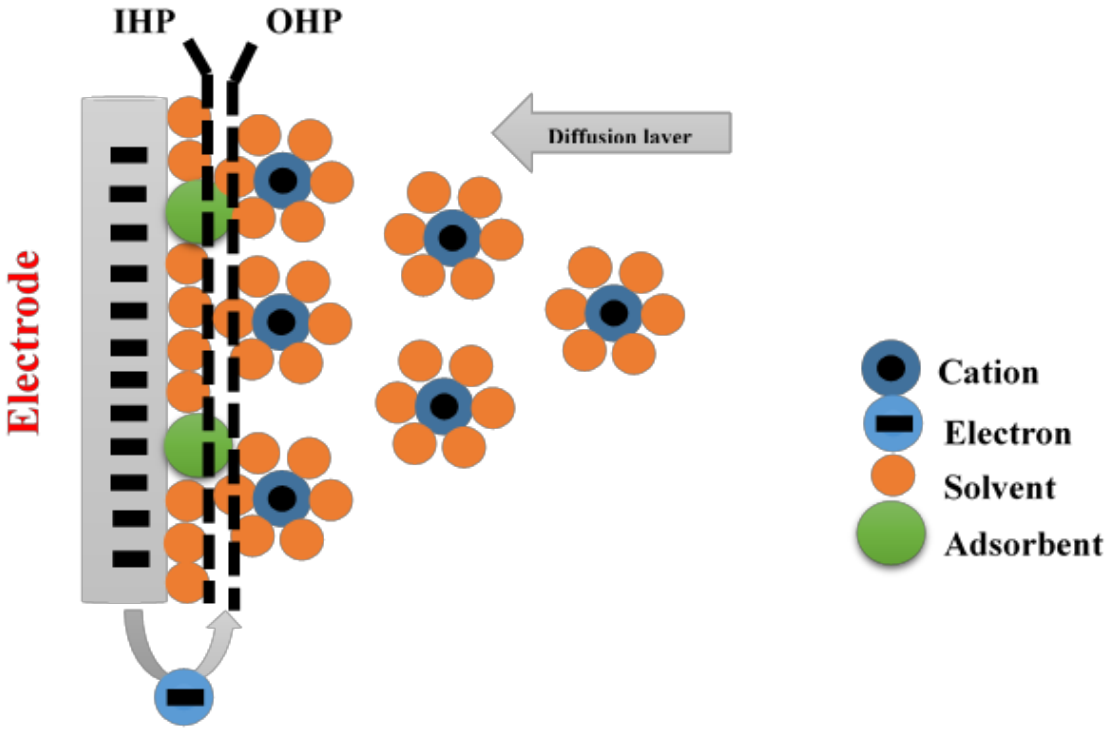

Figure 1.7 Electrical double layer model under conditions where anions are specifically adsorbed.

The strong interactions between the molecules in solution and the electrode surface result in the formation of the electrical double layer and is characterised by a double

layer capacitance. The model of the double layer is shown in Figure 1.7. The double layer model is thought to be made of several "layers" where the layer closest to the electrode, called the inner layer, contains solvent molecules and species that are specifically adsorbed. This inner layer is also called the compact, Helmholtz or Stern layer. The inner or Helmholtz layer itself is then divided into the Inner Helmholtz Plane and the Outer Helmholtz Plane as shown in Figure 1.7. Specifically adsorbed ions appear in the IHP, while solvated ions closest to the electrode plane are in the OHP. The non-specifically adsorbed ions spread in a diffuse layer is located between OHP and the bulk solution. The thickness of the diffuse layer depends on the total ionic concentration in the solution. In most cases, the charging current generated by the double layer is negligible compared to the current generated by faradaic processes. However, at low concentrations of electroactive species, the charging current can be much larger than the faradaic current for the reduction or oxidation reaction (Stojek, 2010).

1.8.2 Interpreting electrochemistry

In a typical voltammetric electrochemical biosensor, the electrochemical process as expressed in equation (1.1) involves the transfer of electron across the interfacial region between WE and a solution phase species. The charge transfer leads to both faradaic and non-faradaic components. The faradaic component arises from the electron transfer *via* a reaction (1.1)

$$O + ne^- \leftrightarrow R \longrightarrow \quad (1.1)$$

where O and R are the oxidised and reduced forms of the redox couple, respectively, and n is the number of electrons transferred in the reaction. The electron transfer reaction occurs across the interface by overcoming an appropriate activation barrier, namely the polarization resistance (R_p), along with the uncompensated solution resistance (R_s). The non-faradaic current results from charging the double-layer capacitor.

The potential of the electrode is related to the standard potential of the redox couple and the activities of the species involved in the conversion and is given by the Nernst equation 1.2:

$$E = E^0 + \frac{RT}{nF} ln \frac{a_{ox}}{a_{red}} \longrightarrow \quad (1.2)$$

where E is the equilibrium potential, E^0 is formal potential and a_{ox} and a_{red} are the concentrations of the oxidized and reduced species at the electrode surface. R is the universal gas constant (8.314 J K^{-1} mol^{-1}), T is the temperature (in Kelvin), n is the number of electrons transferred in the reaction and F is the Faraday constant (96,485.33 C mol^{-1}).

When the potential is applied to the electrodes the following reactions take place:

- Reactant moves to the interface.
- Electron transfer can then occur *via* quantum mechanical tunnelling between the WE and reactant close to the electrode.
- The product moves away from the electrode to allow fresh reactant to the surface.

Thus, the overall response is termed as mass transport of the electroactive species (Bard & Faulkner, 2015).

1.8.3 Mass transport limited reactions

In electrochemical reactions the transfer of electron is limited by three modes of mass transfer:

- Migration: movement of electrons driven by an electric field
- Diffusion: random motion of analyte driven by a concentration gradient
- Convection: motion of particles caused by physical (solution) movement

A mass transport phenomenon is described by flux (j), which can be defined as the rate of molecules flowing across an area per unit time. When all three modes of mass transport occur in a given system, flux can be calculated using Nernst – Planck equation, which is an extended version of Fick's Law by a component representing particles movement as a response to electrostatic force (second term in the equation 1.3). In one dimension this is:

$$J(x,t) = -\frac{D\partial C(x,t)}{\partial x} - \frac{zFDC}{RT}\frac{\partial \emptyset(x,y)}{\partial x} + C(x,t)V(x,t) - - - -\rightarrow (1.3)$$

where D is the diffusion coefficient (m^2 s^{-1}), C is the bulk concentration (mM), z is the ionic charge of the electroactive species, $\emptyset$ is the potential and V is the hydrodynamic velocity. Usually in electrochemical measurements the potential gradient is kept at minimum by providing an excess of the supporting electrolyte,

hence the second term of the equation can be neglected. Moreover, the experiments are often carried out without any convection (i.e. stirring or flow of the solution), which is represented as the last term in the above equation (1.3), in which case it can be also neglected. In such simplified experimental conditions, the flux is dependent on the concentration gradient and can be calculated from equation (1.4):

$$J(x,t) = -\frac{D\partial C(x,t)}{\partial x} - - - - - - - - (1.4)$$

Since the current (i) is directly proportional to the flux, as shown below:

$$i = -nFAJ - - - - - - (1.5)$$

the current response of an electrochemical system can be calculated from the equation (1.6):

$$i = nFA\frac{D\partial C(x,t)}{\partial x} - - - - - - - - \rightarrow (1.6)$$

Hence, the above equation (1.6) implies that the resultant current is directly proportional to concentration gradient of the electroactive species (Bard & Faulkner, 2015). In this section, we discuss about various electrochemical characterization techniques, including cyclic voltammetry (CV), electrochemical impedance spectroscopy (EIS), amperometry and differential pulse voltammetry (DPV) in detail.

1.9 Need for functionalization of GS and GNR

Despite the great application potential, it is worth mentioning that pristine GS and GNR possesses hydrophobic character, which exhibits poor dispersion in both aqueous and non-aqueous solvents and weakens the interaction with the environment. Furthermore, the van der Waals force of attraction and $\pi - \pi$ stacking tends GS to restack and reduce its large surface area (D. Li, Müller, Gilje, Kaner, & Wallace, 2008; Shan et al., 2009). The above mentioned hurdles limit its application in various fields, especially in electrochemical biosensor (C. Li & Shi, 2012). These issues can be circumvented through surface functionalization, hybridization and structural engineering, which results in change in surface chemistry, dispersion and reactivity of GS (Bo, Zhou, & Guo, 2017). Various functional moieties and defects introduced on both basal and edges of GS and GNR during functionalization, convert sp^2 hybridized carbon atoms to sp^3 hybridization. The existence of these sp^3 carbon atoms in functionalized GS, decreases the

aromatic character, subsequently increases the surface reactivity of the GS. During functionalization, different nanomaterials like metals, metal oxide or semiconducting nanostructures, and conducting polymers, incorporated with GS, act as spacer material, thereby, increases the inter planar space, inhibit the aggregation of GS and enhance the surface area, improving the dispersion both in aqueous and non-aqueous solution. In the case of electrochemical biosensor, the functionalized GS and GNR provide larger electrochemically active surface area which facilitate the adsorption of more biomolecules and expedites the electron transfer between the electrode surface and target, consequently lead to a sensitive and fast current response (Chunfeng Wang, Xu, & Zhuo, 2014).

1.10 Chemical functionalization

Here we briefly discuss about the functionalization of GS and GNR. As a first step we start with chemical functionalization, followed by its pros and cons. Next, we discuss about the plasma functionalization, intercalation of carbon nanomaterials and metal nanoparticles. Finally, we elucidate the structural engineering for GNR.

In general, chemical modification can be achieved through either covalent bonding or non-covalent interactions (Kuila et al., 2012). The former is usually achieved *via* four different ways: (i) nucleophilic substitution, (ii) electrophilic addition, (iii) condensation and (iv) addition reactions. This approach allows various kinds of functional moieties, nanomaterials and polymers to bond with GS covalently, resulting in the formation of functionalized GS sheets. One of the main advantages of the covalent functionalization is the increased efficiency to obtain proper dispersions, although it presents the two main drawbacks of the inevitable loss of their electrical and/or electronic properties and the uncontrolled degree of functionalization (Englert et al., 2011).

In contrast, the non-covalent functionalization is achieved *via* hydrophobic, van der Waals, and electrostatic forces interactions, polymer wrapping, adsorption of surfactants or small aromatic molecules, and interaction with porphyrins or biomolecules such as deoxyribonucleic acid (DNA) and peptides. This approach can alter the surface chemistry or solubility of GS, by introducing hydrophilic ligands onto GS, since pristine GS is hydrophobic, and also preserving the intrinsic properties of GS, and, consequently, their original electronic and optical properties.

In this case, the adsorption of functional groups does not distort the extended π-conjugated system ($sp^2 \rightarrow sp^3$ re-hybridization). However, the main drawback of this method is the possible re-aggregation of the GS due to the inherently weak interactions (Georgakilas et al., 2012, 2016) .

1.10.1 Disadvantages of chemical functionalization methods

Both covalent and non-covalent technique have been employed extensively in the surface functionalization of GS. Though, it offers several advantages, in chemical functionalization, preserving the carbon backbone of GS, is one of the major challenges. Requirement of multistep reactions to achieve the desired functionality, usage of solvents like strong acids, strong base and high temperature condition could lead to cleavage of the carbon framework and introduced functional moieties and defects in an uncontrolled manner. As an alternative, plasma surface functionalization provides a one-step controlled functionalization and avoids the usage of solvents and acids, makes it more environmentally benign. And also, functionalization are performed only to the surface, which generally do not alter the bulk properties of the material (Xiaohui Lu, Wang, Wang, & Guo, 2016).

1.11 Plasma functionalization

It is an economical and effective technique gaining popularity in various fields to change the chemical composition and properties such as wettability, refractive index, hardness, chemical inertness, lubricity, and biocompatibility of material, without affecting the bulk properties of the material (Walton et al., 2017).

The term *plasma 'the fourth state of matter'* was first investigated by Sir William Crookes and Langmuir in 1929. Plasma is composed of highly excited atomic, molecular, ionic, and radical species. It can be generated by heating a gas or by applying strong electromagnetic fields, for instance, radio frequency (RF), microwave, or electrons from a hot filament discharge. The high-density ionized and excited species in the plasma can change the surface chemistry of the material by breaking the covalent bonds on the surface of any inert materials such as CNT, GS, etc. According to the degree of ionization, plasma can be divided into hot plasma and cold plasma (non-thermal plasma) (Karahan & Özdoğan, 2008). In recent years, non-thermal plasma has become a suitable and adaptable tool for the functionalization of various materials. Depending upon the vacuum condition this

type of plasma can be further divided into atmospheric-pressure plasmas and low-pressure plasmas. Low-pressure plasma are more controllable and reproducible in introduction of functional groups than atmospheric-pressure plasmas. The low-pressure plasma, which have found applications in the field of materials processing for the past fifty years, typically consists of a power supply, reaction chamber with electrodes, gas feeding and pumping units including gas flow controllers and pressure gauge.

In low-pressure plasma, plasma can be discharged *via* different types, for instance, microwave discharge (300MHz < f < 300 GHz), RF discharge (ideally 13.56MHz), direct current discharge, dielectric barrier discharge, corona discharge, electric arc, hollow cathode discharge, electron beam, plasma torch and alternating current microwave-excited surface-wave plasma. Several research works have been reported on plasma functionalization of GS surface. During this functionalization, various functional moieties were introduced on the surface of GS, modifying its surface chemistry and the electronic structure. Gokus et al. reported on O_2 RF plasma functionalized GS synthesized *via* micromechanical exfoliation and subsequently demonstrated photoluminescence (Gokus et al., 2009). Lin et al. reported a work on nitrogen doping of mechanically exfoliated monolayer and CVD bilayer graphene through the use of NH_3 plasma treatment (Lin, Lin, & Chiu, 2010) Elias et al. converted graphene to graphane through the use of H_2 DC plasma (Elias et al., 2009). Kumar et al reported a nitrogen functionalized GS by microwave nitrogen plasma treatment and demonstrated its enhanced electrocatalytic activity (A. Kumar et al., 2013). In another work, Wei et al reported nitrogen functionalized GS by chemical vapor deposition (CVD) using methane (CH_4) and ammonia (NH_3) as carbon and nitrogen source, and demonstrated its potential application in dielectrics (Wei et al., 2009). Also, Wang et al reported a novel strategy for the in-situ preparation of nitrogen functionalized GS using microwave plasma assisted chemical vapor deposition (CVD) using polydimethylsiloxane (PDMS) as a solid carbon source, high purity nitrogen gas as nitrogen source and their electronic properties were studied (Chundong Wang et al., 2013). Shao et al. reported a method to prepare nitrogen functionalized GS by exposing it to nitrogen plasma with enhanced electrocatalytic activity towards oxygen reduction and H_2O_2

reduction with high durability and selectivity than widely-used expensive Pt for electrochemical energy devices (fuel cells, metal air batteries) and biosensors applications (Shao et al., 2010). Compared to other types of plasma functionalization, RF has some important advantages such as applicability for insulating substrates without sputtering of electrodes, easy coupling within the chamber, and the ability of creating much more free radicals, plasma reactions or dissociations, and ionization reactions and avoiding high temperatures. Thus it can offer many opportunities for wide range of applications at the interface of plasma physics, radiation chemistry, biomedicine, biomaterial and biosensor. Therefore, in this thesis we focus on surface functionalization of GS *via* RF plasma functionalization technique.

1.12 Other Methods of GS functionalization

The limits of RGO can also be overcome by other promising approaches like incorporation of carbon based nanomaterials and metal nanoparticles into GS. Among the various approach we first discuss about the incorporation of carbon nanomaterial into GS.

1.12.1 Incorporation of carbon based nanomaterials into GS sheets

In this approach GS acts as a 2D planar substrate for anchoring other carbon based nanomaterials like CNT, GOS, GNR and fullerene (Mani, Chen, & Lou, 2013). Here, the carbon nanomaterials incorporated in 2D platform act as a spacer material between the GS also prevent the face to face stacking of GS, enhance the dispersion in any solvent and increase the surface area and pore size. Hence, the hybridized GS exhibits a synergetic properties of GS and spacer material by providing large specific surface area, increased electrical conductivity which enhances the diffusion of ions (Tung et al., 2009). Moreover, the material serves as a novel hybrid electrode for applications in the field of nanoelectronics, energy storage, and sensing (F. Liu, Piao, Choi, & Seo, 2012; Mingkai Liu et al., 2013; W. Wang et al., 2014; M. Q. Zhao et al., 2013). Recently, considerable efforts have been received in inhibiting the aggregation of GS by including the carbon spacers, such as functionalized carbon nanotubes (f-CNTs) or carbon black (CB) or carbon nanofibers (CNF) into GS(Chang et al., 2013).

In 2009, Dai's group reported CNT/GS composite with the ordered structure prepared by layer-by-layer (LBL) electrostatic self-assembly of poly (ethyleneimine)-functionalized GS sheets and acid-treated CNT. The obtained CNT/GS showed high performance as a capacitor (D. Yu & Dai, 2009). Chen and co-workers fabricated CNT/GS, by a simple mechanical mixing method, with high surface area and multi-modal porous structure, which was applied as an electrochemical sensor for the detection of acetaminophen (Xu Chen, Zhu, Xi, & Yang, 2012).

1.12.2 Introduction of nanoparticles

Incorporation of metal nanoparticles is also an approach to enhance the surface area and dispersion of GS, thereby enhances the electrocatalytic performance of hybrid material. Transition metals, noble metals, metal oxide, bimetallic nanomaterials can be introduced onto the hybrid material. This type of functionalization can be performed using different physical or chemical approaches: physical attachment, in situ chemical reduction process, electrochemical synthetic processes, impregnation processes, self-assembled and approach ultrasonic spray pyrolysis (Kuang, Xu, Liu, Hu, & Wu, 2013).

During this incorporation of nanoparticles with GS, the sp^2 hybridization of carbon atoms remains intact. Thus, GS functionalized by these methods can be highly conductive. Luo et al. (2012) studied the electrochemical performance of potentiostatically electrodepositing metallic copper nanoparticles on graphene sheets (Cu/GS). Here the nanocomposite was synthesized using the hydrothermal method. The nanocomposite exhibited an improved electrochemical performance, good cycling stability, highly selective and sensitive, stable and fast amperometric sensing of glucose (Luo, Jiang, Zhang, Jiang, & Liu, 2012). Dar et al. (2014) prepared the nanocomposite of silver nanoparticles anchored on GOS for sensing arsenic (III) (Dar, Khare, Cole, Karna, & Srivastava, 2014). In the case of GOS-based nanocomposites, the unique properties of GOS make them particularly useful as the nanoparticle support. This is because the high surface area is essential for the dispersion of the nanoparticles in order to maintain their chemical activities. The GOS supporting materials not only maximize the availability of the nanosized

surface area for electron transfer, but also provide better mass transport of the reactants to the chemically active sites.

Numerous research works have been reported on GOS-based nanocomposites with noble metal nanoparticles(Pt ,Au ,Ru) and metal oxide nanoparticles (TiO_2, ZnO , SnO_2, Cu_2O, MnO_2,NiO, and SiO_2) and used in a variety of applications ranging from catalytic systems to fuel cells, sensors, supercapacitor, and storage batteries (Scenev, 2014). In spite of various catalytic material, nickel (Ni) nanoparticle with GS obtained by various methods with outstanding catalytic property can readily be used to fabricate an electrochemical sensors (G. Wang et al., 2013) &(Si, Huang, Wang, & Ma, 2013).

1.12.3 Structural engineering for GNR: Porous GNR

Noting the GS layers tend to preferentially form aggregated structure to minimize the presence of edge plane sites, various structural engineering strategies, such as vertical structure, tube-like structure, and porous structure have been applied to proliferate the exposed edge sites of GNR for enhanced electrocatalytic activity. The structural engineered GNR and its composites have been widely used in the various fields because of large surface area and porous structure. The increased distance between layers of structural engineered GS alleviates the aggregation of GS and is favourable for the exposure of active sites for electrocatalysis.

Researchers recognized that GS and GNR with large specific surface area plays a vital role in affording more available sites for charge accumulation and promotes the electrochemical performance of electro- catalyst in electrochemical biosensor system. Recently porous materials have been extensively designed, prepared and investigated from both fundamental and technological viewpoints. Among these synthesis methods, template-directed CVD is an important and easy method to prepare foam-like porous GS. The nickel foam is the most commonly used template for the synthesis of GS foam. Chen et al. first reported foam-like GS using an interconnected nickel scaffold as template (Zongping Chen et al., 2011). Based on this pioneering work, the CVD method is widely used for preparation of GS foam and obtained porous GS is applied in various fields. These demonstrations, reveal structural engineered GS and GNR can improve the performance and motivate the applications of these porous material in electrochemical sensors.

1.13 Scope and objectives of the thesis

The focus of our research work is to improve the electrochemical performance of RGO. In order to realize the better electrochemical activity of RGO, the main modification that needs to be done is to alter the morphology and surface chemistry of GS and GNR by controlled functionalization technique, facilitate the introduction of defects, which in turn enhance its electrochemical properties. Inspired by the enhanced reactivity and mobility of electrons, we have focused on the synthesis of RGOS, as it possesses defects and oxygen containing functional moieties on the basal and edges. Recent literature shows that considerable effort has been made to functionalize GS and GNR based derivatives for electrochemical applications. The nature of defects plays a notable role in altering the interfacial interaction and charge transfer mechanism in the systems. A systematic understanding on functionalization of GNR and GS based hybrids will be beneficial for the fabrication of high performance devices.

Based on this outlook, the main objectives of the present work are

1. Surface modification of GS by controlled functionalization technique
2. Physico-chemical characterization of surface modified GS
3. Electrochemical characterization of surface modified GS
4. Studying the performance of electrochemical biosensor on surface modified GS for various analytes
5. To achieve limit of detection down to nanomolar range with high selectivity, high specificity, enhanced reproducibility and stability of sensor
6. Enhanced performance of the sensor in real time application

1.14 Organization of the thesis

Chapter 1 gives an overview on synthesis and properties of GS and GNR. The present chapter also describes the various approaches of functionalization and application in electrochemical biosensor.

Experimental procedures for the synthesis of GOS, various characterization techniques, electrode fabrication and different electrochemical techniques carried out throughout the thesis are described in chapter 2.

Chapter 3 puts forward the plasma functionalization of RGO and its application in nitrite sensing.

Chapter 4 describes application of hybridized GS and plasma functionalized hybridized GS for sensing various biomolecules like ascorbic acid, simultaneous determination of ascorbic acid, uric acid dopamine and glucose, respectively.

Chapter 5 elucidates the synthesis of porous graphene nanoribbons, which is further electrochemically deposited by gold nanoparticles and applied as immunosensor for detection of alpha fetoprotein

The major results and outcome of this research work are summarised in Chapter 6. Finally, the future possible applications are suggested.

CHAPTER 2

MATERIALS AND METHODS

This chapter describes the materials used throughout the research work and experimental procedure employed for the synthesis of reduced graphene oxide (RGO). It also discusses the various material characterization techniques, fabrication of electrode and electrochemical characterization techniques carried out throughout the thesis work.

2.1 Materials

Graphite flakes with particle size <20 μm, multi-walled carbon nanotube (MWCNT), of carbon > 95% 6 - 9 nm O.D x 5 μm L, human hemoglobin (Hb, MW 64,500 daltons), chloroauric acid ($HAuCl_4$), uric acid (UA) and dopamine (DA) were purchased from sigma Aldrich. Conc. sulphuric acid (H_2SO_4) 98%, ortho phosphoric acid (H_3PO_4) 88%, potassium permanganate ($KMnO_4$), hydrogen peroxide (H_2O_2) 30%, hydrochloric acid (HCl) 35%, hydrazine hydrate $(NH_2)_2$ .H_2O 98%, hydroiodic acid (HI) 55%, acetic acid glacial indifferent to chromic acid 100%, hexaammineruthenium (III) chloride($[Ru(NH_3)_6]Cl_3$), sodium nitrite ($NaNO_2$), phosphate buffer saline (PBS), ferrocyanide($K_4Fe(CN)_6$), ferricyanide ($K_3Fe(CN)_6$), nickel chloride ($NiCl_2.6H_2O$), sodium hydroxide (NaOH), ethanol, poly vinyl pyrrolidine (PVP), ascorbic acid (AA), dextrose, sucrose, sodium chloride (NaCl) and bovine serum albumin (BSA, 96–99%) were purchased from Merck India. 99.99% pure nitrogen, oxygen and ammonia gases used in the plasma functionalization process were purchased from Tapaswi enterprises, Kolkata, India. Sodium hydrogen carbonate ($NaHCO_3$) is purchased from Nice chemicals. Alpha fetoprotein (AFP) and anti-AFP were purchased from MyBioSource, Inc.USA.

2.2 Methods

2.2.1 Synthesis of GOS

GOS was prepared from natural graphite flakes through one-pot synthesis based on improved method (Marcano et al., 2010). In this method, 3.0 g of graphite flakes and 360 mL of H_2SO_4 were mixed and stirred in room temperature for several minutes. Then 18.0 g of $KMnO_4$ was added slowly into the solution under stirring condition. Subsequently, after 30 min of stirring, 40 mL of H_3PO_4 was added to the reaction to yield GONS with more ordered graphitic basal planes. The oxidation

process was performed at 60°C for 12 h with continuous stirring to yield a brown suspension. To eliminate excess of $KMnO_4$, 5 mL of 30% of hydrogen peroxide (H_2O_2) was added slowly and stirred for 10 minutes. After reaching room temperature the mixture was centrifuged and washed with 1:10 HCl aqueous solution (250 mL) to remove metal ions. Finally, it was purified by dialysis for one week using a dialysis membrane. Then the obtained GOS solution was centrifuged and vacuum dried at 60°C for 24 h to produce the powder of GOS.

2.2.2 Synthesis of graphene oxide nanoribbons (GOR)

GOR was synthesized by unzipping CNT via novel strategy adopted by improved method (Higginbotham et al., 2010). In detail, 150 mg of multiwall carbon nanotube (MWCNT) was stirred with 36 mL of H_2SO_4 for 1 h at room temperature. After 1 h, 4 mL of H_3PO_4 was added to the mixture followed by addition of $KMnO_4$ gradually. The oxidation process was carried out at 65ºC temperature with constant stirring for 4 h. The reaction was terminated by adding 3 mL of 30 % H_2O_2 in 50 mL distilled water. Finally the brown coloured dispersion was washed by HCl, ethanol and distilled water successively. The obtained GONR solution was dried for 12 h at 60ºC under vacuum to get GOR powder.

2.2.3 Synthesis of RGO

RGO was synthesized with better graphitization by reducing GOS using a mixture of HI acid and acetic acid. In detail, the obtained GOS of 150 mg was transferred to a 500-mL round-bottom flask and dispersed in 150 mL of acetic acid. The dispersion was sonicated using ultrasonic bath sonicator until no visible particulate matter was observed. 20 mL of HI was added to the mixture and was constantly stirred at 50°C for 48 h. This product was isolated by filtration using polycarbonate filter and washed copiously with saturated sodium bicarbonate solution and deionized water several times. Finally the product was vacuum dried overnight at room temperature to yield RGO.

2.3 Characterization

A combination of spectroscopic and microscopic techniques was employed to analyse the materials synthesized for this research work. The chemical features, elemental composition and extent of modification in GS samples were investigated by Fourier transform infrared spectroscopy (FTIR), Raman spectroscopy and X-ray

photoelectron spectroscopy (XPS). Characteristic absorption of the sample was studied using ultraviolet-visible (UV-Vis) absorption spectroscopy. Optical emission spectroscopy (OES) was used to observe the various ionized species produced during plasma interaction. Crystallinity of the samples was analysed using X-ray diffraction studies (XRD). The charge distribution of the sample was examined by zeta potential analyzer, Brunauer-Emmett-Teller (BET) was applied to calculate the specific surface area of the sample. The morphology and surface features of the samples were studied by various microscopic techniques like scanning electron microscopy/energy-dispersive X-ray spectroscopy (SEM/EDX), transmission electron microscopy (TEM) and atomic force microscopy (AFM).

2.3.1 Spectroscopic techniques

2.3.1.1 FTIR

It is a technique based on the molecular vibration spectrum, used for identifying the type of chemical bonds in a molecule by transmitted or absorbed infrared spectrum of different samples like organic, polymer solids, liquid and gas. The frequency of infrared region in the electromagnetic spectrum ranging between 12800 to 10 cm^{-1}, can be classified in to three categories: near infrared (NIR) (12800 to 4000 cm^{-1}), mid infrared (MIR) (4000 to 200 cm^{-1}), and far infrared (FIR) (50 to 1000 cm^{-1}). Since, the "MIR" in the frequency range corresponds to the fundamental vibrations of nearly all the functional groups of organic molecules, it is the most desirable for chemical analysis of any known or unknown molecule.

When the samples are subjected to infrared radiation, some part of the radiation is absorbed by the molecules in the sample, which vibrate at certain frequency. Rest of the radiation is transmitted according to Beer's Law and is collected by a detector. The obtained signal is processed using complex mathematical operations known as Fourier Transformations, and a unique spectrum is produced between transmittance and frequency (Fuller & Griffiths, 1978).

The instrument used for the present study is Perkin Elmer Model spectrum 100 ,FTIR, USA in the wavenumber range of 4500-400 cm^{-1} and 0.5 cm^{-1} optical resolution of the instrument. The samples were diluted with KBr before the measurement and each sample was scanned 32 times.

2.3.1.2 XPS

This is one of the most widely used surface-sensitive quantitative spectroscopic technique, which could interact with the electrons in core level. It provides the information regarding composition, type of bonding, chemical and electronic state of the element and empirical formula. This measurement analyses the average depth of approximately 5 nm. A highly focused monochromatic soft X-rays (commonly Al Kα or Mg Kα) is used to irradiate the sample surface under ultra- high vacuum conditions. The initial step of the exposed X-ray photon is the ejection of an electron from the core electronic levels. The ejected electrons possess certain kinetic energy (KE) of the photo emitted core electron, which relates the binding energy of electron in the atom. The change in the measured KE alters the binding energy (BE) of a photoelectron. The BE of the electron identifies it specifically, both in terms of its parent element and atomic energy level. The information regarding chemical state and quantitative data are related to the position and intensity of the peaks in an energy spectrum, respectively (Engelhard, Droubay, & Du, 2017). The relationship between the KE and BE involved in the experiment is given by the simple equation (2.1).

$$\mathrm{BE} = \mathrm{h}\nu - \mathrm{KE} - \mathrm{W} \longrightarrow (2.1)$$

where 'h' is Plank`s constant, 'ν' represents threshold frequency, 'KE' denotes the kinetic energy of the electron and 'W' is the work function of the spectrometer. Kratos Axis ultra-photoelectron spectrometer with a monochromatic Al Kα X-ray source (1486.6 eV) operated at 225W (15 kV, 15 mA) was used to investigate the elemental composition of RGO and modified RGO. XPSPEAK 4.1 software was used for a detailed analysis of C1s, O1s and N1s core level spectra allowed to reveal the content and nature of carbon bonds attached to different oxygen and nitrogen moieties and to calculate the atomic concentrations. For instance, in the case of RGO and functionalized RGO, the C1s spectrum of the sample clearly indicates the degree of functionalization with four different components, which correspond to carbon atoms of different functional groups: C=C, carbonyl (C=O) bonds and the carboxylate carbon (O–C=O).

2.3.1.3 Raman spectroscopy

It is a non-destructive technique based on inelastic scattering of a monochromatic light (e.g., laser light), employed for studying vibrational, rotational, and other low-

energy modes in a material. When the laser beam is directed towards the sample, photons are absorbed and scattered by the material. A change in the frequency (wavelength) of the incident and scattered photon (inelastic scattering) is called Raman scattering (Raman & Krishnan, 1928). Raman spectroscopy plays an important role in the structural elucidation of graphitic materials.

The Raman spectrum of the samples under study is recorded in WiTec alpha 300 micro-Raman system Germany, with a grating of 600 g/mm. Lasers wavelength of 488 nm, was employed with comparable beam spots 2 mm in diameter.

2.3.1.4 UV-Vis absorption spectroscopy

UV-Vis absorption spectrum is a powerful spectroscopic technique for the characterisation of nanomaterials. In this spectroscopy, the molecules in the sample exposed to UV or visible light, will undergo electronic excitation by the absorption of light from ground state to excited state (Goodmans, 1963). The fundamental features of absorption band in this spectroscopy are the position and intensity. The position of absorption band relates the wavelength of radiation whose energy is equal to that required for the electronic transition from ground state to the excited state. Then, the intensity of absorption can be derived from Beer Lamberts law:

$$A = \in cl \longrightarrow (2.2)$$

where ' A' is the measured absorbance, '$\in$' is the absorptivity, 'l' is the path length and 'c' is the concentration of the solution.

Deuterium discharge and tungsten-halogen lamps are commonly used light sources for UV- visible measurements and NIR measurements. In UV-visible-NIR spectrometers photomulplier tube combined with Peltier-cooled PbS IR is used as detector. Optical absorption measurements of the samples are recorded by dispersing in ethanol using Cary 100 Bio UV-visible spectrophotometer Agilent Technologies USA.

2.3.1.5 OES

It is an analytical technique used to analyze the various active species present in plasma, discharged from various sources like spark discharge, or direct-current arc discharge, or glow discharge (DeKalb, Kniseley, & Fassel, 1966). In this emission spectroscopy, energy acquired by various active species like excited and ionized atoms in the discharged plasma can be re-emitted as radiation and creates a unique

emission spectrum, which is collected and analyzed by a spectrometer. The emission of specific frequencies can be used to identify the species present in the plasma and the intensity of each emission spectrum relates the concentration of the active species in the plasma. Therefore, numerous plasma parameters can be analyzed by means of OES.

The OES was recorded using ocean optics spectrophotometer (HR 2000, USA) in the visible and UV ranges. The spectrophotometer consists of an optical fiber array, which is composed of linearly-aligned cores, and placed to detect the axial distribution of the optical emission. The other end of the optical fiber array is placed close to the entrance slit of a monochromator with a focal length of 500 mm. The exit side of the monochromator is connected to an ICCD camera, by which the optical emission spectra in the spectral range of 200–1000 nm at various distances can be recorded.

2.2.1.6 XRD

XRD is a non-destructive, analytical technique which provides information about the crystal structure, structural properties (strain state, grain size, epitaxy, phase composition, preferred orientation, and defect structure) of the phases and determine the thickness of thin films. When a monochromatic beam of X-ray with wavelength 'λ' incidents at an angle 'θ' upon a crystalline solid which consists of a regular array of atoms, stacked into lattice planes separated from one another by a distance 'd', will scatter x-rays and undergo constructive and destructive interferences.

According to Bragg's law (Bragg, 1929) we have:

$$n\lambda = 2d\sin\theta \longrightarrow (2.3)$$

where 'n' is a positive integer.

XRD pattern also allows estimating thickness of sheets by Scherrer equation (Debye & Scherrer, 1916) as given in equation 2.4. This equation gives the relationship between diffraction peak full width half maximum (β) and thickness (t).

$$t = \frac{0.89\,\lambda}{\beta\cos\theta} \longrightarrow (2.4)$$

The number of layers is calculated from the formula given below

$$N = \frac{t}{d_{(spacing)}} - - - - - - - \rightarrow (2.5)$$

where, t is the thickness of GNS, $d_{(spacing)}$ is the interlayer spacing of particular plane. Bruker AXS D8 advance X-ray diffractometer Germany, with Cu Kα (λ=1.54 Å) radiation was used for XRD studies of the synthesized powder samples. XRD pattern was recorded in the range 2θ =5 to 80°.

2.3.2 Microscopic Techniques

2.3.2.1 SEM

It is employed to obtain images at maximum resolution, which can be used to get a better understanding of surface morphology. In this system, the features of the sample are obtained by scanning the surface with a beam of electrons at high energy in raster pattern. When the electrons in the beam interact with atoms in the surface of the sample, it produces various forms of electrons in the form of signals, including secondary electrons, back-scattered electrons, characteristic X-rays and light cathodoluminescence, absorbed current (specimen current) and transmitted electrons, which contain information about the topography and composition of sample's surface. Among the various signals, secondary electrons and backscattered electrons are generally used for imaging samples: secondary electrons are most important for revealing the morphology and topography of samples and backscattered electrons are beneficial for illustrating the contrasts in composition of multiphase samples (Burany, 2003).

For SEM imaging, the specimen must be electrically conductive, to avoid the accumulation of electrostatic charge on the sample surface. So, before every analysis, the specimens are usually coated with gold conducting materials using gold sputter coater. The SEM is usually equipped with an EDX system, which enables to get information on the chemical composition of the sample.

EDX is an analytical technique, which depends on the investigation of X-ray emitted from the sample. Here a high energy electron beam, is focused on the sample, the incident electron beam may stimulate an electron in an inner shell, ejecting it from the level while creating an electron hole. The electron hole i.e empty space is occupied by a higher energy electron from an outer shell and the difference in energy between the higher energy level and the lower energy level may be

released in the form of an X-ray. The energy emitted from a sample can be measured by an energy dispersive spectrometer. As the energy of the X-ray is characteristic of the difference in energy between the two levels, and of the atomic structure of the element from which they were emitted, this allows the elemental composition of the specimen to be measured.

In this study, the elemental analysis of specific materials on each step of modification was initially confirmed by the SEM-EDX analysis. The SEM-EDX analysis was performed on a Hitachi S 2600N SEM (Hitachi Scientific Instruments, Tokyo, Japan) equipped with a micro analysis detector for EDX (Inca x-act, Oxford Analytical Instruments, Abington, UK). EDX spectra were collected at 30°angle, 20 kV accelerating voltage and 20 mm working distance. EDX results were analyzed using incorporated Inca, Point and Analyze software.

2.3.2.2 TEM

It is an electron microscopic technique used for analysing the defects, crystallographic structure, morphology, particle size and even composition of a specimen. When a beam of high voltage (up to 300 kV) electron transmits through an ultra-thin specimen (nearly 200 nm), it gets scattered. The scattering of the electrons during the transmission determines the kind of information about the sample. Through elastic scattering, diffraction patterns can be observed. The diffraction mode displays accurate information about the local crystal structure. The inelastic scattering will produce spatial variations in the intensity of the transmitted electrons, which can be distinguished by the detector during image formation. This imaging mode provides a highly magnified view of the micro- and nanostructures and ultimately, in the high resolution imaging mode a direct map of atomic arrangements can be obtained (high resolution TEM) (Hayat, 1986).

For imaging using TEM, sample dispersed in ethanol is drop casted on the inner meshed area of TEM grid made up of Cu, with a diameter of 3 mm and thickness and mesh size ranging from 10 to 100 μm. The sample is dried under vacuum before imaging. TEM imaging was done using high resolution transmission electron microscope (HR-TEM) (FEI Tecnai. G230, Hillsboro, USA).

2.3.2.3 AFM

AFM a kind of scanning probe microscopy (SPM) developed by Binnig et al. in 1986. It has been developed to be the foremost tool for evaluating the parameters like height, friction, surface topography and manipulating matter at the nanoscale. The basic SPM working unit consists of a cantilever with a sharp tip, laser, photodiode, detector and feedback electronics and piezoelectric scanner. It works by measuring force between a probe and the sample. In general, the imaging mode of AFM can be operated by two modes i.e contact and non-contact. In contact mode, the cantilever tip is "dragged" throughout the surface of the sample and the topography of the surface is determined either by the cantilever deflection directly or by using the feedback signal required to keep the cantilever at a static position. In non-contact mode, the cantilever tip does not contact the surface of the sample. The cantilever tip externally oscillated at or close to its fundamental resonance frequency and this oscillation amplitude, phase and resonance frequency are modified by the tip-sample interaction force; these changes in oscillation with respect to the external reference oscillation provide information about the sample surface characteristics (Binnig & Quate, 1986).This mode is one of the foremost method used in definite identification of the number of layers in GNS. In the literature, it has been reported that the thickness of single-layer GNS is in the range from 0.34-1.2nm.

In our study, samples are dispersed in ethanol and drop casted on freshly cleaved mica sheet. Before imaging the substrate was allowed to dry under vacuum for 24 h. Agilent Technologies 5500 Scanning Probe Microscope USA, was used for the studies.

2.3.3 Zeta-potential measurements

Zeta-potential is a fundamental parameter used in the area of colloid chemistry. This measurement is used to observe the behaviour of the dispersive system in liquids. All the liquids in colloidal suspension have a surface charge. The particle in the suspension is subjected to an electric field. Due to the interaction between the charged particle and applied field, the particles will tend to move and scatter light in all directions. The direction and velocity of the motion is a function of particle charge, suspending medium and electric field strength. The Doppler shift observed

in the scattered light represents the particle velocity. The particle velocity is proportional to the electrical potential of the particle at the shear plane which is zeta potential (Hunter, 1981).

These measurements were performed at 25º C using a Zeta sizer nano ZS (Malvern Instruments S.A., Worcestershire, U.K) in 173 scattering geometry. All measurements were made using disposable cells at a concentration of 0.0001 g in 10 mL.

2.3.4 Specific surface area measurements

Specific surface area (m^2/g) of the samples are determined by BET (Brunauer, Emmett, & Teller, 1938). The BET theory describes the physical adsorption of gas molecules on a solid surface. Conventionally, nitrogen is used as adsorbate gas. Before the specific surface area measurement, it is necessary to remove gases and vapours from the sample. This was performed by heating the sample at 100º C temperature. Next the samples were dried with nitrogen purging. The amount of adsorbed gas is correlated to the total surface area of the particles including pores in the surface.

The specific surface area of the sample determined by N_2 adsorption-desorption isotherm analysis was carried out using ASAP Model 2020 Chemisorption – Physisorption/Chemisorption Analyzer, India.

2.4 Electrochemical characterization techniques

All electrochemical measurements were performed at room temperature (Room Temperature, 25 ± 2 °C) with a potentiostat/ galvanostat PG 302N, AUT 83909 (Metrohm, Autolab, Netherlands) with a three-electrode system: working electrode, silver/silver chloride (Ag/AgCl in 3.0 M KCl) reference electrode and platinum (Pt) wire counter electrode. Throughout the thesis, the modified glassy carbon electrode (GCE) was used as WE. All chemicals and reagents for electrochemical measurements were of analytical grade and used as such without further purification. All the electrolyte solutions are prepared with water from Millipore Autopure system (18.2 MΩ, Millipore Ltd., USA).

The electrolyte used in various electrochemical measurements will be specified in corresponding sections. Before each electrochemical measurements, the electrolyte was purged with pure nitrogen gas for few minutes, to remove the dissolved oxygen.

2.4.1 Fabrication of electrode

The working electrode for electrochemical sensing was fabricated as follows: GCE was polished with 0.3 mm and 0.05 mm gamma alumina particles, followed by rinsing and sonicating in distilled water and ethanol. This was dried under stream of nitrogen. Samples were dispersed in ethanol (1 mg/ 2 mL) by ultrasonication for more than 30 min. GCE was modified by coating with 7 μL suspension of sample, by drop casting method on the electrode surface and dried at room temperature under vacuum for 12 h.

2.4.2 CV

It is the basic experimental approach used for obtaining qualitative data about the reactions take part in the electrochemical cell. It is generally a type of voltammetric measurement, which refers to the measurement of response in the form of current that results from the applied potential. The potential in CV is swept from E_1 to E_2 in a triangular waveform at a particular scan rate to the working electrode, and return back to initial stage E_1. As illustrated in Figure 2.1 complete cycle of potential in triangular waveform consists of both forward scan and a reverse scan. The slope of the potential gradient is called scan rate (ν) represented as V s^{-1}.

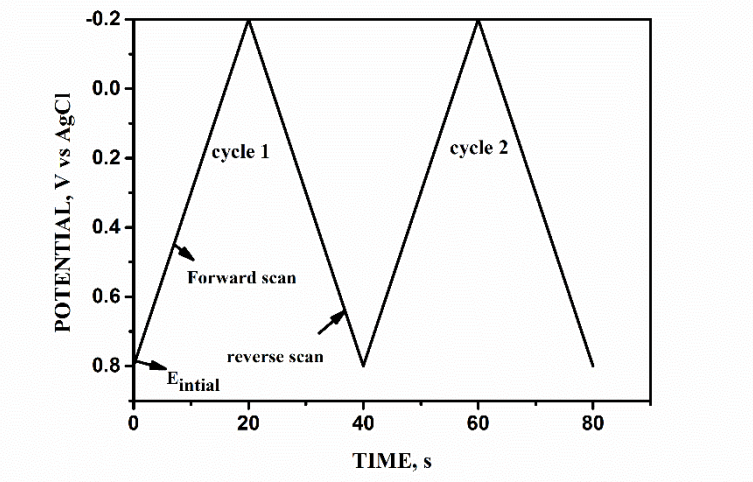

Figure 2.1 Typical triangular excitation signal for cyclic voltammetry

CV offers the rapid identification of redox potential with respect to the electroactive species of interest. This CV technique can also be used for a range of applications, including the determination of number of electrons transferred in the redox reaction, formal potential, rate constants and diffusion coefficients (Heinze, 1984).

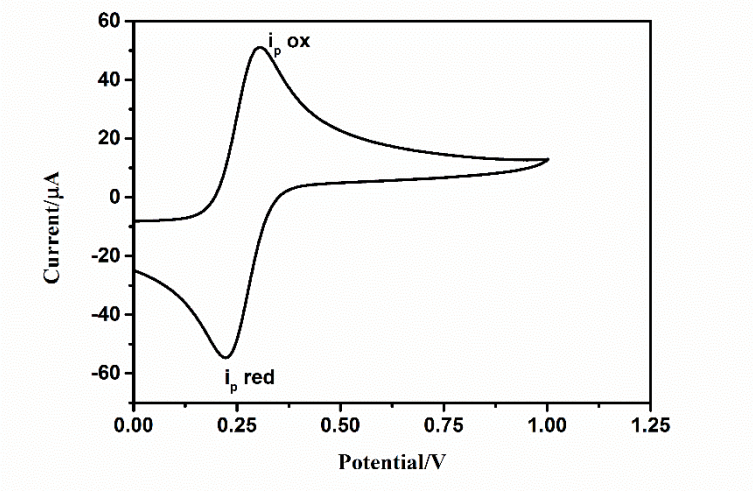

Figure 2.2 Demonstration of typical CV measurement utilizing $K_3Fe(CN)_6$

Figure 2.2 elucidates the plot between I vs V corresponding to the standard redox probe $Fe(CN)_6^{3-}$. The CV represents the resultant current measured with respect to the applied voltage. At the initial potential, the WE and the electroactive species get charged or activated. At this point no redox reactions takes place. When the potential is moved forward over the threshold potential i.e. towards the oxidation potential, at this stage the electroactive species in the interface get oxidized, the concentration of oxidized species is represented as current, which increases until the maximum current I_p is reached. Further increase in the potential, the concentration of the reduced species on the surface of an electrode gets depleted which results in the change of concentration gradient and thus results in increase of a cathodic current. CV can also be used to determine the electroactive area of the WE and the ease of electron transport to the electroactive moieties, allowing the effectiveness of different WE to be compared. In addition, CV provides information on the electrochemical reversibility of the reaction of interest, where irreversibility is easily determined through the disappearance of the reverse scan peak. Particularly, for a reversible electrochemical reaction the peak current I_p is described by Randles – Sevcik equation (2.6)

$$i_p = (2.69 * 10^5) n^{\frac{3}{2}} A C D^{\frac{1}{2}} v^{\frac{1}{2}} \quad ----\rightarrow (2.6)$$

where 'n' represents number of electrons transferred in the reaction, the surface area of the electrode is denoted as 'A' (cm^2), 'C' is the concentration of the redox probe (mM), 'D' is the diffusion coefficient ($cm^2\ s^{-1}$) and 'ν' is the scan rate ($V\ s^{-1}$). The above mentioned equation 2.6 can also be used to calculate the diffusion coefficient

of the electrolyte as the current increases with the square root of the scan rate (for a Nernstian system). Furthermore, from the CV plot one can provide information about the type of the reaction involved in the system (reversible, quasi-reversible or irreversible). For a perfect thermodynamically reversible (or electrochemically reversible) system the ratio between the peak current, $I_{a\ ox}$ / $I_{c\ red}$, will be unity and the peak potential separation between the redox is expressed as:

$$E_{p,ox} - E_{p,red} = \frac{59\ mV}{n} - - - - - - - - - - - - \rightarrow (2.7)$$

where '$E_{p,ox}$' and ' $E_{p,red}$' are the oxidation and reduction potentials, respectively, and n is the number of electrons transferred.

But in practice, all the electrochemical systems do not show the Nerstian behaviour. Such systems are represented as quasi – reversible system, where the rate of electron transfer get decreased than the voltage scan rate. Consecutively, this system causes a separation of the oxidation and the reduction peaks noticed on the CV plot, which can be estimated from the equation (2.8):

$$E_{p,ox} - E_{p,red} = \frac{48\ mV}{\alpha n_a} - - - - - - - - - - - - \rightarrow (2.8)$$

where the electron transfer coefficient is denoted as 'α' and 'n_a'represents number of electrons transferred between the electrode and electrolyte. Moreover, the irreversible system exhibits CV with a shift of 'E_p'with respect to the scan rate, or absence of the reverse peak.

2.4.3 EIS

EIS is a constructive experimental technique, based on the measurement of impedance, which is referred to the frequency dependant resistance to current flow offered by inductor, capacitor etc. Owing to its simplistic, compatibility, automated and can work in any critical environments EIS technique is beneficial over other electrochemical characterization techniques. This technique was used for the determination of the double layer and to provide information about the reactions taking place in the electrode interface (Lvovich, 2012). It is also the response, measured in the form of alternating current from the electrochemical cell resulted by the application of small sinusoidal potential as a function of frequency (Figure 2.3).

The impedance of the electrochemical system can be calculated using Ohm's law as $$Z(\omega) = \frac{E(\omega)}{I(\omega)} \longrightarrow (2.9)$$

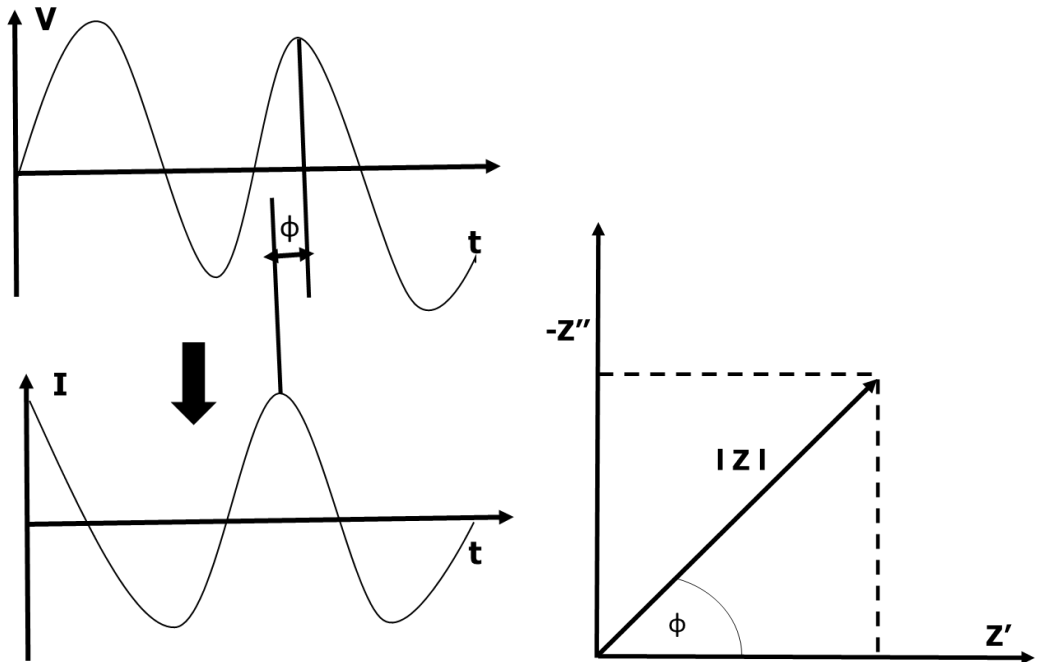

Figure 2.3 Impedance experiment: sinusoidal voltage input (V) at a single frequency (f) and current response (I). It can be expressed as the modulus |Z| and the phase angle φ, or it can be represented by the real (Z') and the imaginary (Z'') part.

The above mentioned impedance, 'Z(ω)' is a complex quantity, which can be represented in two form, one in Cartesian and other in polar coordinates.

In polar coordinates the impedance of the data is represented by:

$$Z(\omega) = |Z(\omega)|e^{\varphi\omega} \longrightarrow (2.10)$$

Here '| Z(ω)|' represents the magnitude of the impedance and ' φ' represents the phase shift. In form of Cartesian coordinates Z(ω)is expressed by:

$$Z(\omega) = Z'(\omega) - j \,.\, Z''(\omega) \longrightarrow (2.11)$$

Where ' Z'(ω)' represents the real part of the impedance and ' Z''(ω)' the imaginary part and $j = \sqrt{-1}$. Subsequently, the electrochemical impedance data was evaluated by the Nyquist and Bode plots.

2.4.3.1 Nyquist plot

The impedance Z(ω) with both real and imaginary value is usually expressed in the Nyquist plot also known as Cole-Cole plot, where the x-axis is the real component (Z') ohmic resistance and y-axis is the imaginary part (-Z'') capacitive resistance.

The shape of the plot plays a significant role in making qualitative data interpretations. The Nyquist plot includes a semicircle portion and a line. The semicircle portion at higher frequency expresses the electron-transfer limited process, and the corresponding diameter is equal to the charge-transfer resistance (R_{ct}). Whereas, the line at lower frequency represents the diffusion process. For example, if the plot demonstrates a perfect semicircle, the impedance corresponds to a single activation-energy-controlled (or charge-transfer) process (Figure 2.4). The Nyquist plot is particularly intended for estimating the electrochemical parameters such as solution resistance (R_s), R_{ct}, electrode polarization resistance (R_p) and double layer capacitance (C_{dl}), etc. However, one of the major disadvantage of Nyquist plot is that information on frequency is not stated on the plot, which makes the estimation of C_{dl} difficult. This can be overcome by labelling the frequencies on the curve (Láng, 1994).

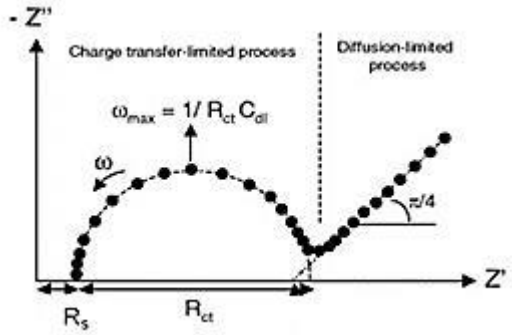

Figure 2.4 Nyquist plot, R_s is solution resistance and R_{ct} is charge-transfer resistance.

2.4.3.2 Equivalent circuit model

Impedance data represented in the form of Nyquist plot is normally analyzed by fitting it to an equivalent circuit model consisting of components like resistors (R), capacitors (C), inductors (L) constant phase element (CPE) and Warburg element (Z_W), which represents the diffusion controlled mass transport of the electrochemical system. This concept of equivalent circuit model was first introduced in 1899 by Warburg.

An example of a generalized equivalent circuit element is illustrated in Figure 2.5

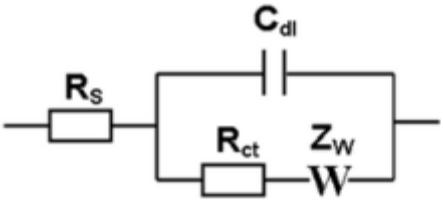

Figure 2.5 An example for equivalent circuit for an impedance cell

The evolution of this equivalent circuit theory continues till Randles, who came up with well-established Randles model in 1947 (Randles, 1947). The common sense in developing an equivalent circuit model is that it should always be selected on the basis of understanding the electrochemical system and does not contain randomly chosen circuit elements. The elements of model can be combined in series and parallel to give complex equivalent circuits.

2.4.4 Chronoamperometry

In this technique, the potential is initially held at a value for which no redox reaction occurs (E_1) then the potential is stepped to a value (E_2) at which the oxidation/reduction of the analyte of interest may occur. The resultant current versus time is measured, for short time periods, and can be modelled using the Cotrell equation,

$$i(t) = \frac{nFACD^{1/2}}{\pi^{1/2}t^{1/2}} - - - - - - \rightarrow (2.12)$$

where n is the number of electrons, F is Faraday's constant, A is the electrochemical surface area, C is concentration of analyte, D is the diffusion constant and t is time. This technique can be used to measure the electroactive area of electrode and the diffusion coefficient of electroactive species. Another common use of this technique is the real-time monitoring of systems, where the potential is held at the redox potential of an electroactive moiety until steady state value is reached. Subsequent addition of the analyte will produce further response with a staircase like signal. And it can be used to electroplate surfaces, which is commonly done by immersing surface in a metal salt plating solution, holding the surface above the reduction potential reducing the metal onto the surface.

2.4.5 DPV

DPV is one of the recent techniques proposed by two eminent persons Barker and Gardner, in recent years it is used by researchers and material scientists for analytical and kinetic studies of the reaction in an electrochemical cell. This

technique is a type of voltammetric method carried out at a stationary electrode, which can be considered as a derivative of linear sweep voltammetry. And it is one of the most sensitive voltammetric methods, since the capacitive currents are strongly eliminated via subtraction. As mentioned earlier, the measured current is the difference in the resultant current measured just before each pulse (I_a) and just before the end (I_b) of each pulse (García-Armada, Losada, & de Vicente-Pérez, 1996). The difference in the resultant current (I_b-I_a) is plotted with respect to the linear sweep voltage as illustrated in Figure 2.6.

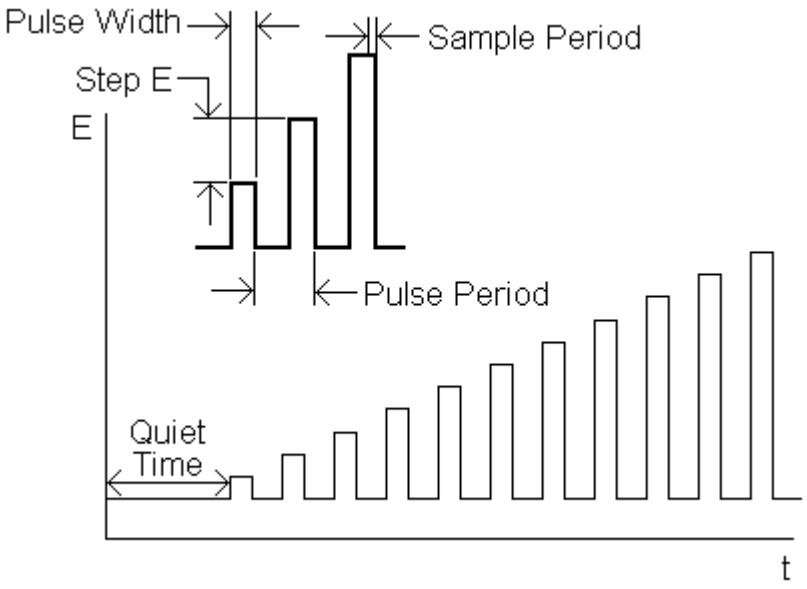

Figure 2.6 Example of applied and measured DPV signals

The obtained peak current will be directly proportional to the concentration of the electroactive moieties of interest.

$$i_p = \frac{nFAD^{1/2}C}{\sqrt{\pi}t_m}\frac{(1-\sigma)}{(1+\sigma)} \quad (2.13)$$

where $\sigma = \exp[(nf/RT)(\Delta E/2)]$ (where ΔE is the pulse amplitude).

This technique has the benefit in the elimination of capacitive charging current, which results in higher sensitivity and better peak resolutions than CV. There is an extra advantage in the case of solid electrodes in discrimination against blocking of the electrode reaction by adsorption. The obtained peak current, with no charging current, makes the technique especially useful for analysis of multiple analytes.

CHAPTER 3

Surface modification of reduced graphene oxide nanosheets through plasma functionalization and its application for electrochemical biosensor

This chapter discusses the surface functionalization of reduced graphene oxide nanosheets (RGO) via radio frequency oxygen, nitrogen and ammonia plasma. The surface chemistry, crystallinity, morphology and the electrochemical property of RGO and plasma functionalized RGO are investigated by various characterization techniques. Finally, this chapter elucidates the application of ammonia plasma functionalized RGO with enhanced electrocatalytic property for nitrite sensor.

3.1 Introduction

GS, a two-dimensional material, has received tremendous interest, with its outstanding properties including stiffness, strength, elasticity, high thermal conductivity, excellent electron mobility, and tunable band gap (Geim & Novoselov, 2007). These properties enable GS to be a potential candidate in a wide range of applications in nanoelectronics, biosensors, energy generation and storage applications (Stoller, Park, Zhu, An, & Ruoff, 2008),(Yoo et al., 2009). Such a remarkable material can be synthesized by various methods, for instance, mechanical exfoliation and cleavage (Park & Ruoff, 2009), chemical vapour deposition (Reina et al., 2009) and solvothermal method (Qian et al., 2009). However these methods have several hindrances like high energy need, low yield, and limitation of instrument. This hindrance can be circumvented *via* chemical method, which has become a promising route to produce GS with high yield and low-cost. Moreover, GS derived by this method contains a significant amount of oxygen functional groups and defects, which is essential in electrochemical biosensors application.

As illustrated in Figure 3.1 the above said approach, consists of three important stages, oxidation of graphite to graphite oxide (GO), followed by exfoliation into few-layered or monolayers of GOS, which could be achieved by sonicating in a suitable solvent. Finally, chemical reduction of GOS into RGO.

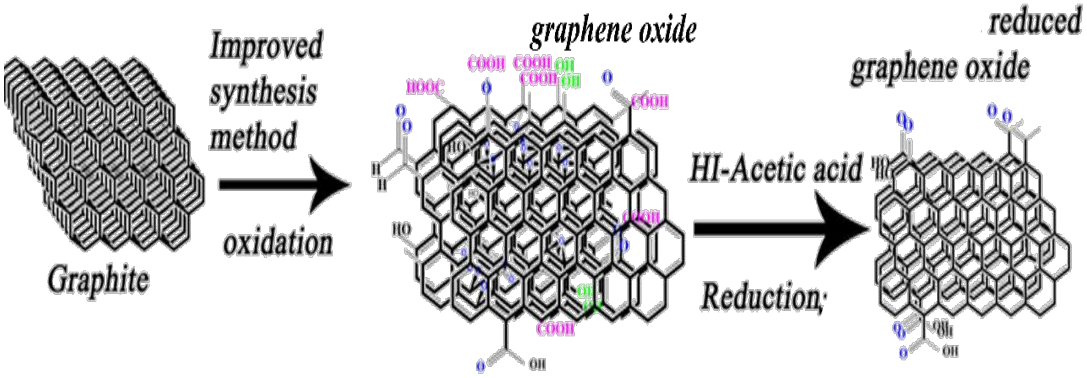

Figure 3.1 Schematic of synthesis of reduced graphene oxide

In spite of various functional groups and defects, the van der Waals interactions, tends RGO to form agglomerates or even restack to form graphite, which limits its potential application in the field of the electrochemical biosensors. This issue can be overcome by surface functionalization, which will prevent restacking, increase the surface area and enhance the dispersion of carbon-based nanomaterials in both aqueous and non-aqueous solvents. For the past few years, many research works have been reported on functionalization of RGO to prevent restacking and to introduce new desirable properties (Bianco, Losurdo, Giangregorio, Capezzuto, & Bruno, 2015).

Therefore, RGO can be functionalized by various approach *via* chemical, electrochemical treatment (Jokar, Shahrokhian, & zad, 2014), ball milling and polymer wrapping (Lim et al., 2015). Though, RGO functionalized by mentioned techniques may enhance the dispersion, due to the usage of strong acids, longer treatment time and high temperature, they have several drawbacks such as structural damage, properties degradation like the rigorous decrease in carrier mobility, drastic change in electronic structure and uncontrolled degree of functionalization. These drawbacks could be overcome by "dry" process, i.e plasma functionalization, which has proved to be an appropriate controlled technique for functionalizing RGO without altering the bulk properties and with no structural damage (Pourfayaz, Khodadadi, Mortazavi, & Jafari, 2010). Hence, this chapter focuses on surface functionalization of RGO *via* oxygen, nitrogen, and ammonia radio frequency (RF) plasma, its characterization and application of ammonia RF plasma functionalized RGO.

3.2 Plasma functionalization of RGO

The RGO obtained from graphite, was functionalized with low pressure plasmas generated by oxygen (O_2), nitrogen (N_2) and ammonia (NH_3) RF plasma, in the plasma reactor M-PECVD-1A [S] (M/s. Milman Thin Film Systems, Pune, India) illustrated in Figure 3.2. The reactor composed of a stainless-steel vacuum chamber consisting of two electrodes, provided with lateral window for optical inspection and connected to a rotary pump.

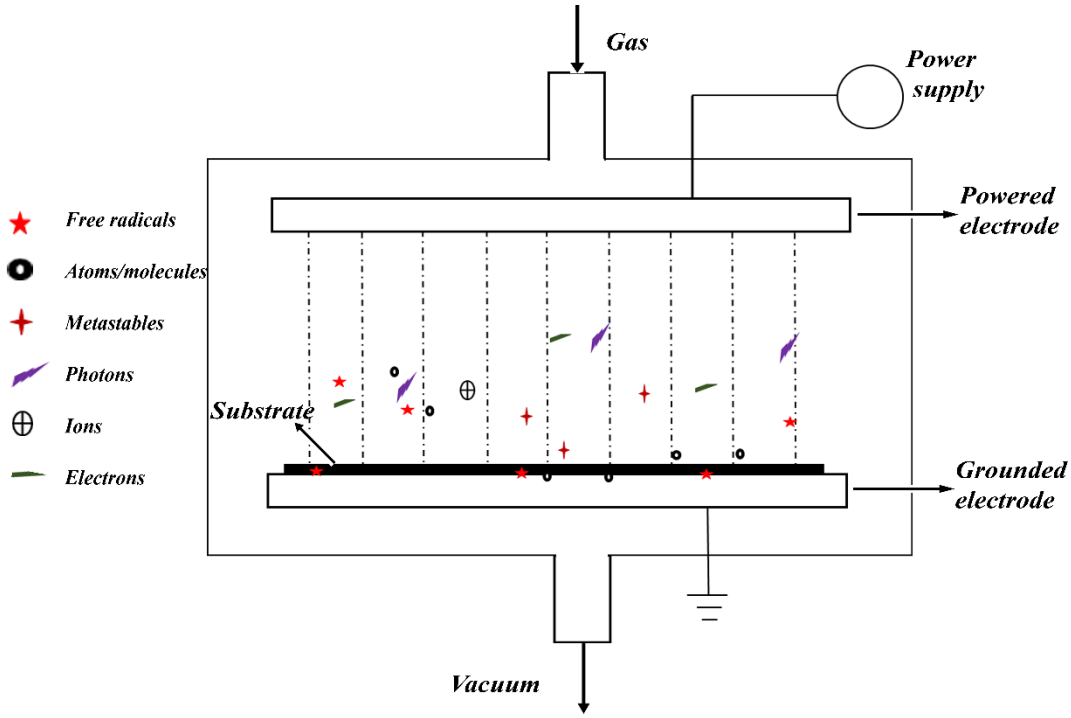

Figure 3.2 Schematic diagram of capacitively coupled reactor

The top electrode was connected to the RF power source and the bottom electrode was grounded. For functionalization, the sample is placed on stainless steel substrate holder on the bottom electrode. Then the system was evacuated to a pressure of 0.1 Pa. After achieving the base vacuum, the plasma functionalization was carried out using O_2, N_2, NH_3 gases, introduced through a mass flow controller at a specified flow rate. When the process pressure was stabilized, capacitively coupled RF plasma was generated between the two electrodes for a preset time of 10 min, at a fixed power 100 W, pressure 50 m Torr and flow rate 10 sccm. During O_2, N_2, and NH_3 plasma functionalization, the excited molecules and radicals generated in the plasma, interact with the sp^2-hybridized graphite-like C=C bond present on the surface of RGO and creates defects that act as prime sites

for functionalization with various chemical functional groups including carboxyl, amine, and hydroxyl groups.

3.3 Results and discussion

3.3.1 SEM

As illustrated in Figure 3.3 the morphology of graphite, GOS and RGO are investigated by SEM. From Figure 3.3 (a) the graphite shows the typical multi-layered structure. The morphology of GOS observed in Figure 3.3 (b) reveals its flaky structure obtained after oxidation of graphite. It is notable from the Figure 3.3 (c) that RGO obtained after reduction of GOS reveals its curled morphology consisting of thin paper-like structures.

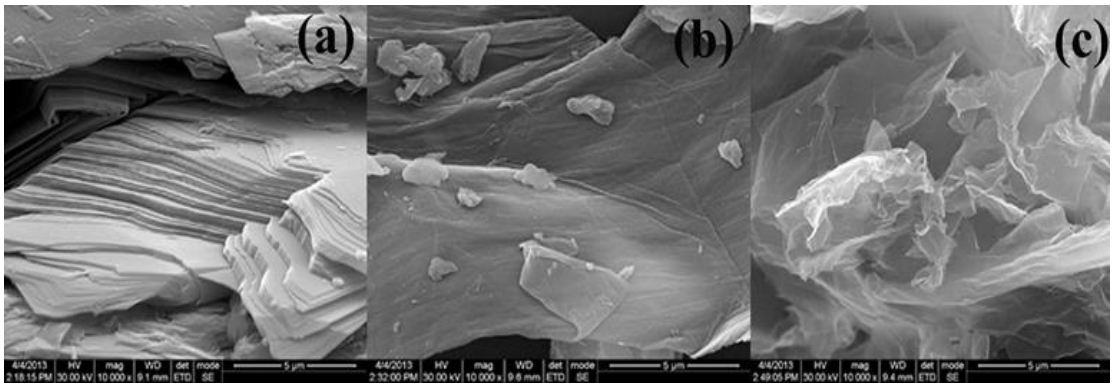

Figure 3.3 SEM images of (a) graphite flakes, (b) GOS and (c) RGO.

3.3.2 AFM

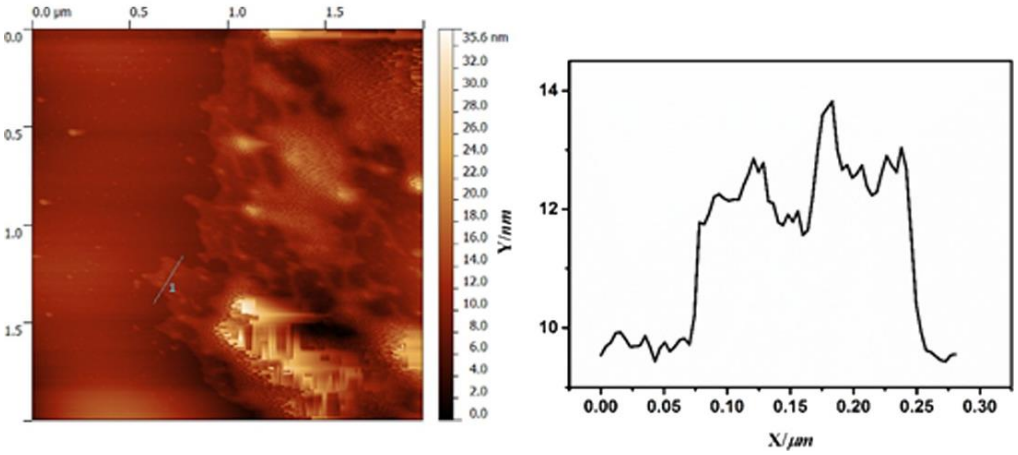

Figure 3.4 AFM image of RGO on mica surface with its height profile

The layer thickness and the topographical features of RGO were determined by AFM. This measurement was performed using silicon nitride cantilever. The sample was prepared by ultrasonicating RGO in ethanol at 0.05mg mL^{-1}. Figure 3.4 depicts the typical AFM image of RGO casted on mica sheet along with its

height profile. The analysis of the micrographs indicates the layer thickness of RGO around 3.6 nm which corresponds to a three-layer of RGO, which is consistent with the data reported in the literature (Paredes, Villar-Rodil, Solís-Fernández, Martínez-Alonso, & Tascón, 2009).

3.3.3 XRD

The crystalline phases of graphite, GOS, RGO and plasma functionalized RGO are investigated and illustrated in Figure 3.5. The obtained diffraction peaks were identified by comparing with the standard JCPDS data of graphite (JCPDS no. 23-64). The acquired XRD pattern illustrated in Figure 3.5 (a) reveals a sharp diffraction peak of graphite found around 2θ = 26° (002) with an interlayer spacing of 0.330 nm. After chemical oxidation of graphite flakes, the diffraction peak of GOS found around 10 ° (001) illustrated in Figure 3.5 (b) indicates exfoliation of the interlayer space of graphite from 0.330 to 0.817 nm, which is due to introduction of a number of oxygen-containing groups on both the basal and edge of each layer (Marcano et al., 2010). Subsequently, RGO obtained after chemical reduction of GOS, shows a broad peak at 2θ = 24.5° of (002) in Figure 3.5 (c) with the interlayer spacing of 0.370 nm, indicates a successful reduction of GOS into RGO.

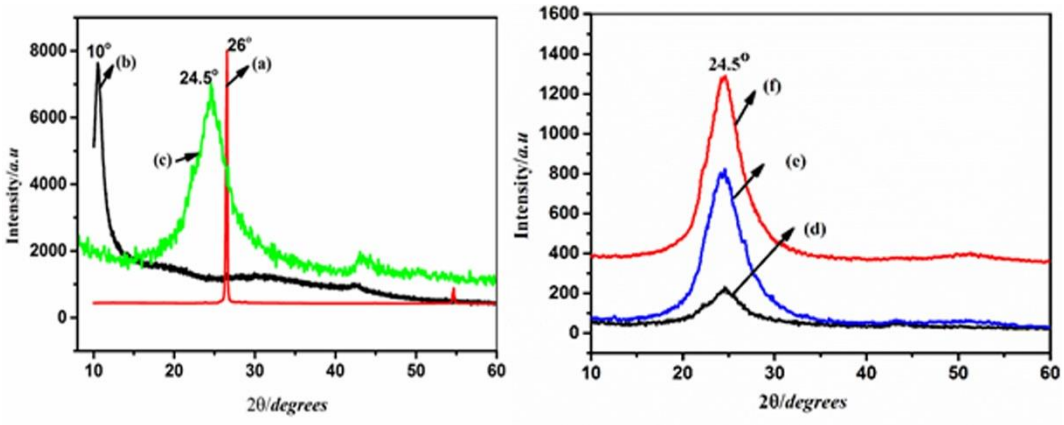

Figure 3.5 XRD pattern of (a) graphite, (b) GOS, (c) RGO, (d) RGO -O_2, (e) RGO -N_2 and (f) RGO -NH_3.

This broad peak indicated that the RGO is exfoliated into few layers of RGO with disordered stacking (Chao Xu, Yuan, & Wang, 2014). Moreover, the plasma functionalized RGO-O_2, RGO-N_2 and RGO-NH_3 display a diffraction pattern around 24.5° (Figure 3.5 (d, e, f), implying no significant change in crystalline phase after plasma functionalization. Furthermore, from full width half maximum

(FWHM) of RGO at (002) phase, the thickness of RGO is calculated using Debye Scherer formula.

$$t = \frac{0.89\,\lambda}{\beta \cos\theta} \longrightarrow (3.1)$$

This equation gives the relationship between diffraction peak full width half maximum (β) and thickness (t). The wavelength of the source used in x-ray is denoted by λ and θ denotes the angle of the peak. From the determined thickness, the number of layers is calculated by the formula given below

$$N = \frac{t}{d_{(spacing)}} \longrightarrow (3.2)$$

where, t is the thickness of graphene sheets, $d_{(Spacing)}$ is the interlayer spacing of particular plane. The number of sheets of reduced graphene oxide calculated was found to be 3, which is also confirmed by AFM.

3.3.4 Raman Spectroscopy

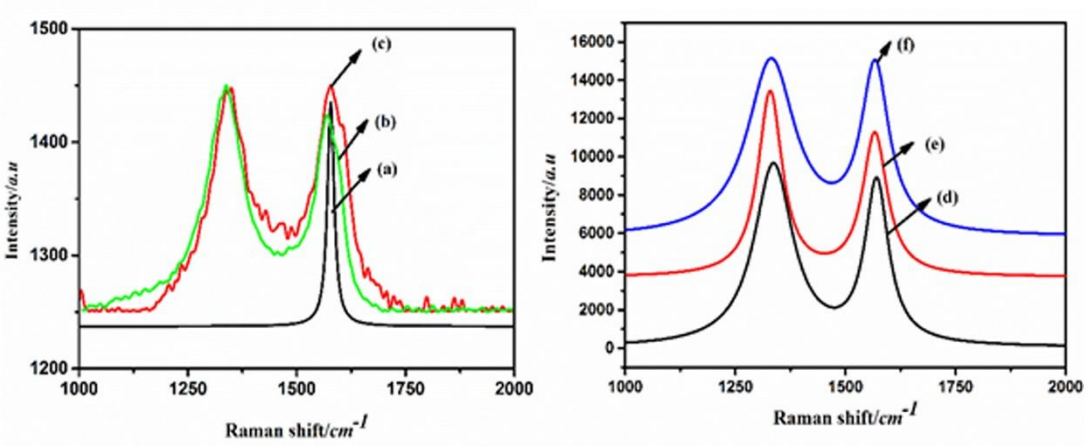

Figure 3.6 Raman spectra of (a) graphite, (b) GOS, (c) RGO, (d) RGO-O_2, (e) RGO-N_2 and (f) RGO-NH_3

Raman spectroscopy has been accepted as a very versatile and purely optical technique used to glean information regarding the degree of disorder in GS materials, where the relative D-band and G-band peak intensities (I_D/I_G) reflect the general density of defects in the sp^2 lattice. As seen in Figure 3.6, there are two characteristic peaks in the spectrum of raw graphite, namely, the D band at 1330 cm^{-1} and the G band at 1580 cm^{-1}. The D band ascribed to edges, other defects, and disordered carbon, while the G band arises from the zone centre E_{2g} mode, corresponding to ordered sp^2-bonded carbon atoms (Ferrari & Basko, 2013). The

absence of D band in Figure 3.6 (a) indicates defect free graphite material. During the oxidation of graphite several defects are introduced in sp^2 - hybridized carbon sheets; therefore an increase in D-band peak intensity and broadening of G-band occurs in the Raman spectra of GOS. As depicted in Figure 3.6(c), with subsequent reduction of GOS by hydroiodic acid, the intensity ratio of D/G increased significantly. This result could be ascribed to restoration of numerous sp^2 domains from amorphous regions of GOS, which gives rise to stronger D band signal (Abdolhosseinzadeh, Asgharzadeh, & Seop Kim, 2015). Further increase in (I_D/I_G) ratio from 1.0 => RGO, 1.1=> RGO-N_2, 1.2=> RGO-O_2 and 1.2=> RGO-NH_3 illustrated in Figure 3.6 (d, e and f) evidenced the introduction of defects after plasma functionalization.

3.3.5 FTIR

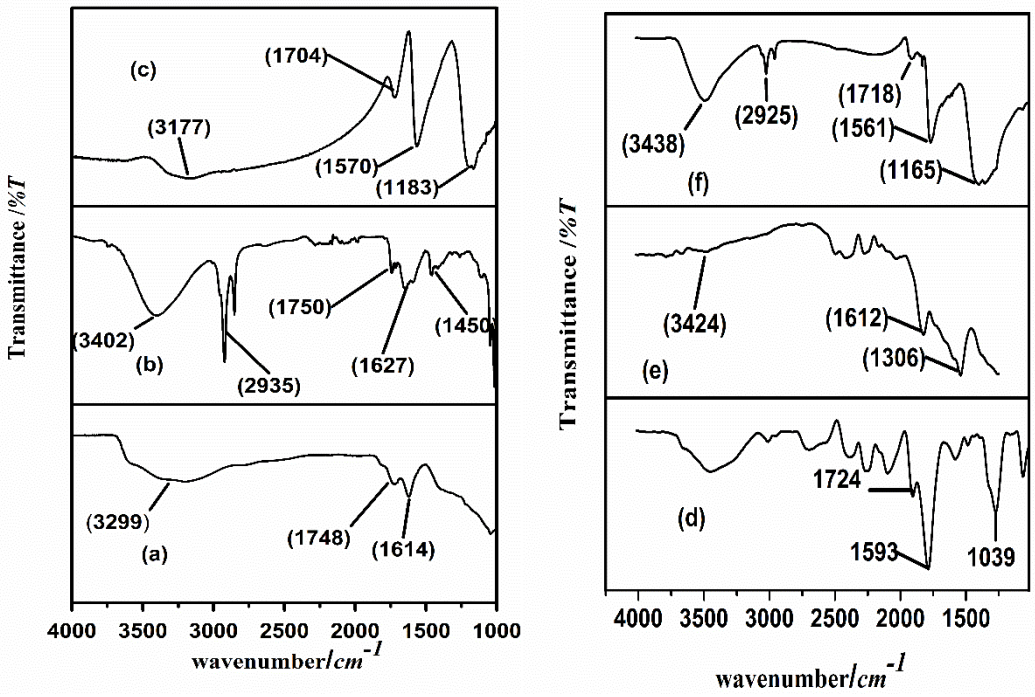

Figure 3.7 FTIR spectra of (a) graphite, (b) GOS, (c) RGO, (d) RGO-O_2, (e) RGO-N_2 and (f) RGO-NH_3

The FTIR spectra illustrated in Figure 3.7 are used to investigate the surface chemistry of graphite, GOS, RGO, RGO-O_2, RGO-N_2 and RGO–NH_3. The spectrum of graphite (Figure 3.8(a)) had broad absorption bands at 3299 and 1748 cm^{-1} corresponding to O-H and C=O stretching vibrations, respectively. Moreover, peak at 1614 cm^{-1} is related to aromatic C=C stretching. The exfoliation of graphite is confirmed from IR spectrum with various oxygen and hydroxyl groups (Figure

3.7(b)). IR peaks at 3402 and 2927 cm^{-1} corresponding to O-H stretching and due the asymmetric and symmetric CH_2 stretching, respectively. Moreover, the peaks around 1627 and 1750 cm^{-1} are attributed to C=C stretches from un-oxidized graphitic domain and C=O stretch of carboxyl group, respectively.

In the case of RGO, the IR spectrum illustrated in Figure 3.7(c), reveals that the intensities of all the peaks corresponding to the oxygen moieties of RGO decreased as compared to the intensities of peaks in GOS, but the peaks had not disappeared. This indicates the partial reduction of GOS. The effective oxygen functionalization of RGO-O_2 illustrated in Figure 3.7(d) was evidenced by increased intensity of carbonyl, epoxy and hydroxyl groups. Moreover, the nitrogen functionalized RGO by N_2 and NH_3 plasma is evidenced by the two distinct sharp peaks depicted in Figure 3.7 (e) and f at 3431 and 1166 cm^{-1} attributed to N-H and C-N stretching, respectively. The other peaks at 1718, 1561 and 2923 cm^{-1} correspond to C=O, C=C and C-H stretching vibration of chemisorbed hydrogen respectively are also observed.

3.3.6 XPS

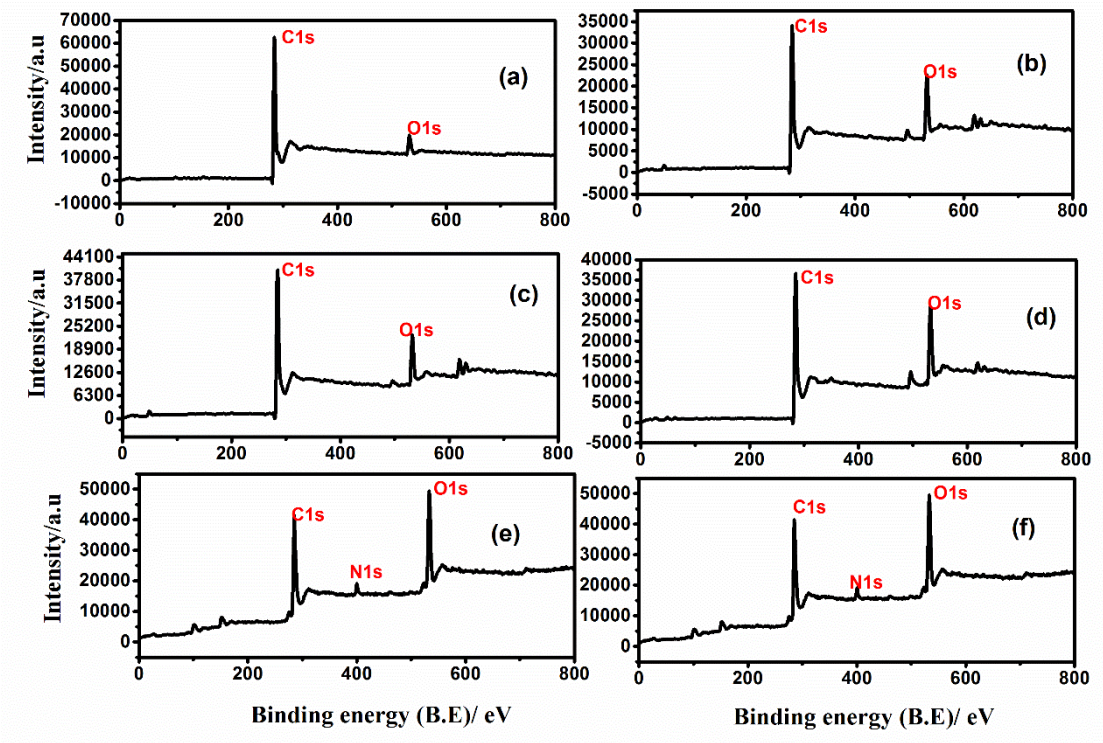

Figure 3.8 XPS survey scan spectrum of (a) graphite, (b) GOS, (c) RGO, (d) RGO-O_2, (e) RGO-N_2 and (f) RGO-NH_3

The detailed elemental composition and quantitative analysis of various functional moieties in graphite, GOS, RGO, RGO-O_2, RGO-N_2 and RGO-NH_3 are further elucidated by XPS. The survey spectrum illustrated in the Figure 3.8, reveals the presence of C, O and N at ~284.7 eV, ~532.1 eV and ~398.2 eV respectively. The high resolution spectra of C1s of all the samples depicted in the Figure 3.8 can be deconvoluted into four main peaks such as C=C (284.6 eV), C-O (286.7 eV), C=O (287.9 eV) and COOC (290.6 eV) (Abdolhosseinzadeh et al., 2015; Changyan Xu et al., 2015).

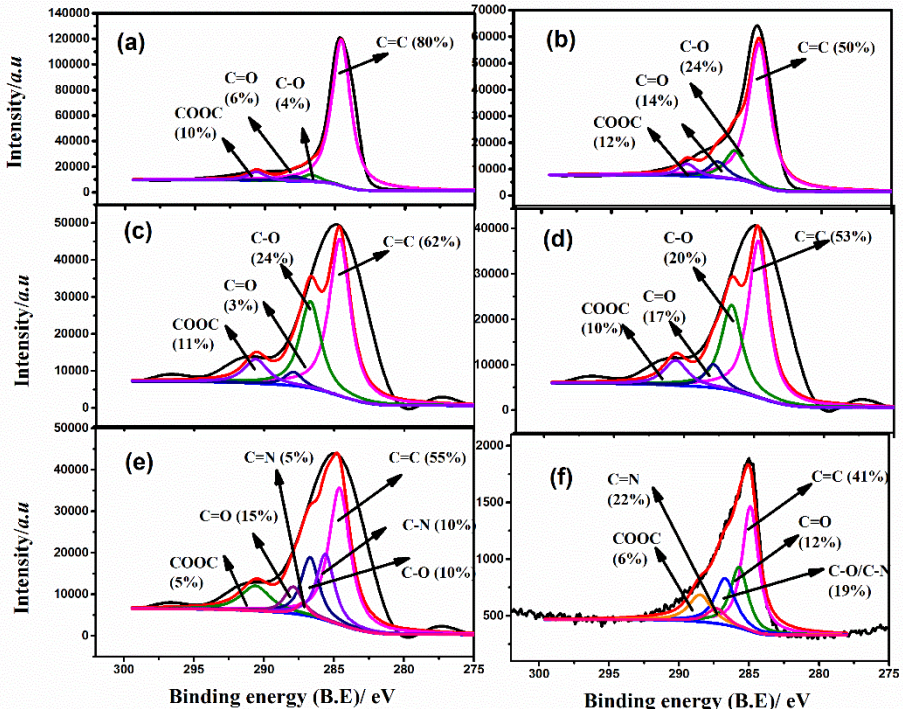

Figure 3.9 C1s High resolution spectra of (a) graphite, (b) GOS, (c) RGO, (d) RGO-O_2, (e) RGO-N_2 and (f) RGO-NH_3

Various oxygen moieties introduced during oxidation of graphite, increase the concentration of C-O, C=O and COOC and thereby reduced the concentration of C=C. Increase in concentration of C=C along with decrease in the concentration of oxygen moieties demonstrated the reduction of GOS. Incorporation of various oxygen moieties introduced during O_2 plasma functionalization was evidenced by decrease in graphitic carbon from 62.3 to 41.5% and increase the percentage of C-O and C=O. Furthermore, two significant peak in RGO -N_2 and RGO -NH_3 at 285.7

and 287.3 eV corresponding to C-N and C=N confirmed the incorporation of nitrogen atoms in RGO during N_2 and NH_3 plasma functionalization.

The high-resolution N1s spectra of RGO -N_2 and RGO -NH_3 illustrated in Figure 3.10 can be deconvoluted into four components, revealing that the nitrogen atoms incorporated during ammonia plasma treatment resulted in the formation of N=C (397.9 eV), C-NH_2 (399.7 eV), C-N-C (400.9 eV) and C-N^+-C or graphitic nitrogen (402.8 eV) (S.-M. Li et al., 2013; Sheng et al., 2012).

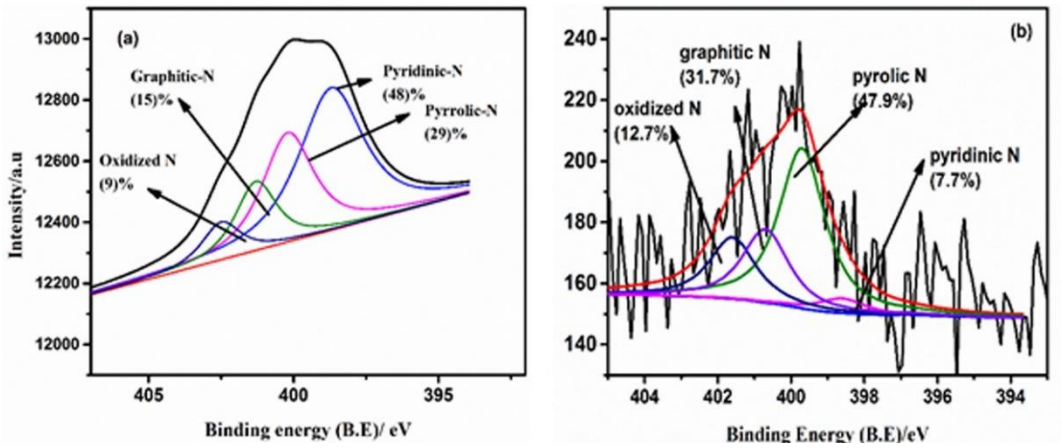

Figure 3.10 N1s High resolution spectra of (a) RGO-N_2 and (b) RGO -NH_3

Pyridinic and pyrrolic groups represent nitrogen atoms bonding with two carbon atoms, graphitic N also called “quaternary nitrogen”, refers to nitrogen atoms that substitute the carbon atoms in RGO and a nitrogen oxide peak at >402 eV.

3.3.7 TEM

TEM images of RGO, RGO-O_2, RGO-N_2 and RGO-NH_3 depicted in Figure 3.11 reveals the typical wrinkled structure of RGO in Figure 3.11 (a) with corrugation. No observable change in the surface morphology was observed after plasma functionalization. Further, investigation on the SAED patterns of all the four samples (Figure 3.10 (d), (e) and (f)) confirmed that there is no change in the diffraction pattern before and after plasma treatment, supporting that the crystalline structure remains unaltered.

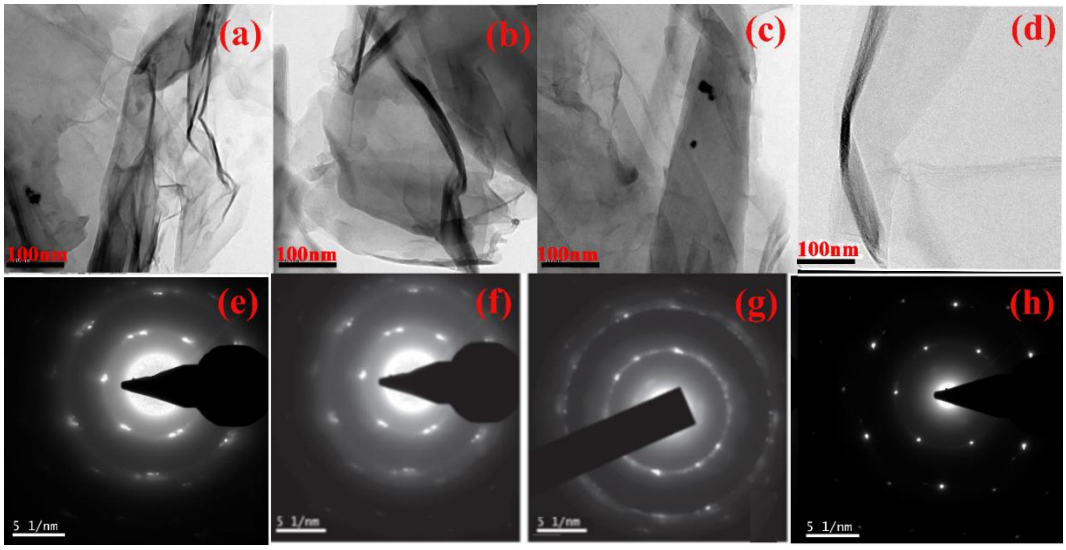

Figure 3.11 TEM images of (a) RGO, (b) RGO-O_2, (c) RGO-N_2 and (d) RGO-NH_3 with (e)–(h) respective SAED pattern

3.3.8 OES

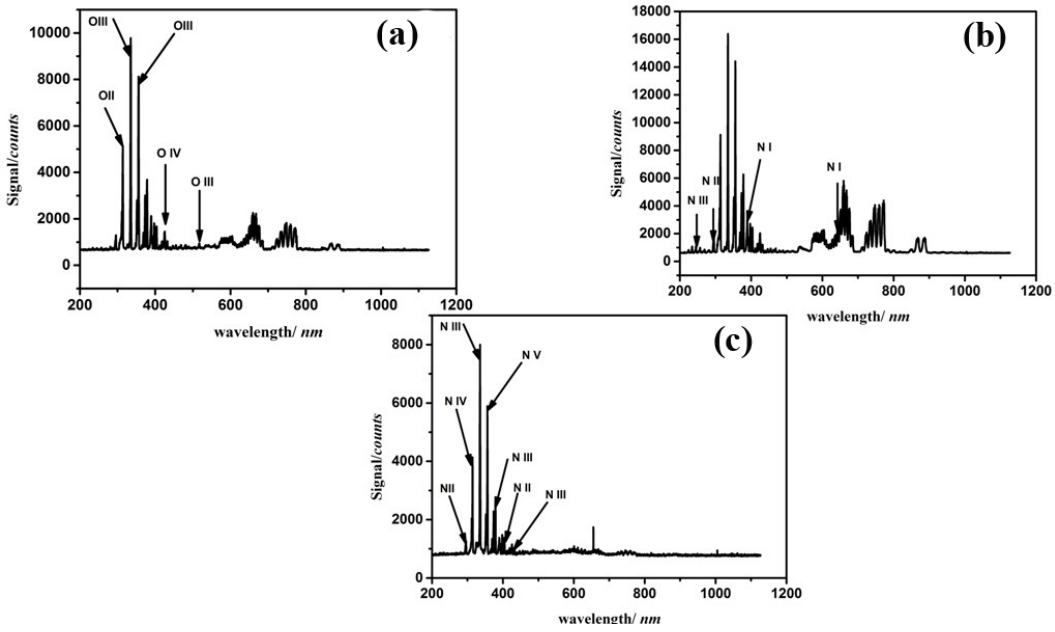

Figure 3.12 OES spectra of (a) oxygen, (b) nitrogen and (c) ammonia plasma.

The ionized species generated during O_2, N_2 and NH_3 RF plasma functionalization were investigated through OES (Figure 3.12). The acquired emission spectra were in the wavelength range of 300–1000 nm with an integration time of 5 s. The spectra illustrated in Figure 3.12 (a) reveal various ionized oxygen generated during O_2 plasma. The first, second, third and fourth ionized oxygen spectral features observed in 334.8, 313.8, 355.6 and 351.4 nm correspond to atomic transition 3s 5S-5p 5P, 3p 4D°-4s 4P, 3s' ^{3}P-3p' ^{3}P° and 6d ^{2}D-7p ^{2}P°, respectively. And also a

triplet peak corresponding to first ionization oxygen is observed at 777 nm. The relative intensity of neutral oxygen at 334.8 nm was very low, which is 1, as compared to oxygen at second and third ionization states which have the relative intensities of 332 and 688, respectively.

In the case of N_2 plasma, OES spectrum depicted in Figure 3.12(b) reveals a triplet peak observed at 767 nm corresponds to first ionization is N1. The first ionized nitrogen (N I) observed at 389.2 nm with a relative intensity of 9 has the atomic transition 3s ^{2}P-5p ^{2}D°. The second ionization of nitrogen (N II) observed at 295.5 403.7 and 636.6 nm correspond to atomic transition 3d ^{3}D°-5f', 3d ^{3}F°-4f', 3s ^{3}P°-3p ^{1}P, respectively are observed with the respective relative intensities of 7, 31 and 1.

Various nitrogen ionized species generated during ammonia plasma was investigated from the Figure 3.12 (c). It reveals the presence of second ionized nitrogen (N II) observed at 296.0 and 404.353 nm corresponds to atomic transition 3d ^{3}D°-5f' and 3d ^{3}F°-4f', respectively. Third, fourth and fifth ionized nitrogen (N III, N IV and N V) spectral feature with the respective relative intensities of 490, 60 and 11 observed at 335.3, 314.2 and 35.9 nm, correspond to atomic transitions of 3p' 4P°-3p' 4P, 3p' ^{3}D-4f ^{3}F°and 7d ^{2}D-10p ^{2}P°, respectively.

3.3.9 Electrochemical characterization

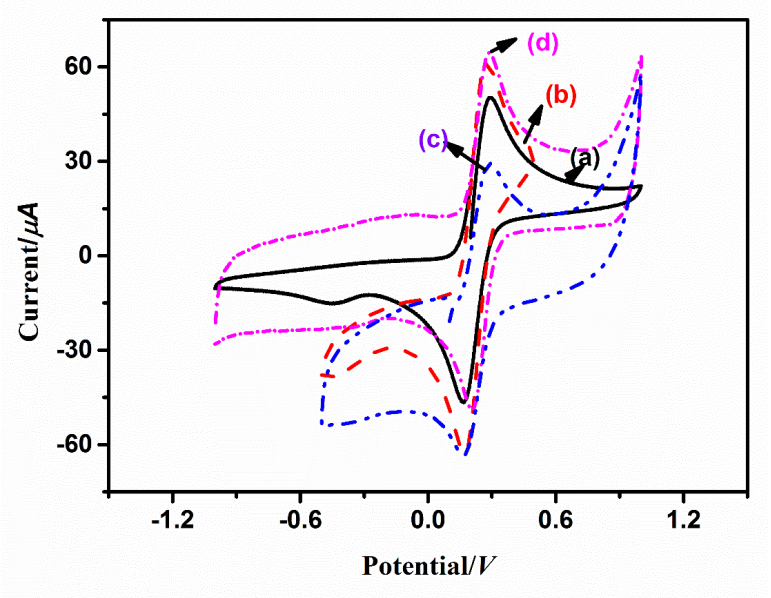

Figure 3.13 CV of (a) RGO, (b) RGO-N_2, (c) RGO-O_2 and (d) RGO-NH_3 in 5mM ferro cyanide at 100 mV/s scan rate.

The electrocatalytic property of the modified electrodes was studied and illustrated in Figure 3.13 by performing CV using 5 mM ferro cyanide as electrolyte under the scan rate of 100 mV/s. The modified electrodes were prepared by drop casting 7 µL of RGO, RGO-O_2, RGO -N_2 and RGO-NH_3 suspension in ethanol and dried at room temperature for 12 h. Among the modified electrodes, due to presence of abundant defects and nitrogen atom introduced during ammonia plasma functionalization, RGO-NH_3 shows higher oxidation peak current and minimum potential difference i.e ΔE_p value, indicating enhanced electrocatalytic activity.

Herein, RGO functionalized with NH_3 plasma, having various functional reactive groups such as amino, amine and other nitrogen moieties enhanced electrocatalytic property. It was applied to investigate the direct electron transfer (DET) of redox protein hemoglobin (Hb).

3.4 Application of NH_3 plasma functionalized RGO in DET studies

Hb is a quarternary structured iron-containing oxygen-transport metalloprotein, consisting of four globular proteins, each associated with a heme group containing an iron (Fe) at the Hb centre, is a preferred model for the DET of a redox protein (Xianbo Lu, Zou, & Li, 2007). In recent times, DET between Hb and electrode surface has received tremendous attention not only to understand the thermodynamic and kinetic properties of protein, but also to design label free biosensors (Gorton et al., 1999). On the contrary, electroactive sites buried in Hb hinders the DET with the electrode. It is often a challenge to identify a potential electrode material that enables DET with the electroactive sites in protein, while retaining the protein structure and activity on electrode material. Various chemically modified electrode materials have been developed for studying the electron transfer of Hb including mesoporous carbon (Feng, Xu, & Chen, 2007), silica thin films, membranes, metal nanoparticles and graphene nanosheets (GS) (Geim & Novoselov, 2007). Amid of the modified electrodes, extensive research works have been performed on the GS modified by incorporating functional moieties such as hetero atom, metal or metal oxide nanoparticles, polymers and other functional moieties can tune the electronic property of GS by increasing the free charge carriers, thereby enhancing conductivity (Xueqing Gao et al., 2015).

Meanwhile, due to the beneficial properties of Hb modified electrode, several research work have been conducted to develop biosensors using Hb for the determination of nitrite (NO_2^-). Nitrite used as preservative and additive in food, can interact with the blood, may results in methaemoglobinaemia, which leads to a condition called "blue baby syndrome." It also has the ability to interact with amines and proteins to generate highly carcinogenic N-nitrosamines, which will enhance the possibility of cancer and hypertension (P. Li, Ding, Wang, et al., 2013), (Fu et al., 2013).

In this section to study the DET between Hb and RGO-NH_3 , we fabricated Hb modified RGO -NH_3 electrode by directly immobilizing 10.0 µL of 15.0 mg/mL Hb on the modified electrode GCE/RGO-NH_3 and we investigate the bio-electrocatalytic activity towards nitrite reduction (Y. Chen et al., 2008), (P. Li, Ding, Lu, et al., 2013).

3.5 Results and Discussions

3.5.1 Electrochemical characterization

Often, the transfer of electron between the chemical species and the modified electrode was studied using the outer sphere redox species such as $[Ru(NH_3)_6]^{3+/2+}$. Figure 3.14 (A) illustrates the CV of 1.0 mM $[Ru(NH_3)_6]^{3+/2+}$ in 1.0 M KCl at GCE, GCE/RGO and GCE/RGO-NH_3. The corresponding peak potential separation (ΔE_p) values were found to be 88 ± 1.7 mV (N=5), 84 ± 1.1 mV (N=5) and 66 ± 1.5 mV (N=5). A lower ΔE_p indicates a fast electron transfer and readily available unoccupied energy states for electron transfer at the GCE/RGO-NH_3 than at the GCE/RGO and bare GCE.

On the other hand, the surface active sites of the electrode were studied using the inner sphere redox probe $[Fe(CN)_6]^{3-}$. Figure 3.14(B) is the representative CV of 4.0 mM ferricyanide in 1.0 M KCl at GCE, GCE/RGO and GCE/RGO -NH_3 and their corresponding ΔE_p values are 95 ±1.3 mV, (N=5), 84±1.7 mV, (N=5) and 63±1.5 mV, (N=5) respectively. The lower ΔE_p value of RGO -NH_3 is due to the introduction of more electroactive sites (as a result of nitrogen incorporation) to facilitate charge transfer, thereby resulting in a higher electrochemical performance of RGO-NH_3 with current values of 51, 62 and 71 µA that corresponds to GCE, GCE/RGO and GCE/RGO -NH_3, respectively.

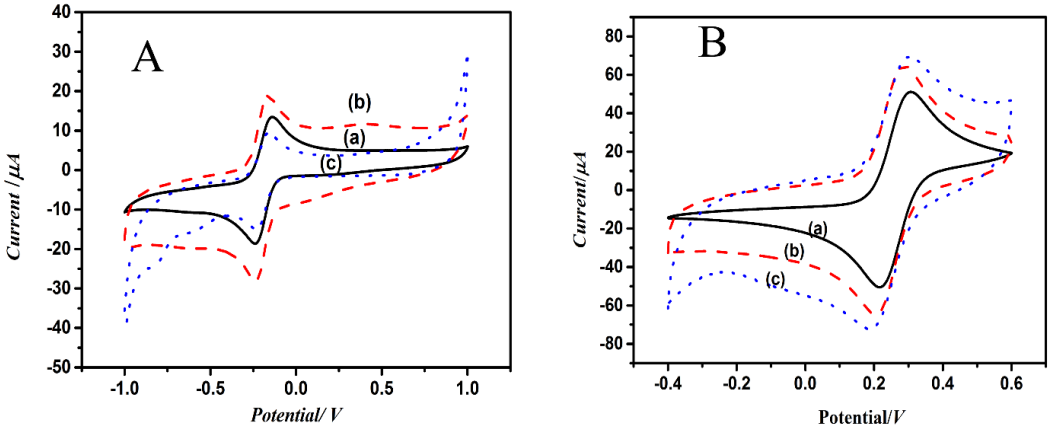

Figure 3.14 CV of (A) 1.0 mM $[Ru(NH_3)_6]^{3+/2+}$in 1.0 M KCl, (b) 4.0 mM $[Fe(CN)_6]^{3-/4-}$ in 1.0 M KCl, at a scan rate of 100 mV/ s at (a) GCE (b) GCE/RGO and (c) GCE/RGO -NH_3.

3.5.2 Characterization of RGO-NH_3/Hb composite film

The distribution of charge can be evaluated from the Zeta potential values. The Zeta potential for RGO and RGO -NH_3 was found to be 0.139 mV and -27.5 mV. Compared to RGO the negative surface charged RGO -NH_3 can strongly interact with hemoglobin and thereby pulls more Hb towards RGO -NH_3 surface.

The immobilization of Hb onto the surface of RGO -NH_3 was confirmed by FTIR measurements. From Figure 3.15 (A), it was evident that the peak at 1700–1600 cm^{-1} resulted from the C=O stretching vibration of peptide linkages in the backbone of protein and the peak at 1620– 1500 cm^{-1} was due to the combined N–H bending and C–N stretching (George & Hanania, 1953). The presence of peaks at 1637 and at 1543 cm^{-1} for RGO -NH_3/Hb composite film, is in good agreement with the peaks obtained for native Hb (Figure 3.15A (a)), confirmed that the protein did not suffer any de-naturation and demonstrated the biocompatibility of RGO -NH_3 (Figure 3.15A (b)). UV–Vis spectroscopy is also an effective way to investigate the stability of Hb immobilized on RGO -NH_3. The Soret absorption bands of heme proteins provide information about the conformational integrity of the proteins. As shown in (Figure 3.15 B), the Soret absorption band of Hb immobilized on RGO-NH_3 is located at 405.7 nm, which is close to that of native Hb at 406.2 nm, indicating that Hb retained the essential features of its conformational integrity. This reveals that RGO-NH_3 has biocompatibility and did not suffer protein denaturation.

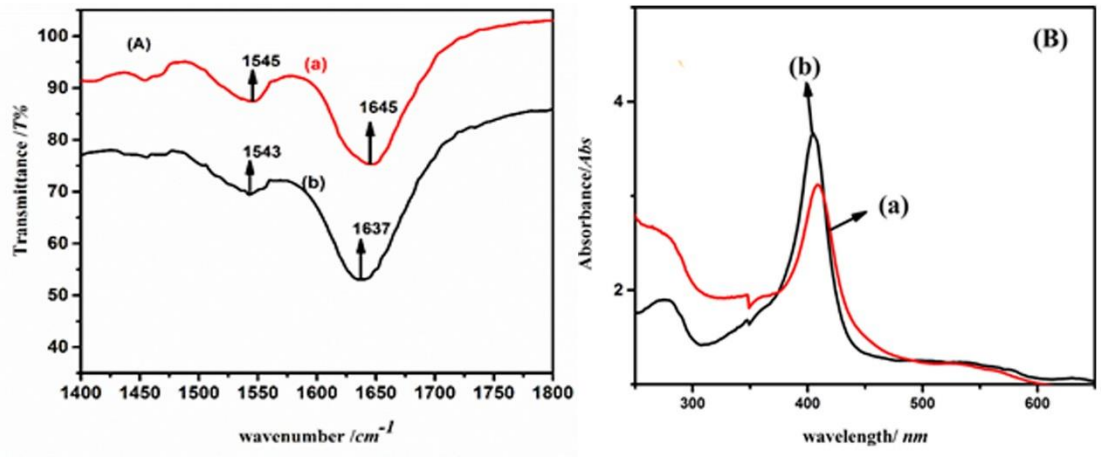

Figure 3.15(A) FT-IR spectra and (B) UV-Vis of (a) Hb and (b) RGO -NH_3/Hb.

3.5.3 Effects of solution pH on direct electron transfer of GCE/RGO-NH_3/Hb

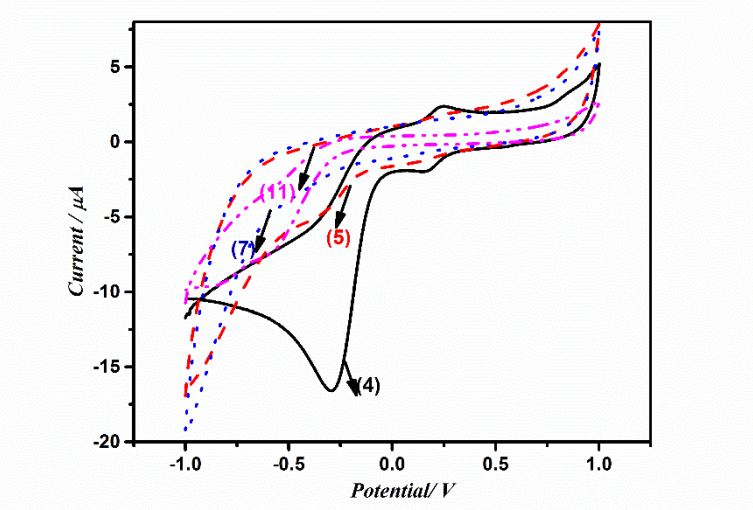

Figure 3.16 CV of GCE/RGO -NH_3/Hb in PBS (pH = 4, 5, 7, and 11) (Scan rate: 100 mV/s)

It is well-known that most heme proteins exhibit a pH dependent conformational equilibrium and thereby it is expected that the pH of the phosphate buffered saline (PBS) would influence their electrochemical reactions. Herein, we have investigated the effect of pH on the electrochemical response at GCE/RGO -NH_3/Hb in pH ranging from 4.0 to 11.0 (Figure 3.16). From our results, it is evident that the electrochemical performance is excellent at pH 4.0 and therefore this pH was opted for further investigation.

3.5.4 Direct electrochemistry of Hb

Figure 3.17 is the representative CV of 0.1 M PBS (pH 4.0) at various electrodes at a scan rate of 100 mV/s. From CV, it is evident that there are no redox peaks noticed at (a) GCE, (b) GCE/Hb, (c) GCE/RGO, (d) GCE/RGO-NH_3 and (e) GCE/RGO/Hb

thereby confirming the electrochemically inactive nature of the above mentioned platforms towards Hb. Redox peaks of Hb were difficult to observe at the above mentioned electrode materials other than GCE/RGO-NH_3/Hb electrode, since Fe is deeply buried in a cavity and not easily accessible for direct electron transfer reaction at the electrode surface. A well-defined reduction peak was observed for (e) GCE/RGO-NH_3/Hb on the cathodic scan (at − 0.285 V) indicating the reduction of Fe^{III} to Fe^{II} with an irreversible electron transfer process (Baccarin et al., 2016). It indicated that availability of abundant (47.9%) pyrrolic N group, large surface-to-volume ratio with good biocompatibility of RGO-NH_3 enhance the protein adsorption and promote direct electron transfer between redox protein by accelerating the electron transfer between matrix and Hb, leading to a more rapid current response for Hb at the electrode surface.

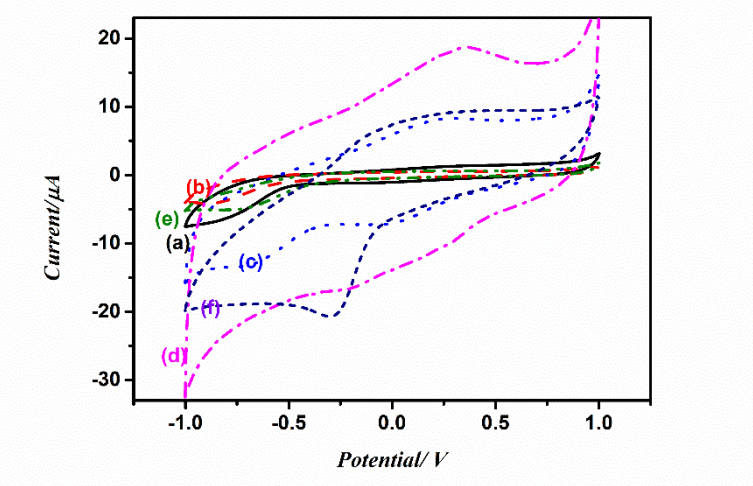

Figure 3.17 CV of (a) GCE, (b) GCE/Hb, (c) GCE/RGO, (d) GCE/RGO-NH_3, (e) GCE/RGO/Hb and (f) GCE/RGO-NH_3/Hb electrodes in pH 4.0 phosphate buffer solution at the scan rate of 100 mV/s.

3.5.5 Effect of scan rate

The influence of scan rate on the voltammetric response of GCE/RGO-NH_3/Hb is shown in Figure 3.18(a). The linear relationship between the cathodic peak currents and scan rate obtained in the range of 10 to 100 mV s^{-1} indicates a typical surface-controlled electrochemical behaviour illustrated in Figure 3.17(b). The surface concentration of electroactive species (Γ_c) in mol cm^{-2} can be calculated by the equation:

$$I_p = \frac{n^2F^2\nu A\Gamma_c}{4RT} \quad \text{---------- (3.1)}$$

where *v* is the sweep rate, A is the geometrical surface area of electrode and the other symbols have their usual meaning. From the slope of cathodic peak current vs. scan rate, the calculated surface concentration of Hb is 1.42×10^{-9} mol cm^{-2} which was larger than the theoretical monolayer coverage (1.89×10^{-11} mol/cm^2) (S.-F. Wang et al., 2005).

The larger surface area and better biocompatibility of RGO-NH_3 exhibits stronger hydrogen bonds interactions with Hb, which contribute to a higher surface coverage of GCE/RGO-NH_3/Hb and is in excellent agreement with the already reported GS/Hb modified electrodes in the literature (W. Sun, Dong, et al., 2014).

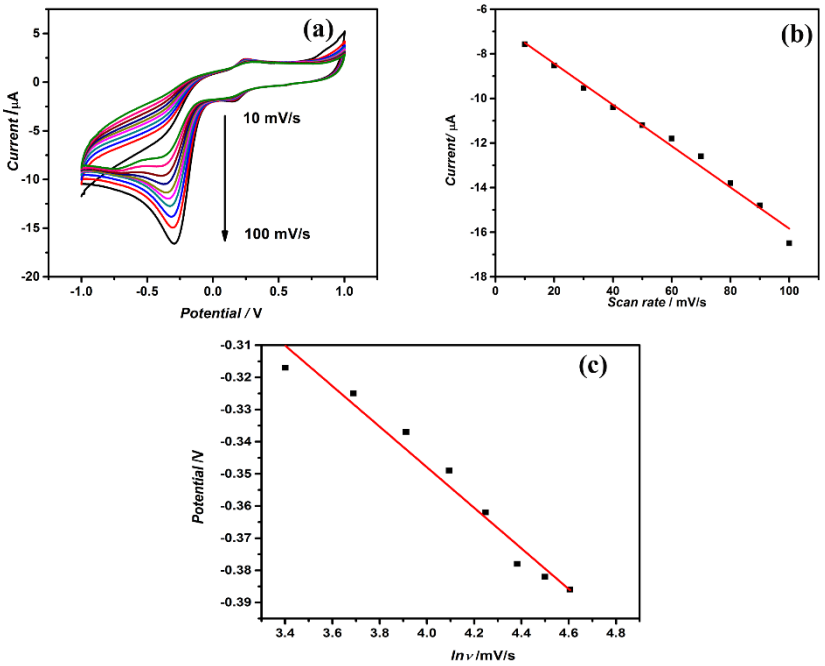

Figure 3.18 (a) CV of GCE/RGO-NH_3/Hb in pH 4.0 PBS with different scan rates (10-100 mV s^{-1}); (b) plot of I_{cp} against υ (c) the relationship of E_p against lnυ.

From the plot (E_p vs ln υ) illustrated in Figure 3.18(c), we noticed shift in peak potentials with respect to increase in the scan rate. The redox peak potentials exhibited a linear relation with log scan rate (ln υ) in the range from 10 to 100 mV s^{-1} (as shown in Figure 3.18(c)).

The electron transfer coefficient (α) can be obtained by the equation (3.2).

$$E_{p/2} - E_p = 1.875\ \frac{RT}{\alpha F} \longrightarrow (3.2)$$

where $E_{p/2}$ is the half wave potential, E_p is the reduction potential, R, T and F have their usual meanings. From the obtained α value (0.43) the electrochemical parameters such as heterogeneous electron transfer rate constant (k_s) and number of electrons (n) for immobilized Hb onto GCE/RGO-NH_3 were calculated using Laviron`s equation (Laviron, 1974, 1979).

$$\frac{RT}{\alpha nF} = \text{slope}\left(E_p \text{vs} \ln(v)\right) - - - - - - \longrightarrow (3.3)$$

$$k_s = \frac{\alpha nF}{RT}\text{slope}\left(E_p \text{vs} \ln(v)\right) - - - - - - - - \longrightarrow (3.4)$$

where υ is the scan rate. Based on the equation (3.2), the value of n was estimated as 0.99, suggesting one electron was involved in the reaction. The values of α and k_s were calculated as 0.43 and 1.05 s^{-1}, indicating that the GCE/RGO-NH_3/Hb provided a suitable microenvironment for promoting the electron transfer rate of Hb at the underlying electrode surface.

The obtained k_s value was larger than the reported values of Hb immobilized on GS/titanium dioxide nanorods composite (0.69 s^{-1}) (W. Sun, Guo, et al., 2013) , graphene oxide and ionic liquid composite film (0.92 s^{-1}) (W. Sun, Gong, et al., 2014) , GS and multi-walled carbon nanotubes (MWCNT) (0.97 s^{-1}) (W. Sun, Cao, et al., 2013), C_{60}–MWCNT composite film (0.39 s^{-1}) (Hua Zhang, Fan, & Yang, 2006), MWCNT film (0.58 s^{-1}) (Qi, Zhang, & Li, 2006), and GS/Fe_3O_4/Hb/GCE (0.3 s^{-1}) (C. Yu et al., 2013).

3.5.6 Detection of Nitrite

Increase in nitrite concentration beyond its maximum level in human beings can irreversibly convert hemoglobin to methemoglobin and cause hemoglobin to lose oxygen uptake and its transport capability. To investigate the electrocatalytic activity of Hb modified electrodes towards nitrite reduction, CV was performed and the obtained results are illustrated in Figure 3.19. No significant redox response was observed on both GCE/RGO/Hb and GCE/RGO-NH_3 modified electrodes (voltammogram "a & d") in the presence of nitrite, which indicates that these electrodes do not facilitate the reduction of NO_2^-. However, GCE/RGO -NH_3/Hb in the absence of $NaNO_2$ shows a reduction peak at -0.285 V vs. Ag/AgCl, which could be ascribed to DET between Hb and the underlying electrode, in PBS at pH 4 (voltammogram b). Upon addition of $NaNO_2$, Hb immobilized on GCE/RGO-

NH_3 acts as an effective catalyst towards reduction of NO_2^- which yields [Hb Fe(II) $(NO)^+]^+$, with a new irreversible reduction peak at − 0.675 V (voltammogram c), which was attributed not from reduction of NO_2^- but from the [Hb Fe(II) $(NO)^+]^+$ nitrosyl adduct. Further increase in potential reduces NO to N_2O with the release of water molecule.

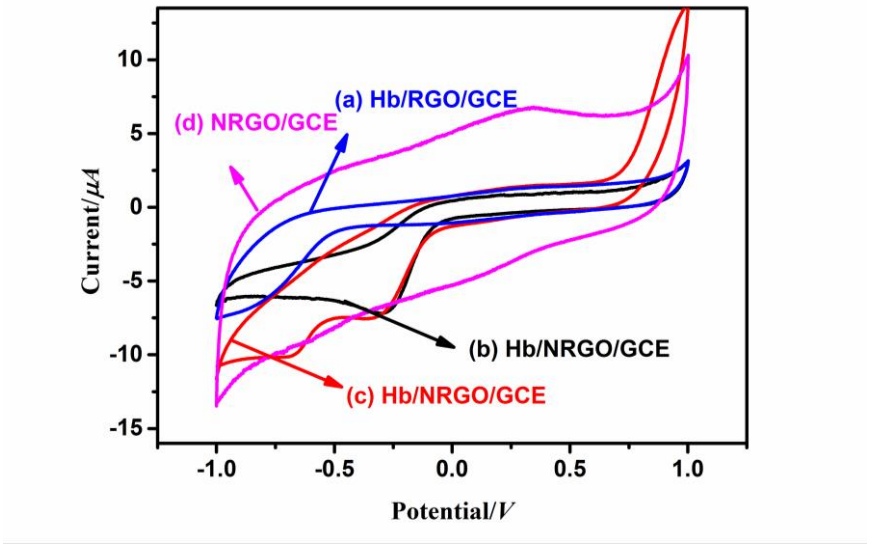

Figure 3.19 Cyclic voltammograms of (a) GCE/RGO/Hb, (c) GCE/RGO-NH_3/Hb and (d) GCE/RGO-NH_3 in presence of nitrite 1.0 mM $NaNO_2$, (b) GCE/RGO-NH_3/Hb in the absence of nitrite.

The mechanism of the electrocatalytic reduction of nitrite at Hb immobilized on GCE/RGO-NH_3 can be the following (Hui Liu et al., 2015).

Hb (Fe^{III}) $+e^- \longrightarrow$ Hb (Fe^{II}) (3.5)

Hb (Fe^{II}) + HNO_2 + H^+ $\longrightarrow$ [Hb (Fe^{II})-NO]$^+$ + H_2O (3.6)

[Hb (Fe^{II})-NO]$^+$ + $e^- \longrightarrow$ [Hb (Fe^{II})-NO] (3.7)

[Hb (Fe^{II}) -NO] $+e^- \longrightarrow$ [Hb (Fe^{II})-NO]$^-$ (3.8)

[Hb (Fe^{II}) -NO]$^-$ + $H^+ \longrightarrow$ Hb (Fe^{II}) + HNO (3.9)

$2HNO \longrightarrow N_2O + H_2O$ (3.10)

The electrochemical reduction of Hb results in the formation of Fe(II) from Fe(III) (Eq. (3.6)). NO_2^- in the acidic medium (pH 4.0) forms an unstable molecule HNO_2. This molecule reacts with Hb to yield [HbFe(II)NO]$^+$ nitrosyl adduct. Further,

nitroxy adduct decomposes by loss of HNO which ultimately leads to formation of N_2O.

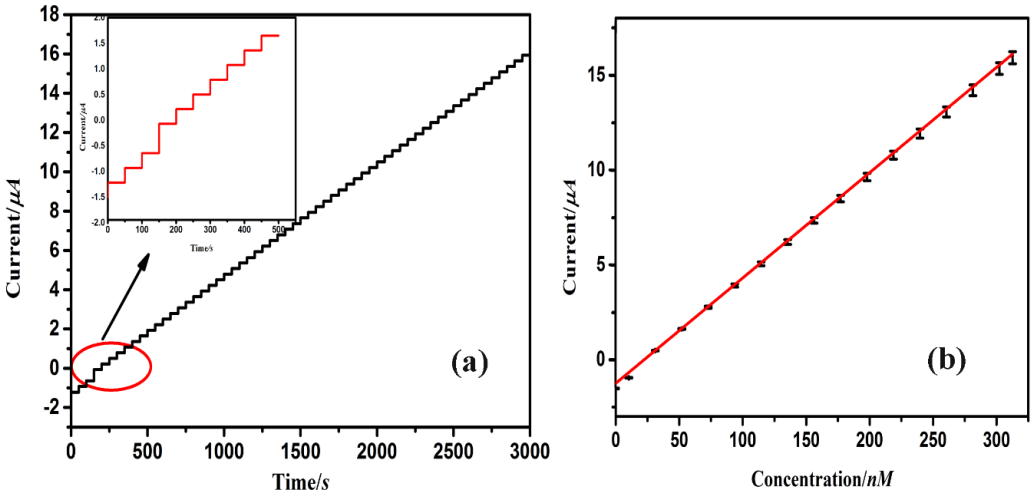

Figure 3.20(a) Amperometric curve obtained using GCE/RGO -NH_3/Hb to successive addition of $NaNO_2$ (5 to 300 nM) in stirred 0.1mol L^{-1} PBS (pH 4.0), at applied potential of −0.67 V with a time interval of 50s; Inset: Magnified portion of amperometry from 0 to 500 s time interval. (b) Calibration curve with respect to peak current (I/μA) vs. nitrite concentration/(nM). Inset: Concentration range from 0 to 100 nM. Error bars represent the standard deviation for three independent measurements.

The performance of the GCE/RGO-NH_3/Hb for the detection of nitrite was also investigated by amperometry. From Figure 3.20 (a), we observed a step like increase in the current response towards nitrite within 5 s demonstrating its rapid response. Moreover, as illustrated in Figure 3.20 (b) the sensor displayed a linear response in the 5 to 300 nM nitrite range with a correlation coefficient of 0.9975, sensitivity of 256 μA/nM cm^2 and detection limit of 1.3 nM (based on a signal-to noise ratio of 3). Performances of various nitrite biosensors reported in literature are listed in Table 3.3.

This superior performance of GCE/RGO-NH_3/Hb can be ascribed to the following reasons. Firstly, RGO-NH_3 with nitrogen moieties could provide a favourable microenvironment for the protein to retain its structure and thereby stability. Furthermore, RGO-NH_3 with a relatively high mobility of charge carriers also emerged as the good interface for efficient electron transfer between the protein and the electrode.

Table 3.1 Comparison of different Hb-based nitrite sensors.

Modified electrode	Surface concentration /(mol cm^{-2})	Limit of detection /(μM)	Linear range/(mM)	[Ref.]
Hb/RTILs/ZrO_2 nanotubes[1]	–	0.2	0.005–0.5	(Ma, Zhan, Ma, Wang, & Li, 2012)
Hb/RTIL/PDDA-GN[2]	4.25×10^{-10}	0.04	0.0002–0.0326	(K. Liu, Zhang, Yang, Wang, & Zhu, 2010)
Cht[3]-Hb-MWCNT-RTILs/CILE	2.87×10^{-9}	100	0.4–8	(Z. Zhu et al., 2010)
Hb–PVA–RTILs/GC [4]	2.2×10^{-10}	–	0.3–11.4	(Yafen Zhang, Yan, Zhao, & Zeng, 2009)
Hb-microbelts modified GCE	8.41×10^{-11}	–	–	(Ding, Wang, Li, & Lei, 2010)
Hb/PI[5]/MWCNTs/GCE	–	0.63	0.03–0.68	(Kou, Jia, Wang, & Ye, 2012)
GCE/RGO -NH_3/Hb[6]	9.26 x 10^{-8}	0.0013	0.000005-0.000300	This work

1 – Zirconium dioxide; 2-graphene nanosheets; 3 – chitosan; 4 - polyvinyl alcohol; 5 – polyimide; 6–Glassy carbon electrode/N-doped reduced graphene oxide/ Hemoglobin.

3.5.7 Selectivity, stability and repeatability

The selectivity of the biosensor was investigated in the presence of interfering species such as (0.5 mM) ascorbic acid (AA), (0.5 mM) uric acid (UA), (0.5 mM) dopamine (DA) and (0.5 mM) H_2O_2 along with $NaNO_2$ (100 nM) solution. The sensor exhibited negligible response towards the interfering species confirming the selectivity of the proposed sensors and is shown in Figure 3.21. Further, no obvious change in the voltammograms is noticed after 50 continuous scans on the GCE/RGO-NH_3/Hb modified electrode confirming the excellent stability of the GCE/RGO-NH_3/Hb modified electrode.

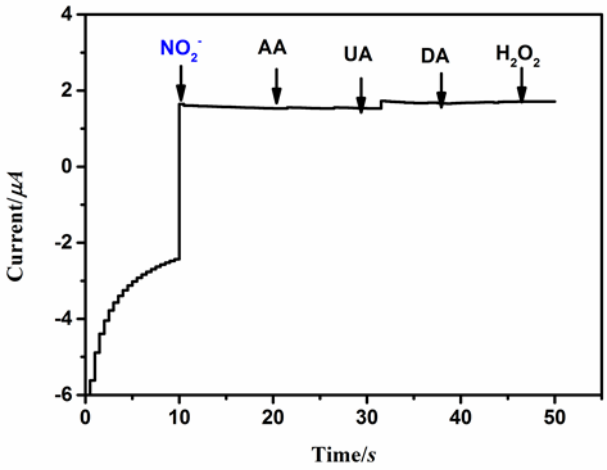

Figure 3.21 Interference study of GCE/RGO-NH_3/Hb in the presence of 100 nM NO_2^-, 0.5 mM of AA, UA, DA and H_2O_2.

Moreover, the long-term stability of the above platform was studied by examining its current response after storage at 4 °C for a month. The modified electrode retained 92.7 % of its initial response towards the detection of 1.0 mM nitrite after a month, demonstrating a good long-term stability (Figure 3.22). The observed behaviour can be attributed to the excellent biocompatibility of RGO-NH_3, that provided a favourable environment for Hb to retain its bioactivity. Moreover, the electrodes exhibited an excellent repeatability with a R.S.D of 2.5% (N=5 electrodes) when the electrodes were employed for the detection 10 mM nitrite.

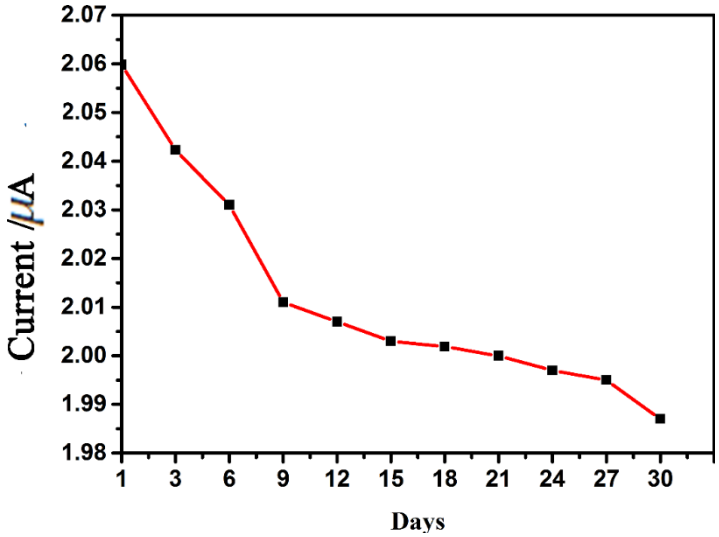

Figure 3.22 Plot showing the stability tests of GCE/RGO-NH_3/Hb in 0.1 M PBS pH 4.0 containing 1 mM $NaNO_2$. Current decay recorded every three days consecutively for 30 days.

3.6 Conclusion

In summary, this chapter discusses the simple method for synthesis of RGO *via* the chemical reduction-based process using hydroiodic acid with acetic acid as reducing agent at low temperature presented. Further, RGO was successfully functionalized by O_2, N_2 and NH_3 RF plasma. The effect of functionalization on crystallinity and morphology investigated by XRD and TEM, indicates that there is no distortion in the graphitic structure of RGO after plasma treatment, while FTIR, XPS and Raman spectroscopy analysis confirmed the effective functionalization. The excellent conductivity together with large surface area of RGO-NH_3 provided a suitable platform for the immobilization of Hb. RGO-NH_3 significantly promoted the direct electron transfer between Hb and the underlying electrode with enhanced electron transfer. Furthermore, the fabricated mediator-free biosensor was applied for detection of nitrite with a limit of detection of about 1.3 nM (S/N=3), as well as prolonged stabilization and repeatability. This suggests that the RGO -NH_3 modified electrode appears to be a potential candidate for the biosensing applications.

CHAPTER 4

GS/GNR hybrid graphene: Synthesis, functionalization, characterization and application in electrochemical biosensor

This Chapter deals with the hybridization of graphene, functionalizing the hybridized material with nitrogen heteroatom by plasma functionalization and incorporating nickel nanoparticle by chemical reduction method. Detailed characterization studies were carried out to understand the structure and morphology of all the three materials. The electrochemical behaviour of hybrid graphene, nitrogen functionalized hybrid graphene and nickel incorporated hybrid graphene were monitored with the selective interaction of AA, simultaneous detection of AA, DA UA and detection of glucose, respectively. Finally, a comprehensive analytical result for the sensing platform is presented.

4.1 Introduction

The limitations of RGO can be overcome by another promising approach i.e hybridization, wherein RGO acts as a 2D planar substrate for anchoring other nanomaterials like carbon-based nanostructured materials CNT, GOS, GNR and fullerene, and metals/metal oxides nanomaterials (Yen et al., 2011) (Chao Xu, Wang, & Zhu, 2008). The nanomaterials incorporated in between the 2D platform acts as a spacer material, thereby prevents the face to face stacking, increases its specific surface area and exhibits synergetic properties of GS and spacer material by providing increased electrical conductivity which enhances the ion diffusion (H. Wang, Kakade, Tamaki, & Yamaguchi, 2014). In the past few years, there has been considerable interest in preventing the GS aggregation by including the carbon spacers, such as functionalized carbon nanotubes (f-CNT) or carbon black (CB) or carbon nanofibers (CNF). Because of unique properties like enhanced surface area and increased electrical conductivity, these hybrid material serves as a novel electrode in various applications including sensors and energy storage.

The electrocatalytic performance of GS/GNR may be further improved by functionalization i.e either by plasma functionalization with heteroatoms such as nitrogen or by incorporating metal nanoparticles *via* chemical method (A. Kumar et al., 2013), (Ensafi, Ahmadi, & Rezaei, 2017). The functionalization of nitrogen alters the electronic properties and surface chemistry of GS, thereby further

enhances the electrocatalytic activity of carbon materials. Many research works, for instance, nitrogen-doped graphene (Sheng et al., 2012), mesoporous nitrogen-rich carbonaceous material (Sheng et al., 2012), nitrogen-doped carbon nanofibres (J. Sun et al., 2015), are reported as suitable material for fabricating electrochemical biosensor.

Incorporation of metal nanoparticles is also an approach to enhance the electrocatalytic performance of the hybrid material. In spite of various catalytic materials, like metal, metal oxide and alloys, such as Pt, Au, Ag, Cu, Ni, Co, NiO, $NiCo_2O_4$, $NiCoO_2$, Co_3O_4 (Xinran Wang, Tabakman, & Dai, 2008), nickel (Ni) based nanomaterials (X. Xiao et al., 2012) with wide linear range and excellent catalytic activity have captured more attention towards researchers, in the field of electrochemical biosensors (Fleischmann, Korinek, & Pletcher, 1971). Despite their high electrocatalytic activity, the long-term stability of the Ni nanoparticles gets reduced by its surface fouling effect. Hence, the need for a conductive nanostructured substrate arises which can enhance the electrode stability and electron transfer toward oxidation of analyte. Therefore, due to the increased specific surface area, good electrical conductivity, fast electron transfer and high loading capacity, the carbon-based hybrid material has drawn much attention as an excellent catalyst support material (Ensafi et al., 2017).

4.2 Experimental

4.2.1 Synthesis of GS/GNR hybrid material

As displayed in Figure 4.1 GOS and GOR, taken in the ratio 10:1 was co-reduced with 15 mL $(NH_2)_2.H_2O$ by stirring for 24 h at 40°C. The product was rinsed with distilled water, ethanol and acetone. To increase the rate of deoxygenation, leading to better conductivity, the product was stirred with 15 mL of HI for 24 h at 40°C. Finally, the filtered product with distilled water, ethanol and acetone was vacuum dried at room temperature for 24 h to obtain GS/GNR hybrid material.

The reaction mechanism of formation of GS/GNR hybrid by co-reducing GOS and GOR is depicted in Figure 4.2.

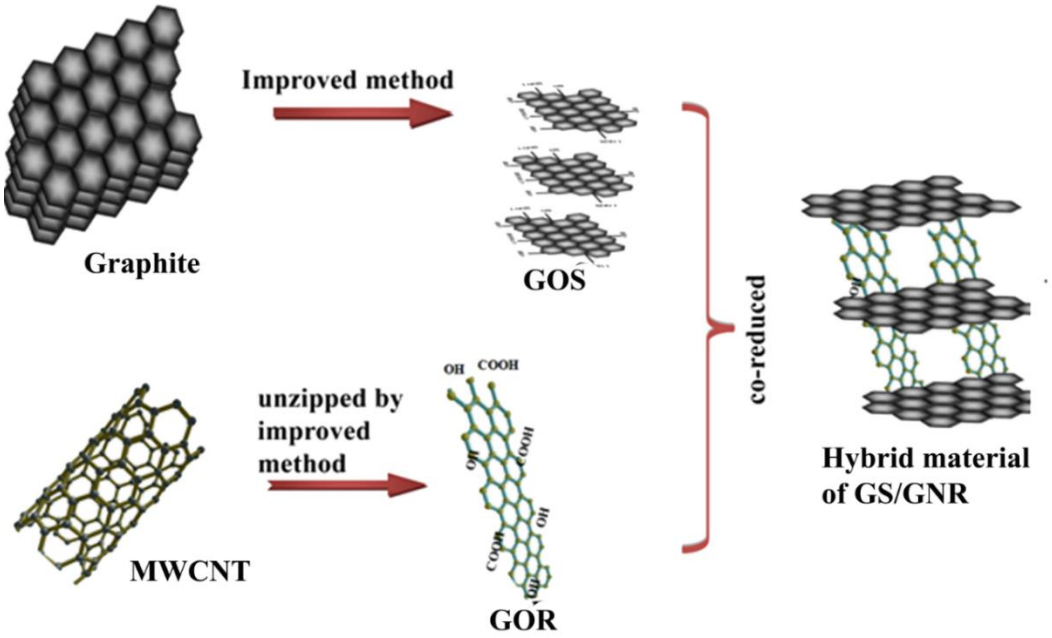

Figure 4.1 Schematic diagram representing the synthesis of hybrid graphene

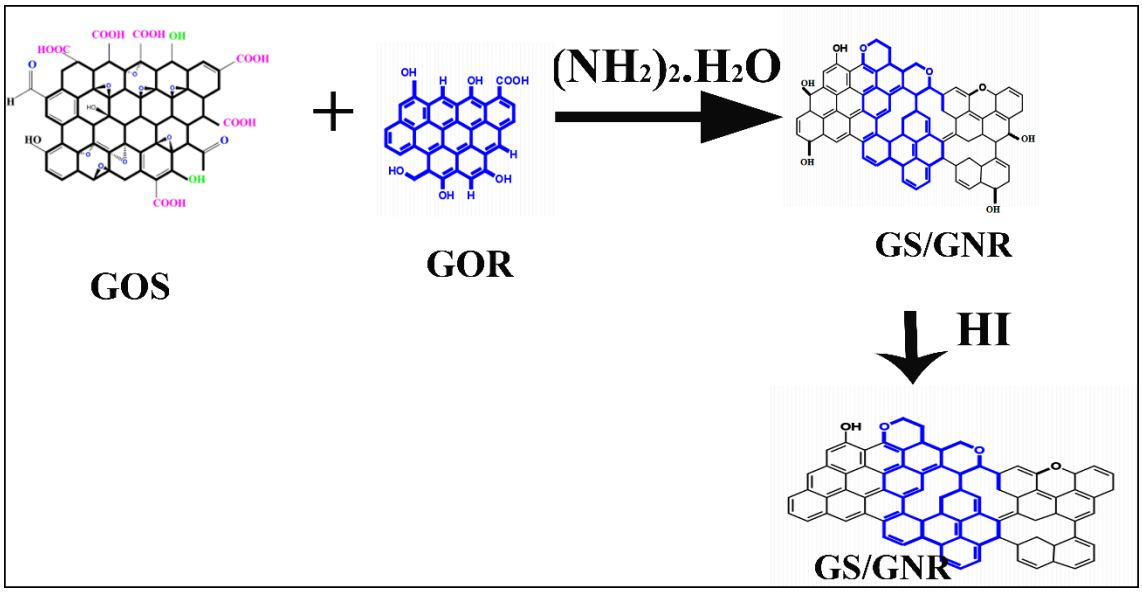

Figure 4.2 Reaction mechanism of preparation of hybrid graphene.

4.2.2 Plasma functionalization of GS/GNR

The functionalization of GS/GNR illustrated in Figure 4.3 *via* N_2/Ar RF plasma is as follows. Initially, the sample was loaded on the substrate holder and the system was evacuated to a pressure of 0.1 Pa. After achieving the base vacuum, N_2 and Ar gases were introduced through a mass flow controller at a desired flow rate of 10 sccm each. Once the desired pressure was stabilized at 50 mTorr, plasma was generated between the two electrodes at a fixed power of 100 W for a preset time of 10 min.

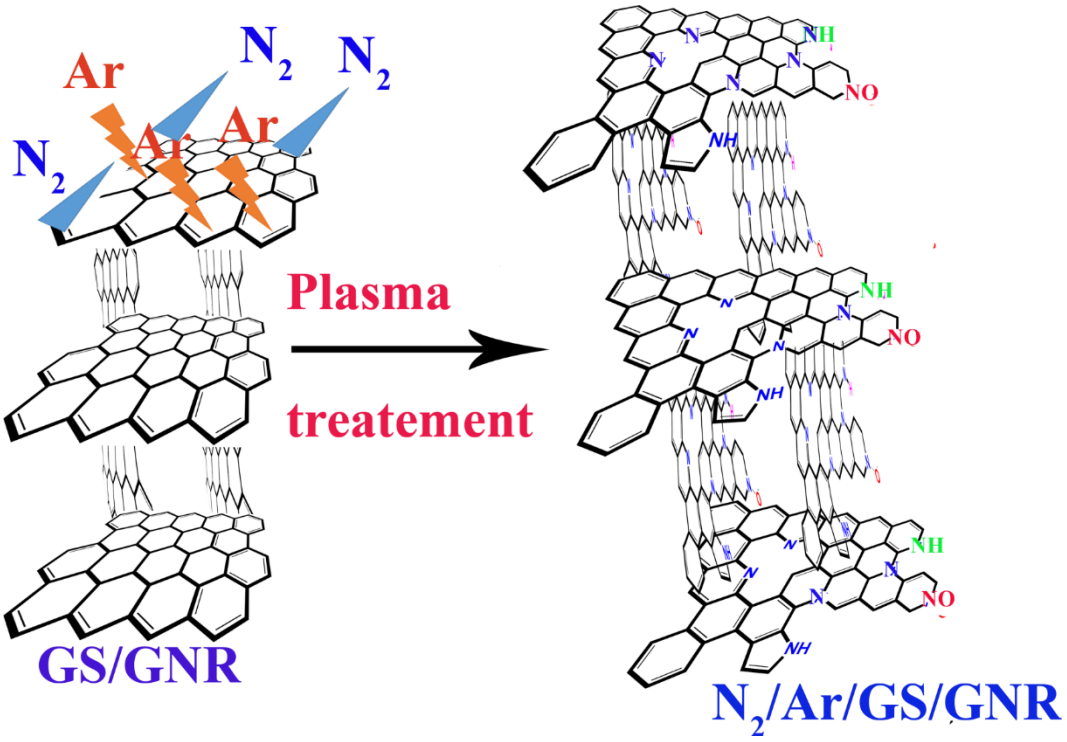

Figure 4.3 Schematic representation of functionalization of GS/GNR *via* N_2/Ar RF plasma.

4.2.3 Synthesis of Ni/GS/GNR hybrid material and Ni nanoparticles

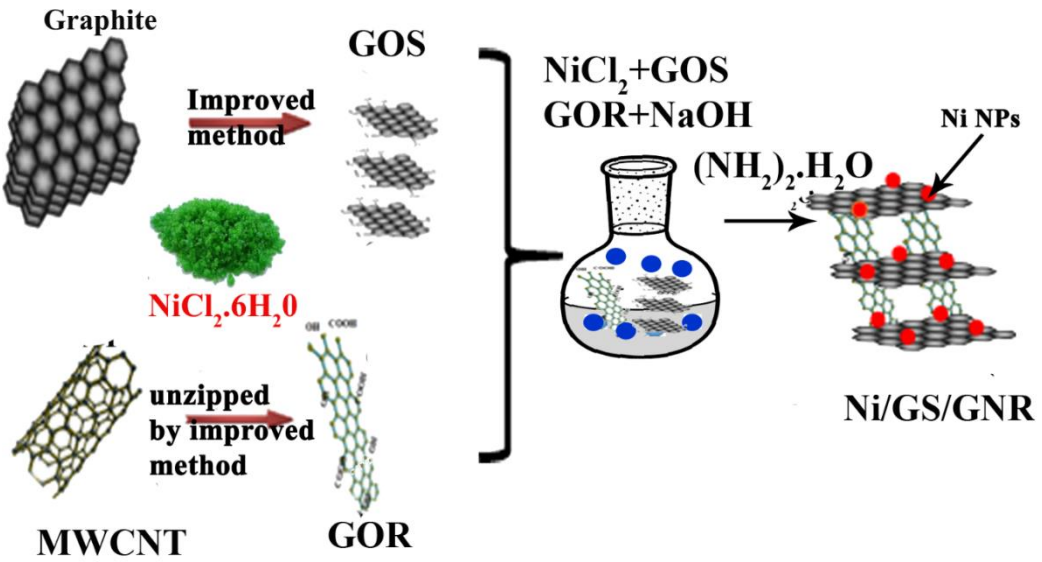

Figure 4.4 Synthesis of Ni/GS/GNR

Ni/GS/GNR was prepared by *in-situ* chemical reduction method as follows: GOS and GOR suspension (1.0 mg mL^{-1}) were mixed at the ratio of 1:1 and ultrasonically dispersed for 1 h in distilled water. Then, 0.020 g of PVP dissolved in 15 mL ethanol and 60 mL water at room temperature was added with

0.1 M NaOH solution and 0.05 M $NiCl_2.6H_2O$. After sonicating for 1 h, the solution was reduced by 2 mL of $(NH_2)_2$. H_2O at 100 ºC for 12 h. Later after washing with ethanol and water for several times, the product was dried under vacuum at 60ºC for 12 h to obtain Ni/GS/GNR.

Ni nanoparticles were synthesized using $NiCl_2.6H_2O$ as a precursor *via* chemical reduction method. First, the mixture was dissolved in 0.020 g of PVP in 15 mL ethanol and 60 mL water, followed by addition of 0.1 M NaOH solution and 0.05 M $NiCl_2.6H_2O$ the mixture was reduced by 2 mL of $(NH_2)_2$. H_2O after sonicating for 1 h. Later, after washing with ethanol and distilled water for several times, the product was dried under vacuum at 60ºC for 12 h to obtain Ni nanoparticles.

As depicted in Figure 4.4 the preparation of Ni/GS/GNR hybrid material *via* chemical reduction method involves three stages. Firstly, Ni^{2+} were adsorbed to the GOS and GOR surface through electrostatic interaction of functional groups (carboxyl, hydroxyl and epoxy groups) on GOS and GOR surface. Then, after adding NaOH, Ni^{2+} in GOS and GOR mixture gets converted to Ni $(OH)_2$. Finally, the mixture was co-reduced by hydrazine hydrate. During this process, the reducing agent plays its role in reduction of GOS and GOR into GS/GNR hybrid and Ni^{2+} ions to Ni^0 nanoparticles, as well as in the growth of Ni nanoparticles into GS/GNR network. Finally, incorporated Ni nanoparticles into hybrid graphene leads to form a complex network where the GNR and GS are intermeshed together with randomly interspersed Ni nanoparticles.

4.3 Characterization

4.3.4 Morphological studies

The obtained SEM images illustrated in Figure 4.5 (a) and (b) investigate the morphology of GOR and GS/GNR. The ribbon-shaped structure observed in the image Figure 4.5 (a) indicates the completely unzipped CNT. During the co-reduction of GOS and GOR, the oxygen moieties present on the edge and basal planes of both GOS and GOR interact and get reduced with the formation of wrinkled morphology of the sheets along with GNR on the basal and edges of GS as reflected in Figure 4.5 (b) evidences the successful formation GS/GNR hybrid material through the incorporation of GNR on GS.

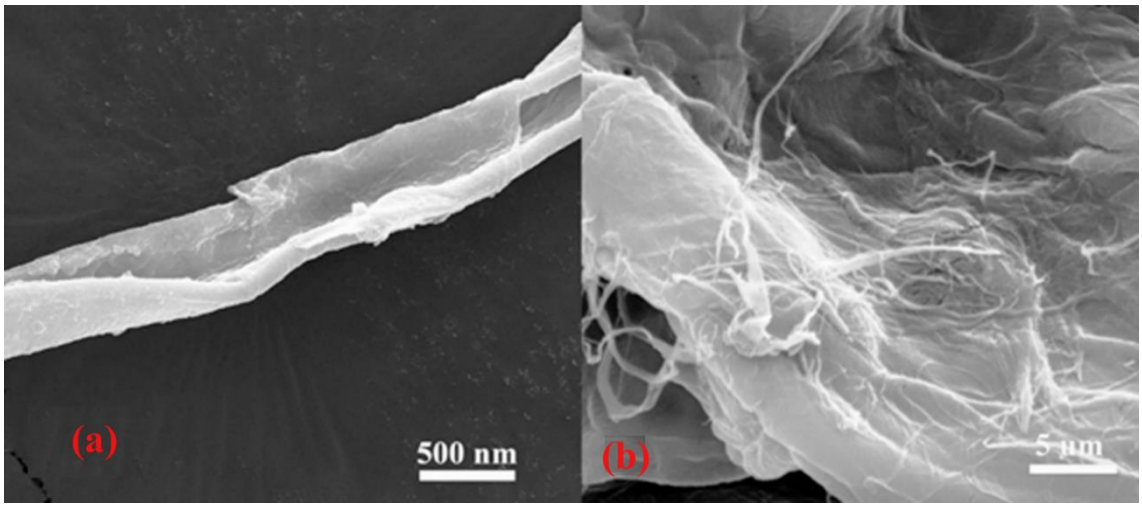

Figure 4.5 SEM image of (a) GOR and (b) GS/GNR

During the reduction process the incorporated GNR acts as carbon spacer between the GS, prevents the agglomeration of GS with an increase in surface area and pore size. As a result of incorporation of ribbons into sheets, the specific surface area of GS/GNR (82.7 m^2/g) is increased by a factor of four compared to RGO (20.7 m^2/g).

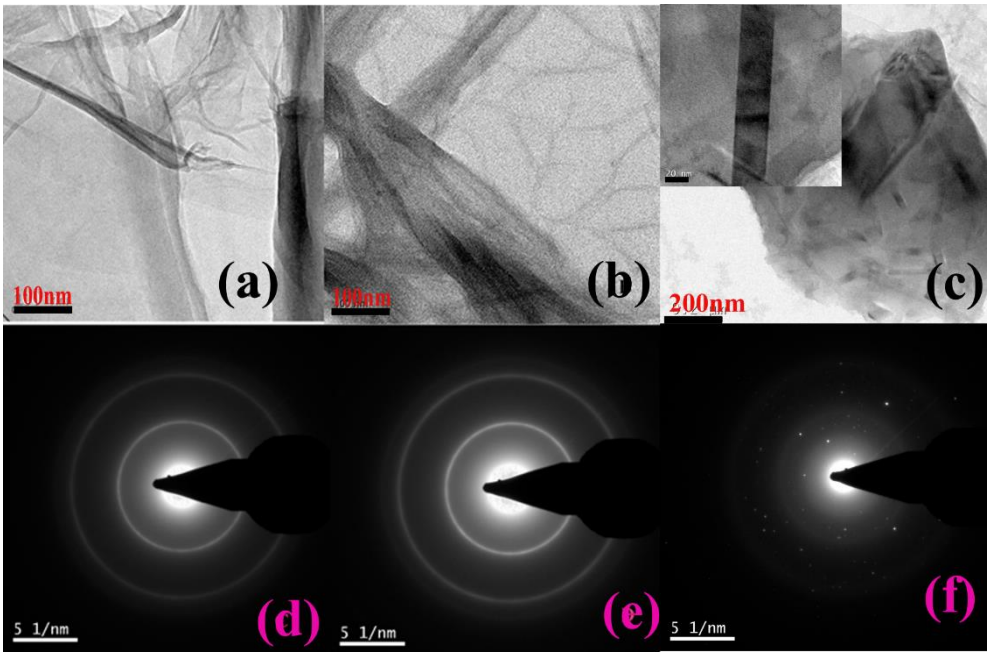

Figure 4.6 TEM image of (a) GOS (b) GOR and (c) GS/GNR with respective SAED pattern d, e and f

The HRTEM image demonstrated in Figure 4.6 depicts the morphology of GOS, GOR and GS/GNR. Figure 4.6 evidences the morphology of GOS with a thin crumpled cloth like structure with folded edges. Wavy structured strip, with an

increase in the width to 60 nm, depicted in Figure 4.6 (b), showed the completely unzipped CNT. Typical width of GOR lies in the range of 50-100 nm range. Well-dispersed GNR in GS as depicted in Figure 4.6 (c) evidences the quasi-1D GNR incorporated to 2D GS. The enlarged area containing GS and GR are shown in the inset image of Figure 4.6 (c).

Moreover, the ring pattern observed in the SAED depicted in Figure 4.6 (d and e) indicates the polycrystalline character of both the samples (GOS (d) and GOR (e)) (Wilson et al., 2009). Randomly arranged bright spots are corresponding to the crystalline character of randomly overlapped GS and GNR in the GS/GNR hybrid (Figure 4.6 (f)).

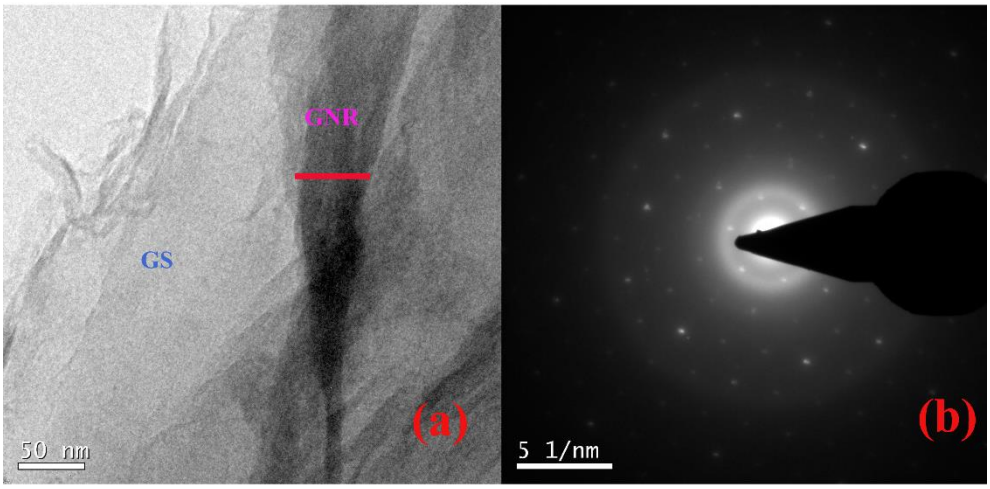

Figure 4.7 TEM images of (a) N_2/Ar/GS/GNR and (b) SAED pattern.

Typical morphology of N_2/Ar/GS/GNR with the corresponding SAED pattern depicted in Figure 4.7 (a) & (b) respectively demonstrates the random distribution of GNR with GS and graphite AB stacking order. The clear diffraction spots with six-fold symmetry observed strongly evidences the prevention of graphite AB stacking in lattice even after plasma functionalization (Sheng et al., 2011).

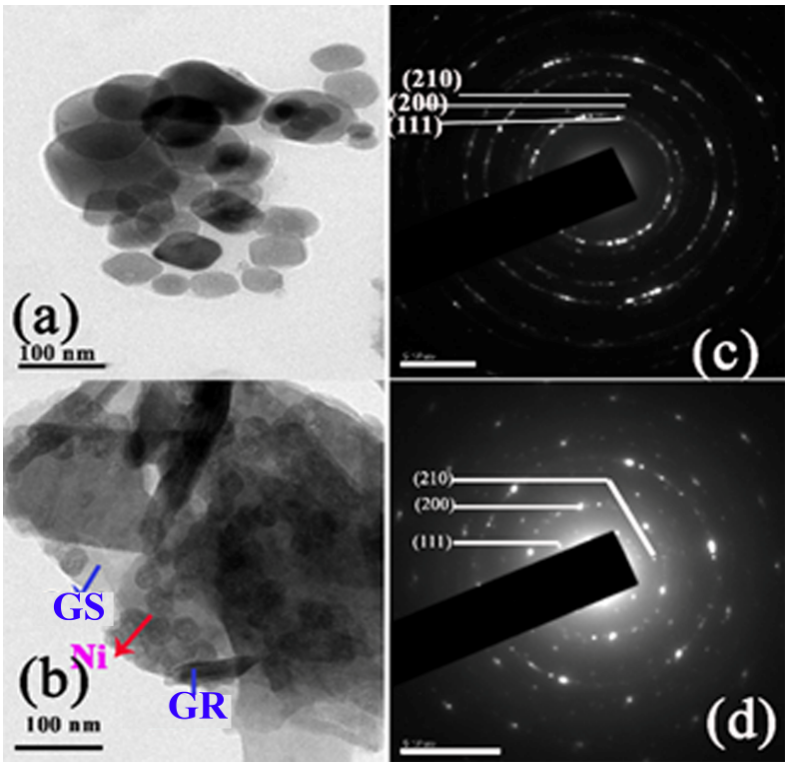

Figure 4.8 TEM image of (a) Ni (b) Ni/GS/GNR (c) selected area energy diffraction (SAED) pattern of Ni and (d) Ni/GS/GNR.

As depicted in Figure 4.8(a), the nanostructure of Ni nanoparticles exhibits dispersed sphere like morphology with an average size of 55 ± 2 nm. The morphology of Ni/GS/GNR hybrid, displayed in Figure 4.8(b) describes the Ni nanoparticles coexists along with GS/GNR. The SAED pattern depicted in Figure 4.8 (c and d) describes the diffraction data of both Ni and Ni/GS/GNR. The lattice spacing of 0.24 nm and 0.21 nm which could be readily indexed to the (111) and (200) crystal planes respectively confirm the crystalline structure of Ni nanoparticles. The bright spots in hexagonal pattern attributed to sp^2 -bonded carbon frameworks, along with diffraction spots at (111), (200) and (210) planes assigned to cubic Ni in Ni/GS/GNR hybrid are in good agreement with XRD results shown in Figure 4.9.

4.3.2 XRD

The crystalline phases of GOS, GOR and GS/GNR displayed in Figure 4.9 was examined with X-ray diffraction technique. The exfoliation of graphite *via* oxidation was evidenced by the diffraction peak around 10° at (001) plane as illustrated in Figure 4.9 (a) (Marcano et al., 2010). The intense peak observed

around 8° as shown in Figure 4.9 (b) indicates the exfoliation of CNT through unzipping (Higginbotham et al., 2010).

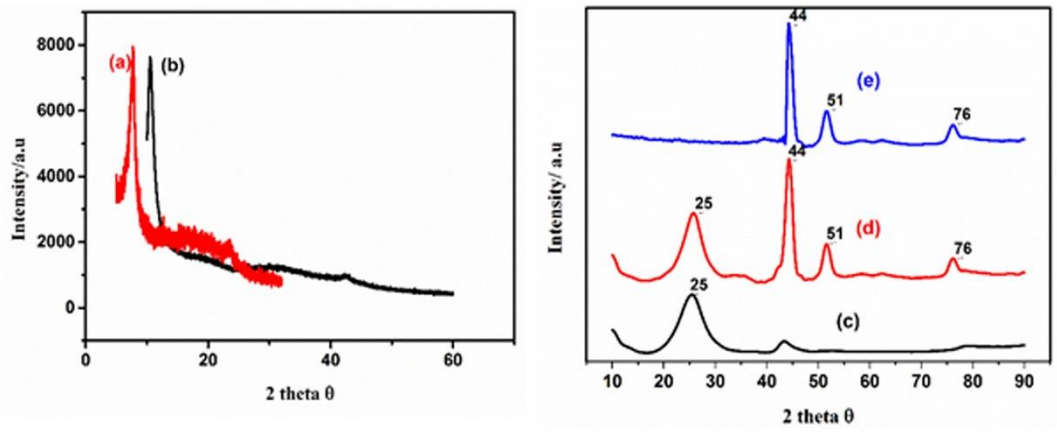

Figure 4.9 XRD pattern of (a) GOS, (b) GOR, (c) GS/GNR, (d) Ni/GS/GNR and (e) Ni nanoparticles.

XRD pattern of GS/GNR displayed in Figure 4.9 (c), demonstrates the co-reduced GOR and GOS mixture with the appearance of graphitic peak at 25.2° at (002) (Guo, Wang, Qian, Wang, & Xia, 2009). The Ni nanoparticles incorporated with GS/GNR in Ni/GS/GNR hybrid material was evidenced by the diffraction peaks at 2θ = 25.2°, 44.7°, 52° and 76.5° in Figure 4.9 (d), corresponding to GS/GNR and Ni with a FCC lattice (1 1 1), (2 0 0) and (2 2 0) planes, respectively. Moreover, the diffraction peak of Ni displayed in Figure 4.9 (e) was found around 44.7°, 52° and 76.5° corresponding to the characteristic peaks of Ni (JCPDS card No. 04-0805), with a FCC lattice, which belong to (1 1 1), (2 0 0) and (2 2 0) planes, respectively.

4.3.3 Surface chemistry

The chemical moieties on the surface of GOS, GOR and GS/GNR are qualitatively analysed by FTIR, and their respective spectra are illustrated in Figure 4.10. The sp^2 character of carbon was observed at 1570-1620 cm^{-1} in all the three cases (Figure 4.10 (a, b, c)). Epoxy and hydroxyl groups were observed at 1217 and ~3200 cm^{-1} in GOS and GOR (Figure 4.10 (a) and (c)). The disappearance of carbonyl groups peak at 1720 and 1717 cm^{-1} at GS/GNR evidences the co-reduction of GOS and GOR.

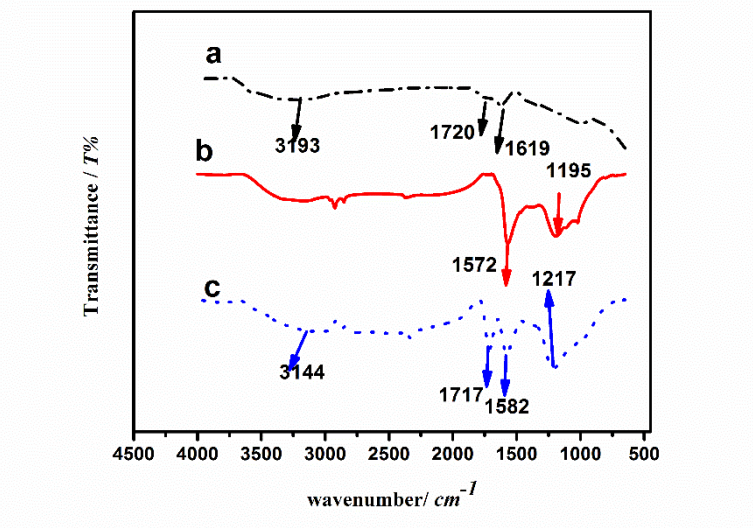

Figure 4.10 FTIR spectra of (a) GOS, (b) GS/GNR, and (c) GOR

4.3.5 Raman Spectroscopy

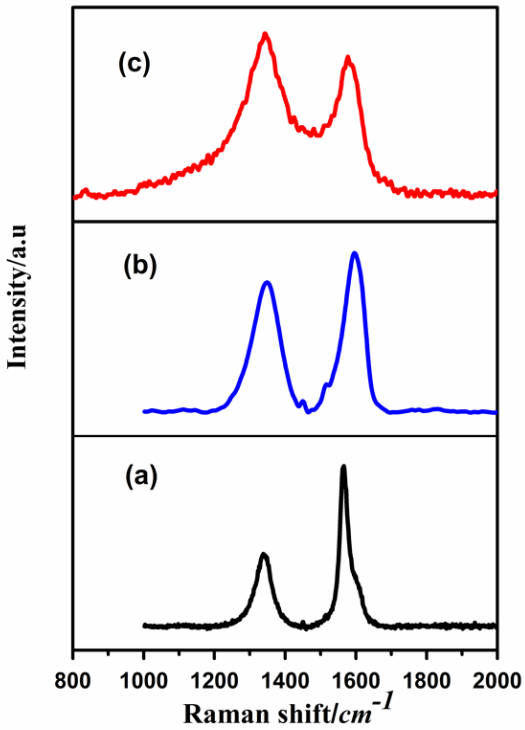

Figure 4.11 Raman spectra of (a) GS/GNR (b) N_2/Ar/GS/GNR and (c) Ni/GS/GNR

Raman spectroscopy investigates the effect of the functionalization of N_2/Ar and Ni nanoparticles on the structure of GS/GNR. The Raman spectra illustrated in Figure 4.11, exhibit two characteristic peaks at 1352 and 1581 cm^{-1} corresponding to D and G band (Ni, Wang, Yu, & Shen, 2010). The

intensity ratio between D and G band was effectively used to evaluate the degree of disorder in GS/GNR, N_2/Ar/GS/GNR and Ni/GS/GNR. The enhancement in I_D/I_G ratio from GS/GNR: 0.5 to N_2/Ar/GS/GNR: 1.08 and Ni/GS/GNR 1.16, reveals the increased disorder and defect density generated by the sp^2 transformed to sp^3configuration during functionalization.

4.3.6 XPS

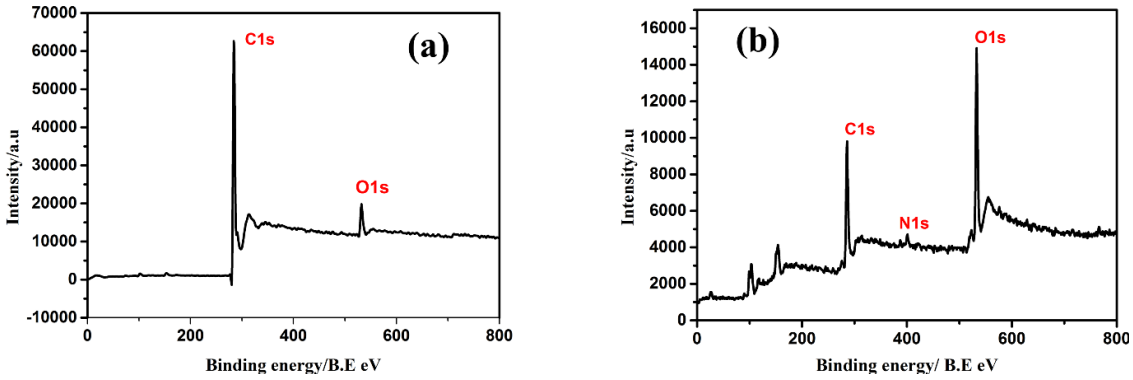

Figure 4.12 Survey spectrum of (a) GS/GNR and (b) N_2/Ar/GS/GNR

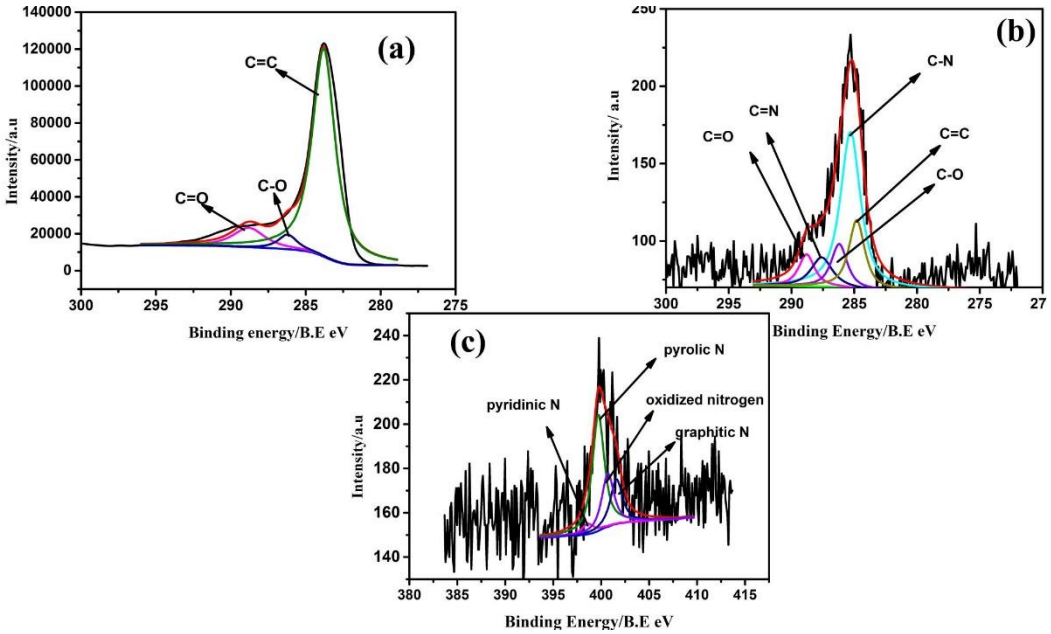

Figure 4.13 XPS high resolution spectrums C1s of (a) GS/GNR (b) N_2/Ar/GS/GNR and (c) N1s of N_2/Ar/GS/GNR.

The detailed quantitative and qualitative analysis of chemical moieties introduced during plasma functionalization was investigated by XPS. The survey spectrum of N_2/Ar/GS/GNR illustrated in Figure 4.12 confirms, the C, O and N containing functional groups are attached to the carbon scaffold with the respective C1s, N1s and O1s peaks appearing at about 284.5 eV, 400 eV, and 533 eV. Figure 4.13 (a)

and (b) illustrate the de-convoluted C1s high-resolution spectra of GS/GNR and N_2/Ar/GS/GNR, respectively. The deconvoluted high-resolution C1s peak exhibits five peaks. The peak at 284.8 eV was ascribed to the sp^2 carbon atoms constituting graphitic regions. The other four weak peaks centred at 285.3, 286.2, 287.6 and 288.8 eV correspond to (C=N), (C-N/C-O), (C=O) and (O-C=O), respectively (Lee, Lee, Chang, & Hu, 2011) and the actual concentration of the same are depicted in Table 4.1.

High-resolution N 1s peak demonstrated in Figure 4.13 (c) was deconvoluted into four peaks centered at 398.5 ± 0.2 eV, 399.8 ± 0.1 eV, 400.7 ± 0.5 eV and 401.6 ± 0.5 eV corresponding to pyridinic, pyrrolic and graphitic nitrogen and oxidized nitrogen (Hulicova, Kodama, & Hatori, 2006). The respective concentrations of the functional moieties are given in Table 4.2.

Table 4.1 Elemental data and C1s, peak analysis of GS/GNR and N_2/Ar/GS/GNR.

Sample	Elemental analysis at %			C1s composition%				
	C	O	N	C=C (284.8eV)	C-O (286.2eV)	C=O (288.5 eV)	C=N (287.6eV)	C-N (285.3eV)
GS/GNR	82.5	17.5	0	82.3	9.01	8.59	Nil	Nil
N_2/Ar/GS/GNR	65.9	30.0	4.1	18.03	11.38	8.38	10.22	51.99

Table 4.2. N1s XPS peak analysis of GS/GNR and N_2/Ar/GS/GNR.

Sample	N1s composition%			
	Pyridine (398.6 eV)	Graphitic N (400.7 eV)	Pyrrolic N (399.7eV)	Oxidized nitrogen (401.6eV)
GS/GNR	-	-	-	-
N_2/Ar/GS/GNR	24.9	25.03	24.97	25.09

4.4 Application of hybrid graphene and modified hybrid graphene materials material in sensing various electrochemically active analytes.

This section investigates the application of GS/GNR, N_2/Ar/GS/GNR and Ni/GS/GNR in detecting various biological analytes by electrochemical method. The sensing mechanism of the respective materials are illustrated in Figure 4.14.

As a first step, the electrocatalytic activity of GS/GNR was studied towards the oxidation of AA, a most common electroactive biological compound found in fresh fruits, vegetables, seeds and nuts. Next the N_2/Ar RF plasma functionalized GS/GNR was applied to simultaneously detect AA, DA and UA. Finally, Ni incorporated GS/GNR was employed to investigate the sensing of glucose.

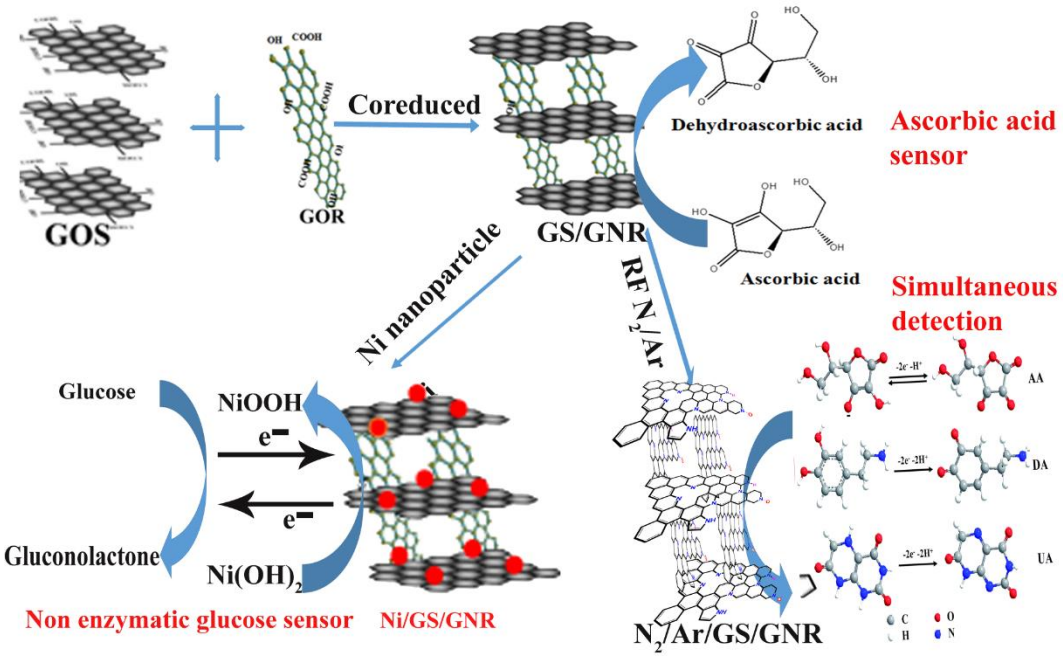

Figure 4.14 Schematic illustration of various biological analytes sensing mechanism on the surface of GCE/GS/GNR, GCE/N_2/Ar/GS/GNR and GCE/GS/GNR/Ni.

AA plays a role in antioxidant, cancer prevention, free radical scavenger and effective antiviral agent (Arrigoni & De Tullio, 2002). Detection of AA is important, particularly in the pharmaceutical and food industries by an inexpensive and easy method. Among the various methods such as available turbidimetry (Farajzadeh & Nagizadeh, 2002), spectrophotometry (Toral et al., 2001) and potentiometry (Abdullin, Turova, Ziyatdinova, & Budnikov, 2002) AA could be effectively detected by electrochemical method (Keeley et al., 2010) with good sensitivity and selectivity.

In this electrochemical process, GS/GNR hybrid material acts as a working electrode for sensing AA. Here, the adsorbed AA molecules on the electroactive sites available on the surface of GCE/GS/GNR get oxidized to dehydroascorbic acid

with the release of two protons and two electrons (F. Li, Li, Feng, Yang, & Du, 2011) as depicted in Figure 4.14 (a).

4.4.1 Electrochemical surface area determination

Before applying the GCE/GS/GNR electrode, its electrochemical surface area (ECSA) was estimated by recording CV at different scan rates using 4 mM $Fe(CN)_6^{3-}$ in 0.1 M KCL electrolyte (Figure 4.15 (a)).

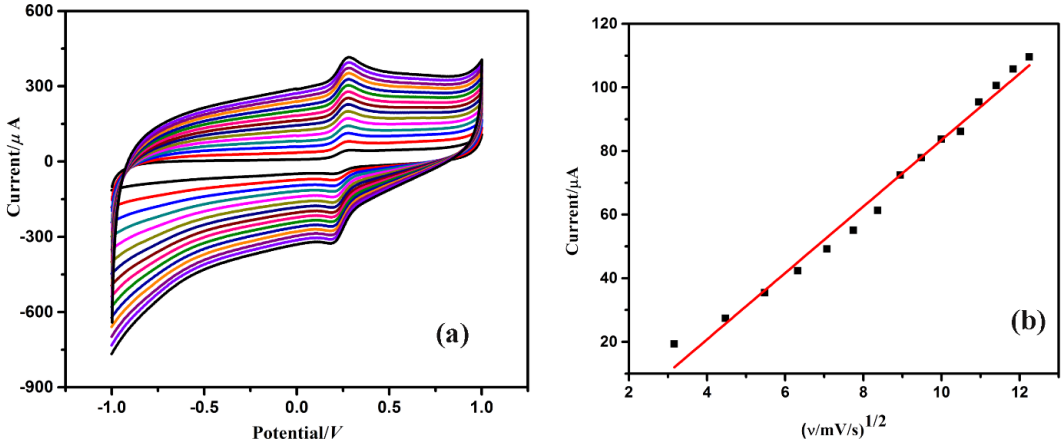

Figure 4.15 (a) CV recorded at various scan rate (10-200 mV/s) in 5mM $Fe(CN)_6^{3-}$ with 0.1 M KCL (b) (I_p) vs $v^{1/2}$.

By using the Randles servick equation (4.1)

$$A = \frac{k}{(2.69 * 10^5)n^{3/2}D^{1/2}C} - - - - \rightarrow (4.1)$$

where *n* is the number of transferred electrons for the redox reaction, *D* is the diffusion coefficient (6.70×10^{-6} cm^2 s^{-1}), *C* is the molar concentration of ferricyanide (4 mM), *A* is the electrochemical surface area (cm^2) and k is the slope value obtained from the plot between peak current (I_p) and square root of scan rate $v^{1/2}$ (Figure 4.15 (b)). The ECSA of GS/GNR was calculated to be 0.365 cm^2.

4.4.2 Optimization of pH

The effect of pH on the modified electrode in 0.1 M PBS containing 5 mM AA with different pH values in the range of 4 to 9, was investigated by CV. The I_p increased with pH from 4.0 and reached a maximum at pH 7.0. As shown in Figure 4.16 peak current value decreased with further increase in pH of the solution. Therefore, the further electrochemical analysis was performed at pH 7.

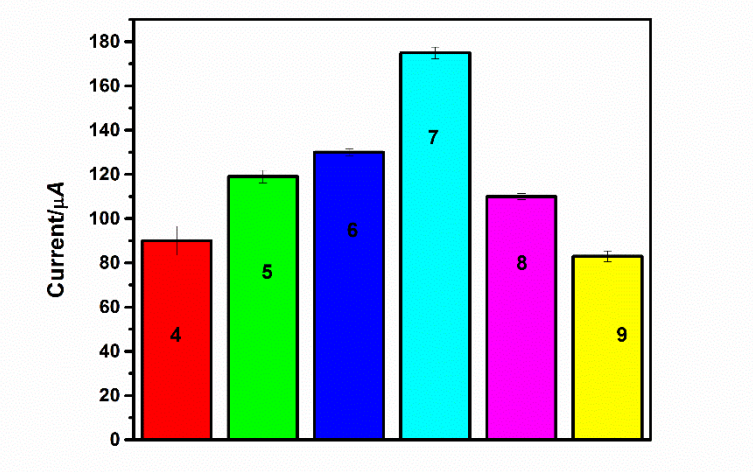

Figure 4.16 Effects of the pH on the oxidation current.

4.4.2 Electrochemical Characterization of AA sensor

Figure 4.17 illustrates the CV response, in presence of 5 mM AA, of the electrodes such as bare GCE, GCE/RGO, GCE/GS/CNT and GCE/GS/GNR in PBS buffer (pH=7) at a scan rate of 100 mV/s. Both GCE and modified GCE exhibited electrocatalytic oxidation response towards AA.

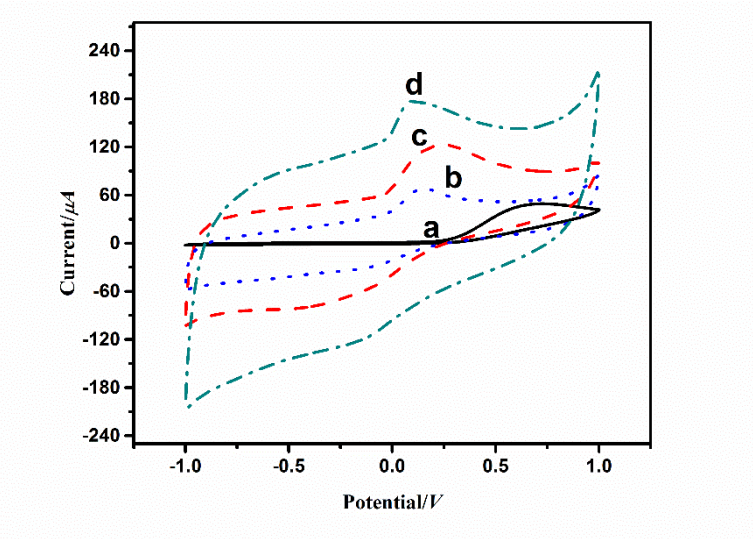

Figure 4.17 CV of (a) GCE, (b) GCE/RGO, (c) GS/CNT/GCE and (d) GCE/GS/GNR electrodes, recorded in the presence of 5 mM AA in PBS (pH 7) at scan rate of 100 mV/s.

In the cases of GCE, GCE/RGO and GCE/GS/CNT, oxidation of AA resulted in a broad peak with the peak potential of 0.666 V (Figure 4.17a), 0.222 V (Figure 4.17b) and 0.150 V (Figure 4.17c), while GCE/GS/GNR exhibited a low oxidation peak potential at 0.080 V with a pronounced current signal (176 μA) (Figure 4.17d). The substantial negative shift with an onset potential at ca. -0.03 V and larger

current signal demonstrated the strong electrocatalytic activity of the GCE/GS/GNR. Herein, the GS/GNR with the large electroactive surface area and excellent electric conducting ability contributes to the decreased oxidation potential of AA.

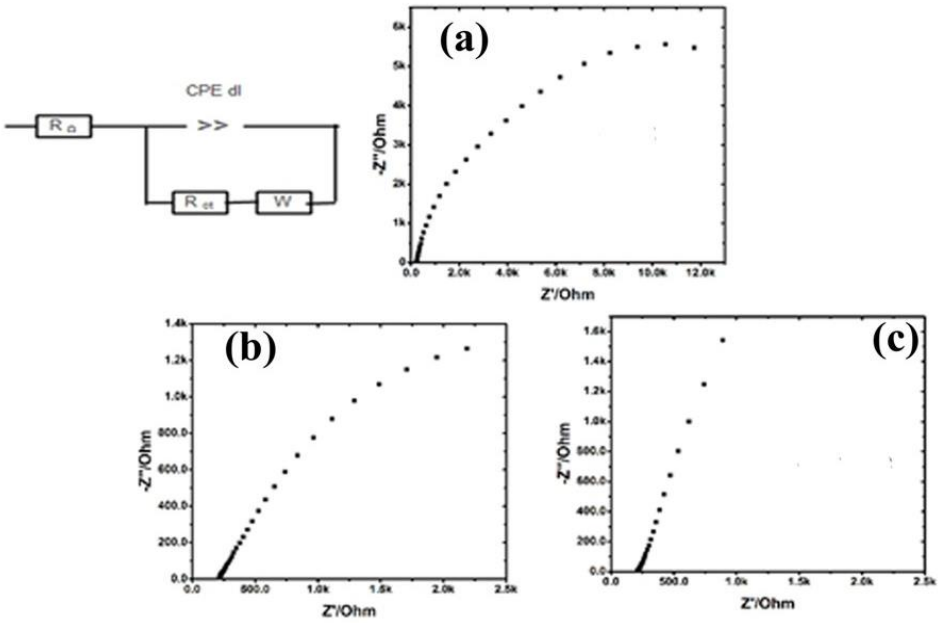

Figure 4.18 EIS of (a) GCE, (b) GCE/RGO and (c) GCE/GS/GNR in 5mM AA.

EIS was further executed to make a comparison of electron transfer of GCE, GCE/RGO and GCE/GS/GNR in an electrolyte of 5 mM AA. The diameter of a semi-circle obtained at higher frequency in the Nyquist plot (Figure 4.18) represents the electron transfer resistance (R_{ct}) while the linear part at lower frequency represents the diffusion limited process. The GCE and GCE/RGO exhibited a semi-circle in the high frequency range with a large electron transfer resistance (R_{ct}) of 15700 Ω and 14500 Ω respectively (Figure 4.18 (a) and (b)), suggesting a relatively sluggish electrochemical performance of the probe. Whereas GCE/GS/GNR in Figure 4.18 C showed nearly straight line with electron transfer resistance (R_{ct}) of 140 Ω indicating a facile electron transfer from the redox probe towards the electrode surface. This could be attributed to the good electron transfer ability of GS/GNR, which facilitates the electrocatalytic oxidation of AA on electrode surface.

4.4.3 Effect of scan rate

Figure 4.19(a) demonstrates the behaviour of GCE/GS/GNR at different scan rates from 10-100 mV/s in 5 mM AA dissolved in PBS solution at pH=7. Plot of peak current (I_p) against the square root of scan rate ($v^{1/2}$) shown in Figure 4.19(b) exhibiting a linear relationship over the range suggests that the oxidation reaction of AA is diffusion-controlled. From the slope value of the plot (I_p) vs (v) (Figure 4.19(c)), the estimated surface coverage (Γc) of ascorbic acid on the surface of GS/ GCE/GNR to be 2.1192 $\times 10^{-6}$ mol/ cm^2 by using the following equation (4.2).

$$I_p = \frac{n^2F^2vA\Gamma c}{4RT} \longrightarrow (4.2)$$

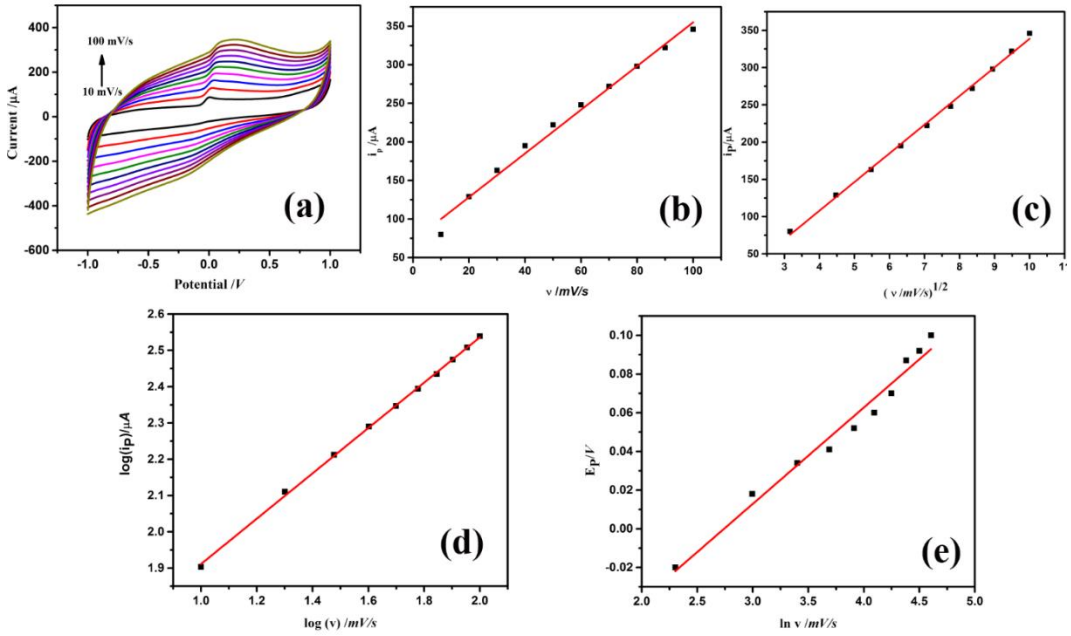

Figure 4.19 (a) CV of GCE/GS/GNR in PBS pH=7 with 5 mM AA at different scan rate (10-100 mV/s), (b) I_p vs $(v)^{1/2}$, (c) I_p vs v, (d) log I_p vs log v and (e) E_{pa} vs ln v

As shown in Figure 4.19(d), the logarithm of peak current (log I_p) versus logarithm of scan rate (log v) shows a linear relationship (log I_p = 0.62log v +1.28; R = 0.992). The obtained slope value (0.62) is slightly higher than the theoretical value of 0.5 for the diffusion-controlled process, but less than 1 which is for the adsorption-controlled electrode process. This confirmed that the electrode process is diffusion controlled.

As shown in Figure 4.19(e), the linear plot between E_p and ln v (E_p = 0.04738 ln v – 0.12394) confirms the irreversible electrochemical process of AA. In addition, the number of electrons transferred in the rate determining step (n) and the electron-transfer coefficient (α) were determined by using the obtained slope in Laviron's equation (Laviron, 1979). (RT/αnF= 0.04738). Therefore, by considering the number of electrons transferred as 2, the electron transfer coefficient would be determined as 0.27 which is closely matching with the theoretical value ranging between 0.3 and 0.7.

4.4.4 Amperometric studies

The potential would be optimized, by varying the potential from 0.05 to 0.09 V and measuring the corresponding amperometric current to AA (shown in Figure 4.20). The response current increased rapidly with the increase of applied potential. When the applied potential was >0.07V, a decrease in current and increase in noise appeared. Therefore, 0.07 V was selected as the optimum applied potential for amperometric detection of AA in the subsequent studies.

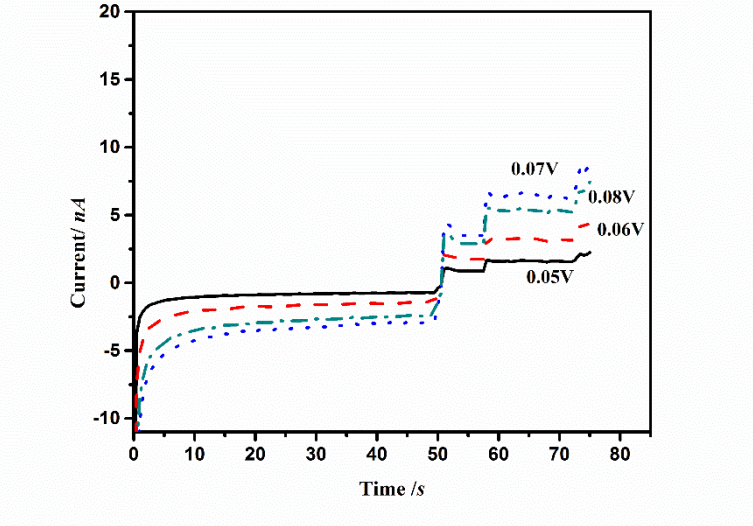

Figure 4.20 Optimization of potential in amperometric studies

The amperometric response of GCE/GS/GNR towards the successive addition of AA could be examined at the potential of 0.07 V in the stirred solution containing PBS at pH 7. Figure 4.21 (a) demonstrates the stepwise increase in current with respect to increase in concentration, with a correlation coefficient of 0.99076, with the signal to noise ratio 3.

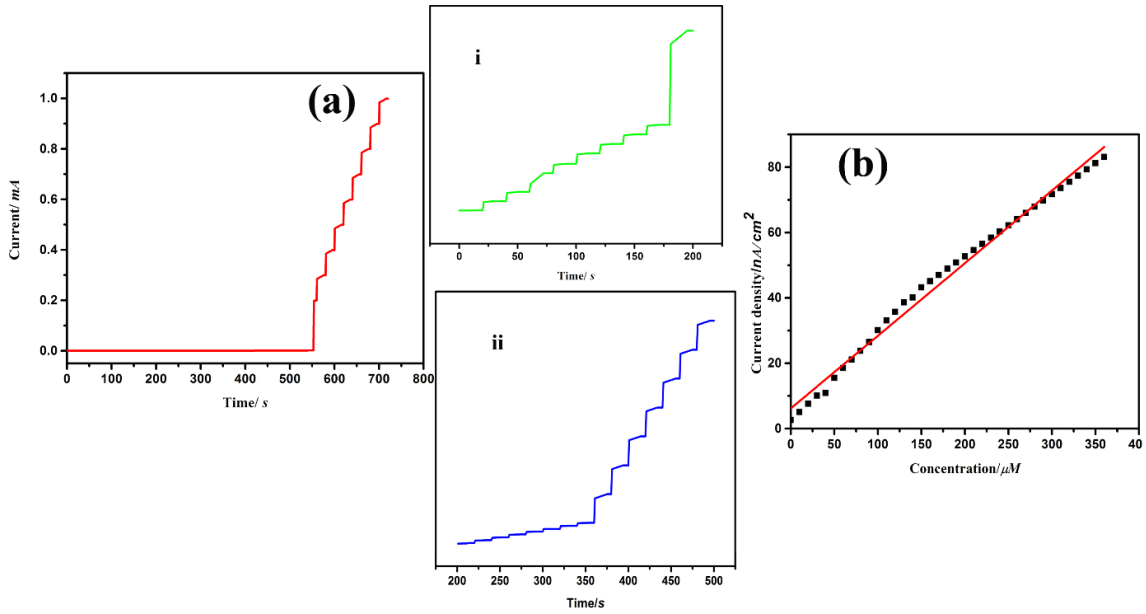

Figure 4.21 Amperometric studies on (a) GCE/GS/GNR in PBS (pH=7) at 0.07 V with different concentration of AA from 10 to 360 μM (i &ii) magnified image of A (b) Calibration curve.

The amperometric signal shows a linear correlation of AA concentration in the range of 10 to 360 μM with a sensitivity of 22 nA/μM cm^2 and LOD of 230 nM calculated by using 3σ/m, where σ is the standard deviation of blank and m is the slope value calculated from the calibration curve as shown in Figure 4.21(b).

The linear regression equation was expressed as:

$$j = 6.18633 * 10^{-9} + 2.22174 * 10^{-10} C_{AA} \quad (4.3)$$

With R = 0.99076. j is the current density and C_{AA} is the concentration of AA. The better performance of the GS/GNR towards AA with low over potential and lower detection limit was comparable with various electrodes as presented in Table 4.3.

Table 4.3 Comparison of electrochemical performance of different electrodes for AA sensor

Electrode material	Applied potential (mV)	Detection limit (μM)	Reference
CoPc-MWCNT/GC	190	1.0	(Zuo, Zhang, & Li, 2012)
CuNps/c-MWCNT/PANI/Au	400	1.0	(Chauhan, Narang, Rawal, & Pundir, 2011)

Ni-Pt alloys	200	-	(Weng & Hsiao, 2011)
Graphene/Pt-modified GCE	200	0.15	(C.-L. Sun, Lee, Yang, & Wu, 2011)
PdNPs-GO/GCE	100	-	(Wu et al., 2012)
PPF/GS electrode	370	0.12	(Keeley et al., 2010)
MSAPANI/MWCNTs/GCE	–	0.6	(Ying Liu et al., 2013)
Q-chitosan/C composite GCE	90	3	(Jirimali, Nagarale, Saravanakumar, Lee, & Shin, 2013)
GS/GNR/ modified GCE	80	0.23	This work

4.4.5 Interference, Sensor stability

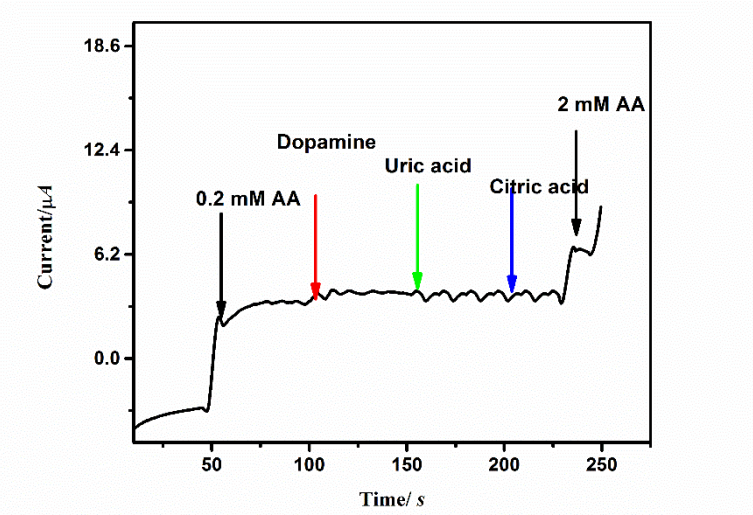

Figure 4.22 Interference study on GCE/GS/GNR in PBS (pH=7) at 0.07 V with 0.2 mM AA and other interferents dopamine, citric acid and uric acid and also 2 mM concentration.

The GCE/GS/GNR selectivity towards AA, could be investigated by amperometric studies with the interfering compounds like dopamine, uric acid and citric acid in 2 mM concentration along with 0.2 mM AA in PBS (pH=7) with continuous stirring at 0.07 V. Negligible response observed in Figure 4.22, indicated GCE/GS/GNR is highly selective to AA.

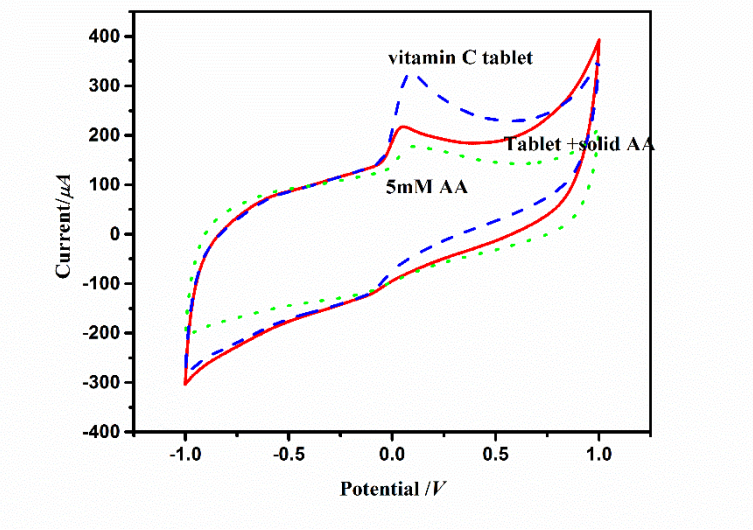

Figure 4.23 CV of GCE/GS/GNR in the solution containing 5 mM AA, vitamin C tablet and tablet with solid AA

The GCE/GS/GNR response was stable over a period of 50 min for 5 mM AA in 0.1 M PBS (pH-7) with a limited loss of 45.5% in the current signal. The current response measured three times for vitamin C tablets using the same electrode with a RSD of only 1.5% (Figure 4.23) confirms that the GCE/GS/GNR has a high stability.

4.5 Application of GCE/N_2/Ar/GS/GNR towards simultaneous determination of AA, DA and UA

In the last few decades, determination of AA (Arrigoni & De Tullio, 2002), DA (Wightman et al., 1988) and UA (Dutt & Mottola, 1974) has been of utmost important. Even the slight variation of their concentration can be used as an indicator for a wide variety of diseases like schizophrenia, parkinson's, gout, scurvy and cardiovascular diseases. Hence, simultaneous determination of these biomolecules, and in biological fluids is very important not only for investigating their physiological functions but also for diagnosing diseases.(Hadi & Rouhollahi, 2012)

In this section, as illustrated in Figure 4.14 (b), N_2/Ar RF plasma functionalized GS/GNR is employed to fabricate an electrochemical sensor for the simultaneous determination of AA, DA, and UA. Here, nitrogen plays a role in the enhancement of the electrocatalytic property, whereas the purpose of inert gas (Ar)

is to reduce amorphous carbon particles during N_2 functionalization without significantly affecting the structural stability of the GS/GNR.

4.5.1 Electrochemical characterization

The individual electrocatalytic activity of bare GCE, GCE/GS/GNR and GCE/N_2/Ar/GS/GNR towards AA, DA and UA, were first investigated by CV (Figure 4.24). In the case of AA, the oxidation peaks observed in all the three electrodes correspond to the hydroxyl groups oxidized to carbonyl groups in furan ring of AA. As depicted in Figure 4.24(a), among three electrodes, negative shift in the anodic peak potential of AA observed in GCE/N_2/Ar/GS/GNR, infers the enhanced electron transfer rate, which may be attributed to the abundant pyrrolic-N structure in N_2/Ar/GS/GNR.

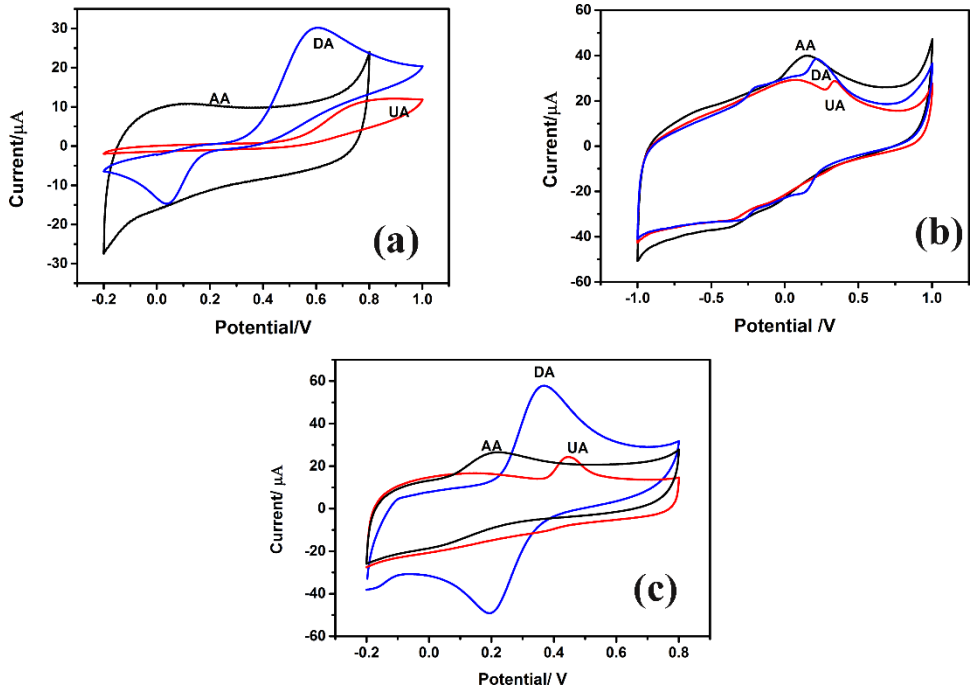

Figure 4.24 CV of 1.0 mM AA, 1.0 mM DA and 1.0 mM UA in 0.10 M PBS (pH 7.4) at (a) GCE, (b) GCE/GS/GNR and (c) GCE/N_2/Ar/GS/GNR at a scan rate of 100 mV/s.

In all the three electrodes, a well-defined redox couple appeared towards DA corresponds to two-electron oxidation of DA to quinone and the subsequent reduction of dopamine quinone to DA. Figure 4.24(b) depicts the anodic peak currents (I_{pa}) for 1 mM DA, for the bare GCE and GCE/GS/GNR of 7.38 μA and 10.76 μA, respectively. The I_{pa} of GCE/N_2/Ar/GS/GNR is much larger (24.49 μA) than that of the bare GCE and GCE/GS/GNR. This enhanced redox peak current

observed in GCE/N_2/Ar/GS/GNR could be due to three main reasons: one due to the π–π interactions between the benzene ring of DA molecule and the carbon layer. Second, because of the hydrogen bonds formed between hydroxyl or amine group in DA molecule. Thirdly due to the enhanced electrocatalytic property of nitrogen atoms within GS/GNR layers. From Figure 4.24(c), a well-defined oxidation peak observed in all the three cases, reveals that UA gets oxidized to quinonoid. The positive shift of UA oxidation peak from +333 mV (GCE/GS/GNR) to +446 mV (GCE/N_2/Ar/GS/GNR), infers that GCE/N_2/Ar/GS/GNR can simultaneously detect AA, DA and UA without any overlapping of oxidation potential of the three analytes. From CV it is evident that AA, DA and UA molecules with different structures have different interaction modes with the mentioned three electrodes. The above investigations demonstrate that GCE/N_2/Ar/GS/GNR exhibits the enhanced electrocatalytic performance, than the other two electrodes namely GCE and GCE/GS/GNR, with decrease in the overpotential and increase in the peak current by about three times toward the electrooxidation of AA, DA and UA.

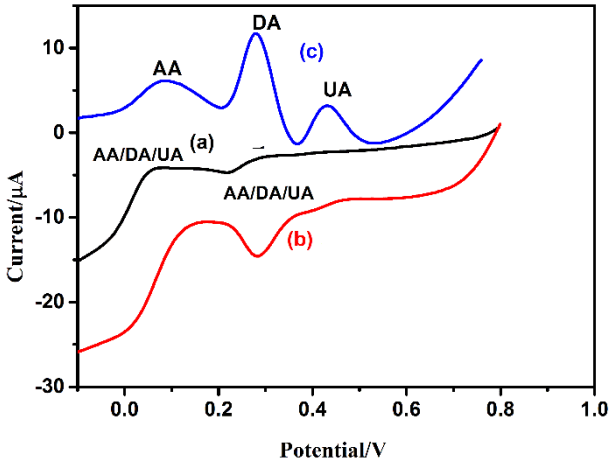

Figure 4.25 DPV of GCE, GCE/GS/GNR and GCE/N_2/Ar/GS/GNR in 1000μM AA, 50 μM DA and 100μM UA in 0.1M PBS (pH 7.4).

This could be attributed to its unique structural features and improved electrochemical property of GCE/N_2/Ar/GS/GNR, where the nitrogen atoms in N_2/Ar/GS/GNR may interact with the target molecules via hydrogen bonds, which can activate the hydroxyl and amine groups and accelerate the charge transfer kinetics of the target molecules. Moreover, the enhanced electrochemical surface area of N_2/Ar functionalized GS/GNR can provide more active sites, which

significantly improves its electrocatalytic activity. In other words, the excellent electrocatalytic activities of GCE/N_2/Ar/GS/GNR may also be due to the hybrid structure of GS/GNR and properties originating from the nitrogen/argon plasma functionalization effect. All these results indicate that GCE/N_2/Ar/GS/GNR possesses excellent electrocatalytic activity, which can effectively separate the oxidation potentials and improve the oxidation peak currents towards AA, DA and UA.

The excellent electrocatalytic activity of GCE/N_2/Ar/GS/GNR towards these three biomolecules in the tertiary mixture were also investigated by the DPV experiments (Figure 4.25) with a mixture of 1.0 mM (AA), 50 μM (DA) and 100 μM (UA) in 0.1 M PBS (pH 7.4). The electro-oxidation of the three biomolecules, at GCE and GCE/GS/GNR, presents a broad peak attributed to overlapping of AA, DA and UA, which infers that simultaneous determination of these molecules does not take place in GCE and GCE/GS/GNR. On the contrary, in the case of GCE/N_2/Ar/GS/GNR, it would be noted that the anodic peak potentials of AA (60 mV), DA (280 mV) and UA (432 mV) were well separated, making GCE/N_2/Ar/GS/GNR a promising electrode for simultaneous determination of these three biomolecules with higher peak current intensity and larger peak potential separation ($\Delta E_{AA–DA}$ = 220 mV, $\Delta E_{DA–UA}$ = 152 mV, $\Delta E_{AA–UA}$ = 372 mV). It clearly demonstrates that GCE/N_2/Ar/GS/GNR is a potential electrode material in the electrochemical biosensor for simultaneous detection of DA, AA and DA.

Both the CV and DPV demonstrate that GCE/N_2/Ar/GS/GNR possesses good electrocatalytic activity towards the oxidation of these analytes. This could be attributed to its particular hybrid structure of two and one-dimensional microstructures and properties originating from N_2/Ar functionalization. For instance, various nitrogen moieties and additional defects created during N_2/Ar plasma functionalization facilitates electron transfer and enhances adsorption strength of biomolecules.

4.5.2 Effects of scan rate on the electrochemical response of AA, DA and UA

The influence of scan rate were studied to examine the kinetics of electrode reaction on the redox peak current and potential through the CV of 1 mM AA, 1mM DA and 1 mM UA in 0.1 M PBS with different scan rates at the GCE/N_2/Ar/GS/GNR. As

shown in Figure 4.26 a, c, e with increasing scan rate (10–100 mV s^{-1}), the oxidation peak potentials of AA, DA and UA on the as-prepared GCE/N_2/Ar/GS/GNR underwent small positive shifts, suggesting that the adsorption does not occur significantly on electrode in 0.1 M PBS (pH = 7.4) solution. The increase in redox current intensities with increasing scan rates between I_p and the $v^{1/2}$ (Figure 4.26 b,d,f), indicates that the electrochemical activity of GCE/N_2/Ar/GS/GNR on AA, DA and UA is the diffusion controlled process.

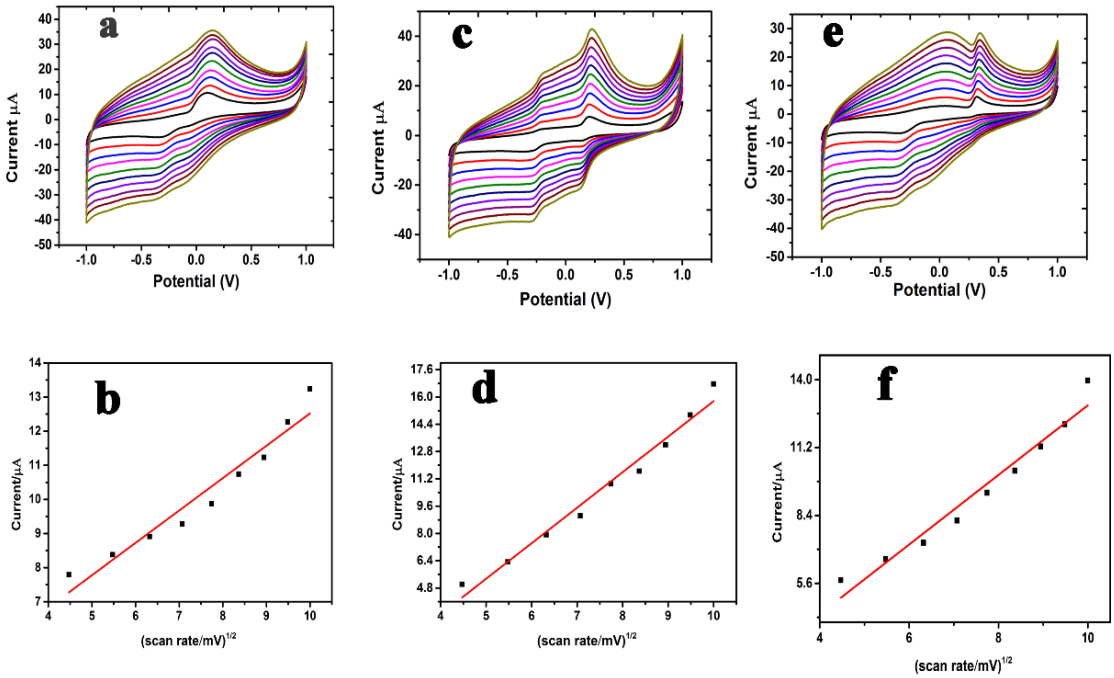

Figure 4.26 CV of N_2/Ar/GS/GNR /GCE in 0.1 M PBS solution (pH 7.4) containing 1 mM AA (a), 1 mM DA (c), and 1 mM UA (e) at different scan rates 10-100 mV s^{-1}. With their respective plots of the I_p vs $v^{1/2}$ (b, d, f).

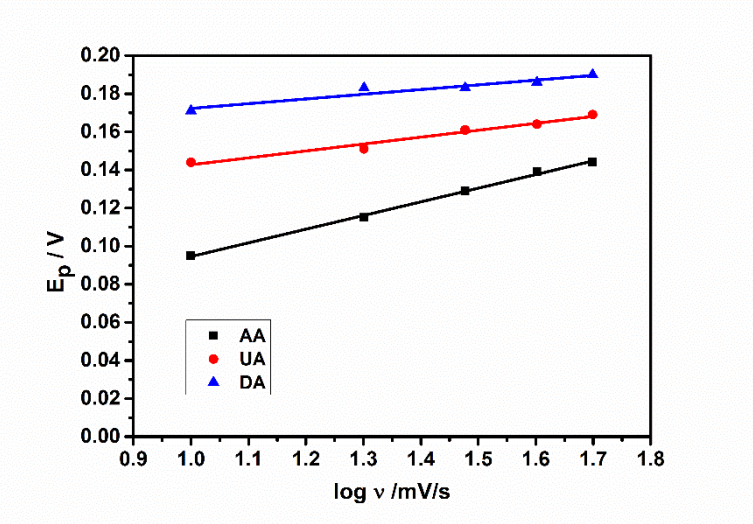

Figure 4.27 E_p vs log ν mV/s of N_2/Ar/GS/GNR /GCE in 0.1 M PBS solution (pH 7.4) containing 1 mM AA, 1 mM DA, and 1 mM UA at different scan rates 10-100 mV s^{-1}

Subsequently, from the Figure 4.27, the electrochemical parameter "α" electron transfer coefficient was calculated by using the obtained slope value between E_p and log υ in Laviron's equation (4.4) (Laviron, 1979).

$$\frac{2.3RT}{(1-\alpha)nF} = \text{slope value}\left(E_p \text{vs log} v\right) - - - - - - - \rightarrow (4.4)$$

The obtained "α" electron transfer coefficient are 0.08, 0.32 and 0.69 for AA, DA and UA, respectively by assuming two-electron transfer.

4.5.3 Effects of pH on the electrochemistry of DA, AA and UA

The effect of pH was investigated on the electrocatalytic oxidation of 1 mM AA, 50 µM DA and 100 µM UA at GCE/N_2/Ar/GS/GNR by DPV in 0.1 M PBS solution at a scan rate of 100 mV/s in the pH range of 4.0–9.0. With the increase of solution pH, the oxidation peak potentials of the three molecules gradually shifted negatively. The slope values of 30.8 mV, 60.8 mV and 65.7 V obtained from the linear relationships between peak potentials of AA, DA and UA and pH (Figure 4.28(a)), indicate that protons were directly involved in the overall oxidation reactions which occurred via electron transfer step followed by protonation process. The slopes are close to the theoretical value of 59 mV/pH (25 °C), indicating that their oxidation reactions are accompanied by the transfer of an equal number of protons and electrons. Besides, it was found that the separation of peak potentials for AA–DA and DA–UA and oxidation peak currents reached the maximum at pH

= 7.0 (Figure 4.28 (b) and (c)). Considering the effect of redox peak potential separation and current response, physiological pH value, pH = 7.4 was chosen in the following measurements.

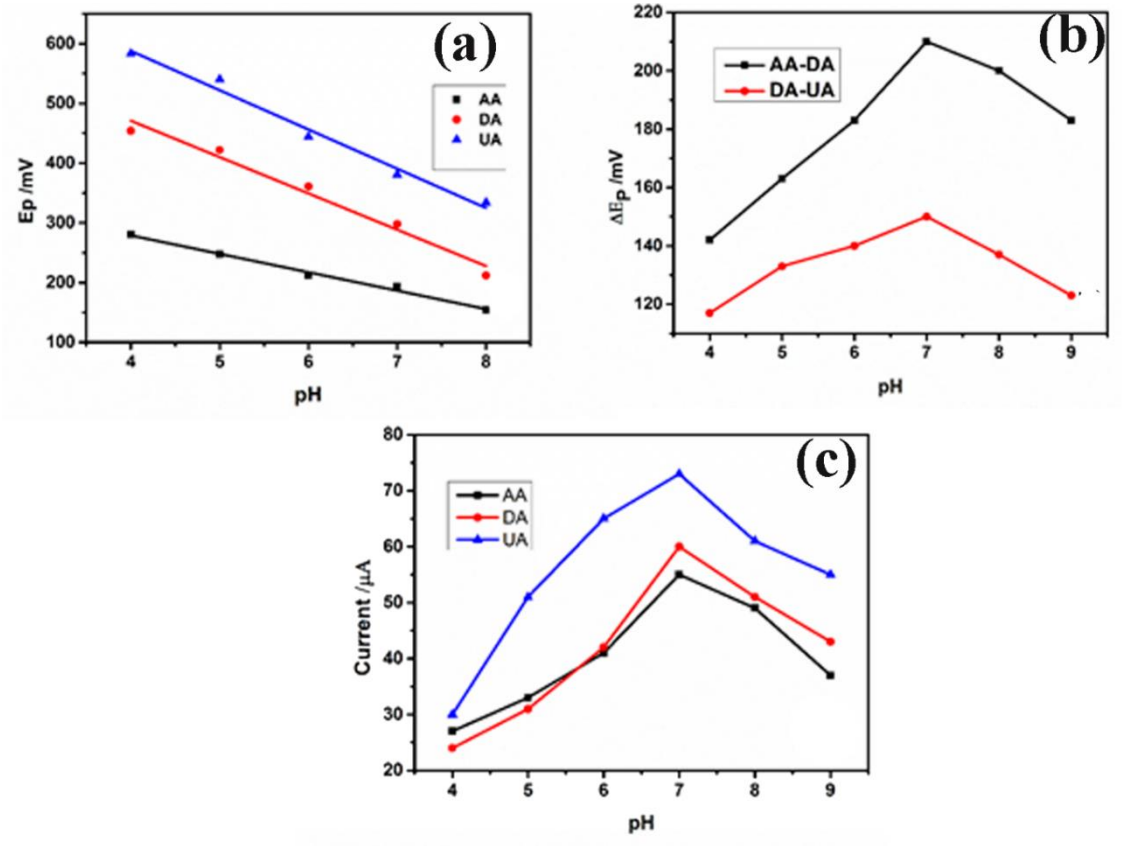

Figure 4.28 Effect of pH o the peak current (a), peak separation potential (b) and the peak potential (c) for the oxidation of 1 mM AA, 50 µM DA, and 100 µM UA in PBS buffer solution (pH 7.4) at the GCE/N_2/Ar/GS/GNR using DPV.

4.5.4 Amperometric response of AA, DA, and UA

The GCE/N_2/Ar/GS/GNR sensitivity towards AA, DA and UA was investigated by adding different concentrations of analytes into the electrolyte. Amperometric responses of GCE/N_2/Ar/GS/GNR was carried out under constant magnetic stirring upon successive addition of aliquots (20 µL) of AA, DA, or UA stock solution in PBS of pH 7.4 at 20 s interval at the optimum working potential (0.06 V for AA, 0.280 V for DA, and 0.430 V for UA, respectively). Figure 4.29 a, c, e shows the amperometric responses of GCE/N_2/Ar/GS/GNR to the successive addition of AA, DA, or UA into the PBS buffer. Initially, only PBS (15 mL, 0.1M, pH 7.4) was present in the cell. After the successive addition of 20 µL aliquots with the given concentration range, GCE/N_2/Ar/GS/GNR shows rapid response with a step-like

increase of responding current towards the concentration of the analyte and attained the steady-state current within 5 s demonstrating its fast response.

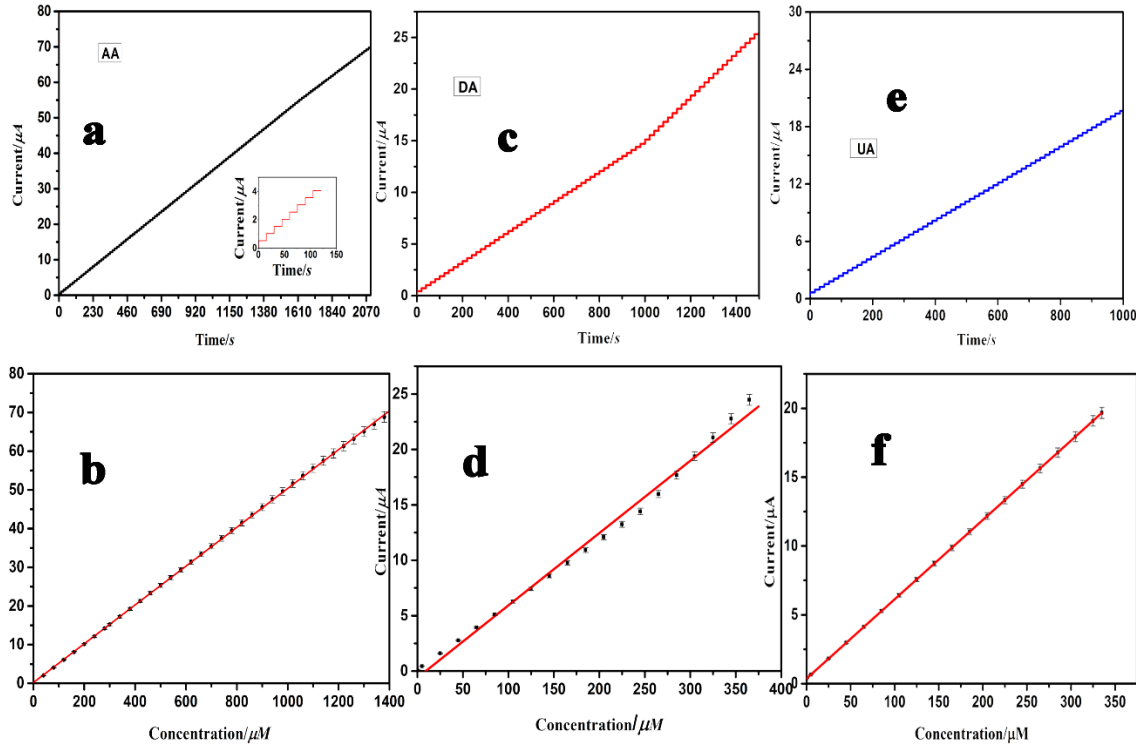

Figure 4.29 Amperometric curve of N_2/Ar/GS/GNR /GCE in 0.1 M PBS (pH 7.4) with successive additions of (a) 0.1–1400 µM AA, (b) 0.01–400 µM DA, (c) 0.02–350 µM UA, and (d, e, f) their calibration plots between the peak current intensities and the concentrations. The working potential was 0.06 V for AA, 0.28 V for DA and 0.43 for UA.

The calibration curves between current vs concentration (Figure 4.29 b, d, e) illustrate a linear relation in the range of 0.1 to 1400 µM, 0.01 to 400 µM and 0.02 to 350 µM, corresponding to AA, DA and UA respectively. GCE/N_2/Ar/GS/GNR sensitivity was estimated by using the slope of the calibration curve, as 501 µA/µM cm^2, 652 µA/µM cm^2 and 576 µA/µM cm^2 for AA, DA and UA respectively. And detection limits of of AA, DA and UA were determined to be 5.3 nM, 2.5 nM and 5.7 nM, respectively, with a signal-to-noise ratio of 3.

The above electrochemical measurements evidenced the excellent electrocatalytic activity of GCE/N_2/Ar/GS/GNR towards AA, DA and UA with higher sensitivity and lower detection limit. The electrochemical performances including linear detection ranges, detection limits and the peak potential separations of

GCE/N_2/Ar/GS/GNR are comparable with those of other listed literature (Table 4.4).

Table 4.4 Comparison of the performances of sensors for the simultaneous determination of AA, DA and UA with those of sensors based on different matrices.

Electrode	Peak separation			LOD in µM			Ref
	ΔE_1	ΔE_2	ΔE_3	AA	DA	UA	
NGCE/GS	170	120	290	2.2	0.25	0.045	(Sheng et al., 2012)
HNCS/GCE	212	136	348	0.04	0.91	0.02	(C. Xiao et al., 2011)
Au/ZnO/NGCE/GS	195	198	393	5	0.4	0.8	(Xianlan Chen et al., 2016)
Pt NSs/C_{60}/GCE	176	132	308	0.43	0.07	0.63	(X. Zhang, Ma, & Zhang, 2015)
(ZnO–CuxO–PPy)/GCE	150	154	304	25	0.04	0.2	(Ghanbari & Hajheidari, 2015)
Au/RGO/GCE	200	110	310	0.5	1.4	1.8	(Caiqin Wang et al., 2014)
RGO/carbon fiber electrode	116	167	283	4.5	0.77	2.23	(Yang et al., 2014)
Chitosan/GCE/GS	165	90	255	50	1	2	(D. Han, Han, Shan, Ivaska, & Niu, 2010)
Pd/GS/chitosan/GCE	252	144	396	20	0.1	0.17	(Xue Wang et al., 2013)
N_2/Ar/GS/GNR	220	152	372	0.0053	0.0025	0.0057	This work

4.5.5 Interference, stability, repeatability and selectivity of N_2/Ar/GS/GNR based electrochemical sensor

The effect of other several possible interferential species such as glucose, l-cysteine, NaCl, KCl, $CaCl_2$, $MgSO_4$, $Fe(NO_3)_3$ towards simultaneous determination of AA (1000 µM), DA (50 µM) and UA (100 µM) using GCE/N_2/Ar/GS/GNR were examined.

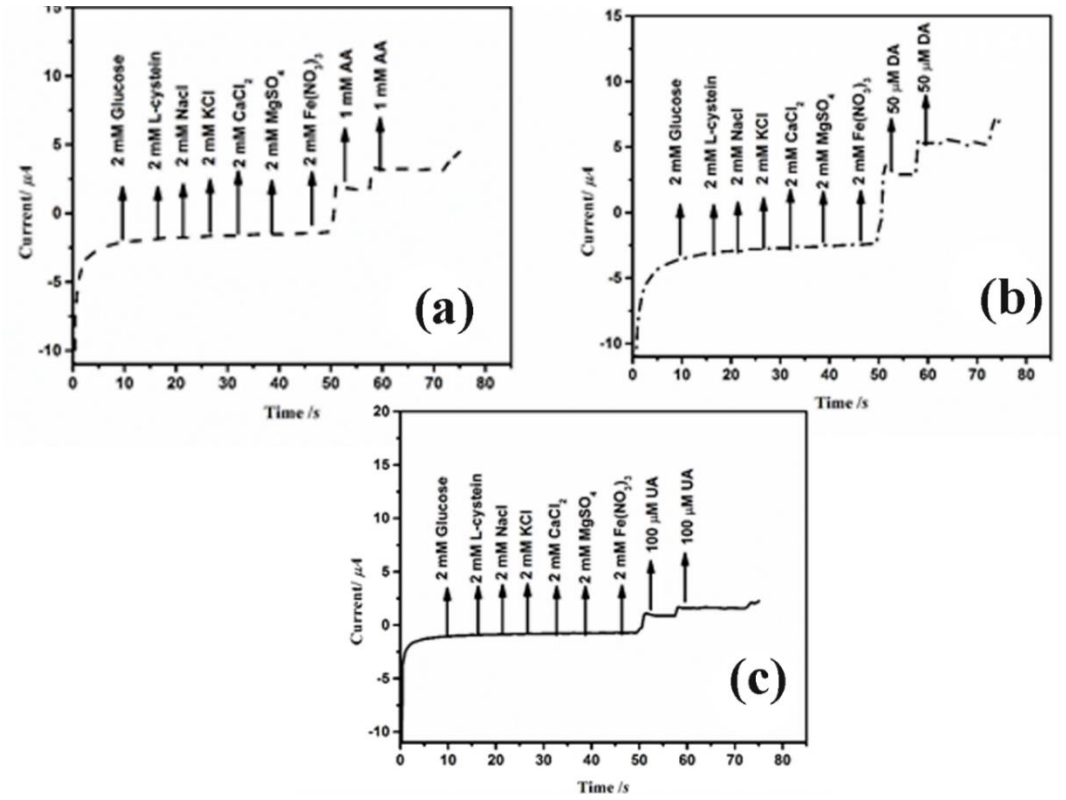

Figure 4.30 Interference study of GCE/N_2/Ar/GS/GNR in 2 mM of glucose, l-cysteine, NaCl, KCl, $CaCl_2$, M GSO_4, Fe $(NO_3)_3$ towards simultaneous determination of (a) AA, (b) DA and (c)UA at AA (1000 µM), DA (50 µM), and UA (100 µM).

It was found that the existence of afore mentioned species (2 mM) showed negligible interferences, revealing a good selectivity of GCE/N_2/Ar/GS/GNR (Figure 4.30 (a) AA, (b) DA, (c) UA). GCE/N_2/Ar/GS/GNR stability was determined by CV in a solution containing 1 mM AA, 50 µM DA, and 100 µM UA. Figure 4.31 clearly shows no significant change in peak current even after 50 consecutive cycles. To further calculate the long-term stability of the proposed sensor, the response of GCE/N_2/Ar/GS/GNR was recorded over a period of 30 days as depicted in Figure 4.32, there was a very little decay in the peak

currents of AA, DA and UA with the respective values of 2.7%, 3.6% and 2.8%. This clearly shows that proposed sensor retains excellent stability over a period of 30 days.

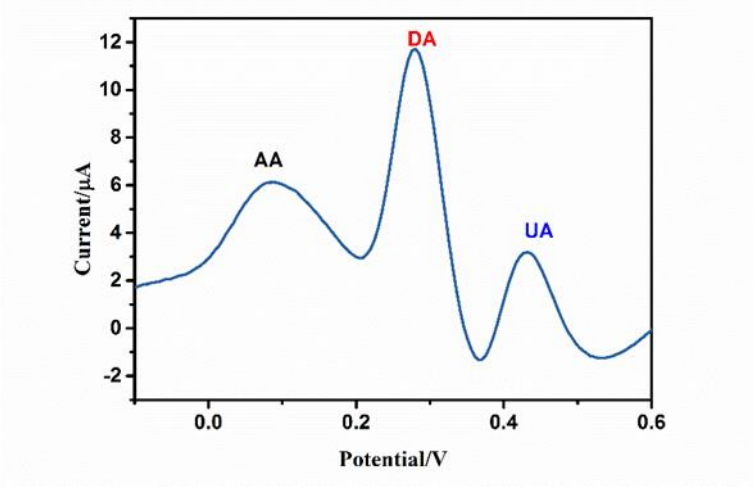

Figure 4.31 Repeatability of GCE/N_2/Ar/GS/GNR after 50 cycles

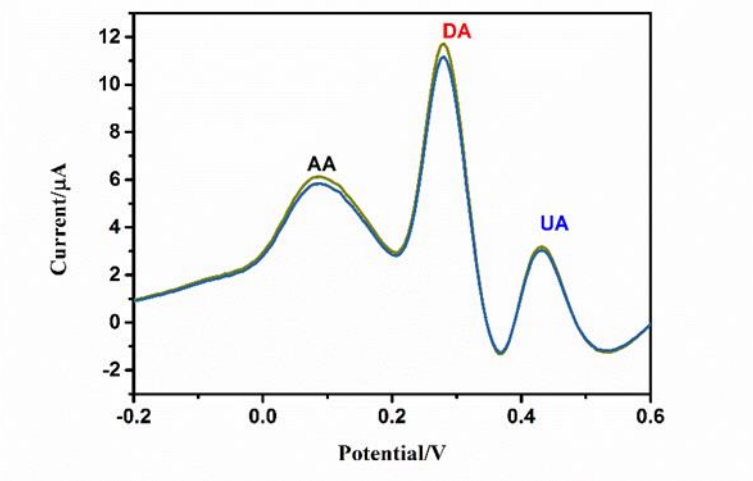

Figure 4.32 The stability of GCE/N_2/Ar/GS/GNR in 4° C after 30 days.

The repeatability of the proposed sensor was verified using three different electrodes. The RSD of the corresponding peak currents obtained for AA, DA and UA were 2.4%, 2.2% and 1.9% respectively, which suggests that proposed sensor possesses good repeatability.

Table 4.5 Determination of AA, DA and UA in human serum samples (n = 3).

Samples	Added µM			Found µM			Recovery %			RSD%		
	AA	DA	UA	AA	DA	UA	AA	DA	UA	AA	DA	UA
	0	0	0	6.62	0.323	17.9						
1	10	0.5	20	16.02	0.759	37.3	94	87.2	97	3.29	4.16	2.30
2	15	1	25	20.89	1.398	42.8	95.1	107.5	99.6	2.40	3.53	2.01
3	20	1.5	30	25.84	1.907	47.5	96.1	105.6	98.6	2.62	2.96	2.62
4	30	2	35	37.92	2.355	52.6	104.3	101.6	99.1	3.02	3.39	2.5
5	40	2.5	40	45.9	3.0	57.4	98.4	107.3	98.7	2.7	3.4	2.06

The practical applicability of N_2/Ar/GS/GNR in analytical determination of AA, DA and UA was carried out using five human serum samples using standard addition method. Serum samples taken from the lab, are diluted 50 times using 0.1 M PBS (pH 7.4). To authenticate the proposed sensor certain known amounts of AA, DA and UA are added to the diluted serum sample and then detected. The results obtained are tabulated in Table 4.5. The recovery of the spiked sample ranges between 94 and 104 % which validates the applicability of N_2/Ar/GS/GNR based sensor for real sample analysis.

4.6 Application of GCE/GS/GNR/Ni towards oxidation of glucose

The Ni/GS/GNR was applied to diagnose diabetes mellitus, a chronic disease related to glucose digestion caused by insufficient insulin secretion, resulting in increasing death rate worldwide. Therefore determination of glucose level in blood is of practical importance to reduce the complications associated with diabetes. In recent years considerable research have been devoted in development of vast number of rapid, sensitive and accurate glucose sensors to monitor glucose which are not only relevant to determination of glucose level in blood but also in the food industry, bioprocessing, etc (Wild, Roglic, Green, Sicree, & King, 2004). Among the various methods available for glucose sensor, such as high performance liquid chromatography method, spectrophotometric assay, polarimetry method and electrochemiluminescence (Shuang Song et al., 2008), (Kanchana, Sakai, Teshima, Katoh, & Grudpan, 2007), (Kang, Lee, Lee, & Jung, 2008), (X. Liu et al., 2008), electrochemical sensor has triggered extensive attention owing to its high

sensitivity, excellent selectivity, rapid response, lowest detection limit and good reliability (Singh et al., 2013). So, in this section, Ni incorporated into the network of GS/GNR hybrid by *in situ* chemical reduction method was further used for as a stable and sensitive non-enzymatic glucose sensor.

4.6.1 Electrocatalytic oxidation of glucose

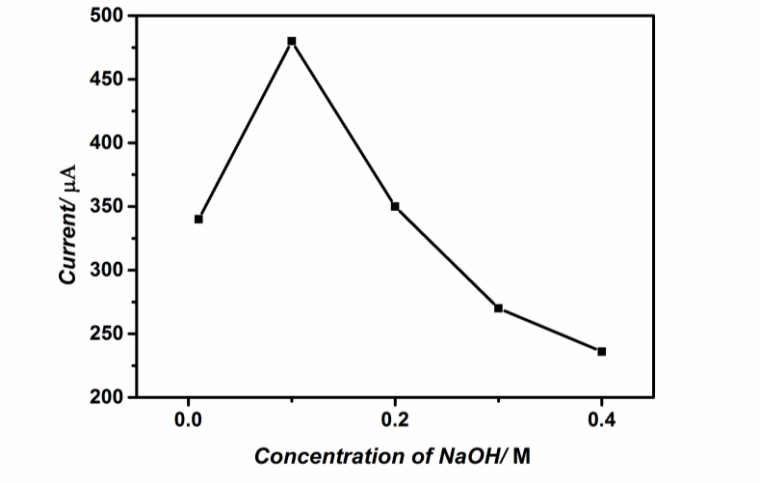

Figure 4.33 Effect of concentration of NaOH towards GCE/GS/GNR/Ni

Chemisorbed hydroxide ions (OH-) facilitate a stronger interaction between glucose and Ni based electrode and decrease the activation energy for the oxidation of glucose as follows. First, OH- neutralises the protons generated during the dehydrogenation steps; second, the formation of glucose intermediate occurs at a faster rate in alkaline solution; and third, the formation of NiOOH catalyst with the conversion of glucose intermediate to gluconolactone. Therefore, the effect of concentration of the electrolyte (NaOH) on the electroactivity of the catalytic material was investigated by CV measurements, with different concentrations of NaOH 0.01, 0.1, 0.2, 0.3 and 0.4 M. As illustrated in Figure 4.33, we observe increase in peak current at 0.01 M NaOH, further increase in NaOH concentration results in decreased oxidation peak due to the blockage of active sites on the electrode by the increased concentration of hydroxide ions. Therefore, 0.1 M NaOH was selected as the optimal concentration for the further experiments.

The electrocatalytic behaviour of GCE, GCE/GS/GNR, GCE/Ni and GCE/GS/GNR/Ni were evaluated by CV in alkaline medium with and without addition of glucose and illustrated in Figure 4.34. All CV experiments were carried out in the potential window of 0.0-1.0 V at a scan rate of 50 mV s^{-1}.

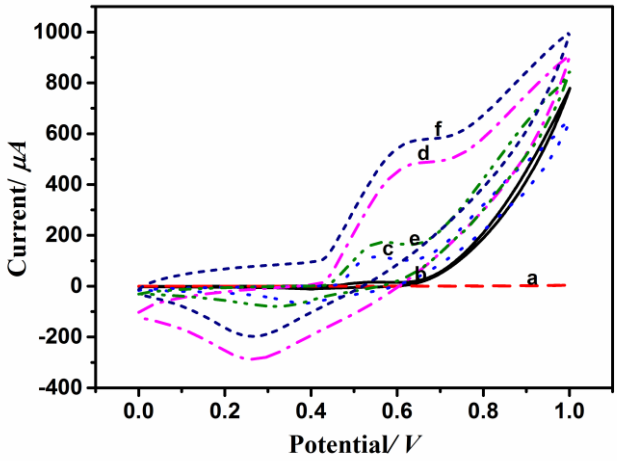

Figure 4.34. CV response of bare GCE (a); GCE/GS/GNR (b); GCE/Ni (c) & (e); GCE/GS/GNR/Ni (d) & (f) in 0.1 M NaOH; (a, b, c, d - in absence of glucose, e, f - in presence of 0.1 mM glucose); scan rate: 50 mV s^{-1}.

The CV obtained at bare GCE and GCE/GS/GNR revealed no redox behaviour, indicating that both the electrodes do not undergo redox reaction in 0.1 M NaOH (Xiaohui Gao, Lu, Liu, He, & Chen, 2015). In contrast, owing to excellent electrocatalytic properties of Ni nanoparticles, GCE/Ni and GCE/GS/GNR/Ni modified electrodes exhibited a pair of well-defined redox peaks, under an alkaline solution with E_{pa} and E_{pc} peak potential of +0.5 V and +0.3 V vs. Ag/AgCl respectively, which correspond to the redox reaction that occurs between Ni nanoparticles and OH to form $Ni(OH)_2$/NiO(OH), indicating that the modified electrodes exhibited significant electro catalytic activity in the alkaline medium and the involved electrochemical reaction as follows:

$$Ni(OH)_2 + OH^- \longrightarrow NiO(OH) + H_2O + e^- \longrightarrow (4.5)$$

Moreover, the observed oxidation peak current of the GCE/GS/GNR/Ni (Figure 4.35) was much higher than that of other electrodes. The superior electro catalytic performance of GCE/GS/GNR/Ni was attributed to the synergistic effect of GS/GNR hybrid network and Ni nanoparticles. In the hybrid network of GS/GNR/Ni, where Ni nanoparticles were uniformly dispersed on GS/GNR, the GS/GNR hybrid provides higher specific surface area, enhanced electrical conductivity and more active sites, providing a facile transport pathways for ions and offers unhindered diffusion of OH- during the electrochemical process.

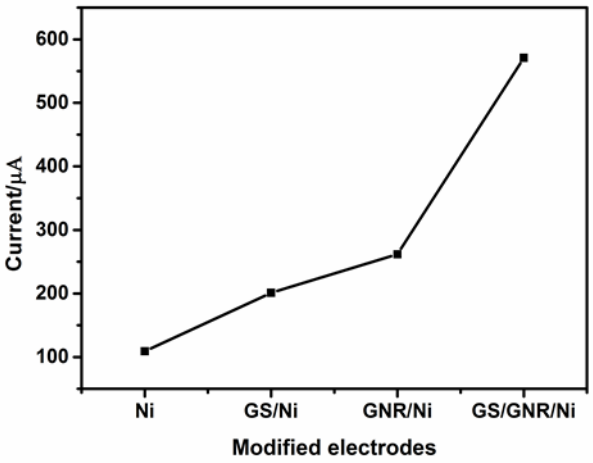

Figure 4.35 Peak current of GCE/Ni, GCE/GS/Ni, GCE/GNR/Ni and GCE/GS/GNR/Ni modified electrodes towards 0.1 M NaOH electrolyte.

Ni nanoparticles serve as excellent catalytic active material for direct glucose oxidation, which would further enhance the electron transfer resulting to high sensitivity, lower detection limit and good selectivity towards glucose detection. Similar catalytic mechanism was exhibited in the Cu_2O nanocubes incorporated on GS structures (Minmin Liu, Liu, & Chen, 2013). Upon addition of glucose, the significant increase of the oxidation current was ascribed to the fact that Ni was oxidized to $Ni(OH)_2$ on the surface of the GCE/GS/GNR/Ni electrode (equation (4.6)), and then glucose was catalytically oxidized to gluconolactone, further to gluconic acid by a hydrolyzation process (equation (4.6 and 4.7)). In addition, due to the adsorption of glucose and the oxidized intermediates on the active sites in Ni/GS/GNR based electrode, the anodic peak potential shifts to a little positive direction. It was also ascribed to the diffusion limitation of glucose at the electrode surface; these results are consistent with the previous reported works on Ni (Sivasakthi, Ramesh Bapu, & Chandrasekaran, 2016).

The mechanism for oxidation of glucose by Ni nanomaterials can be described by the following reactions (Joseph Wang, Chen, & Chatrathi, 2004), (L.-M. Lu et al., 2009).

$$NiO(OH) + \text{glucose} \longrightarrow Ni(OH)_2 + \text{gluconolactone} \quad (4.6)$$

Finally, gluconolactone was turned into gluconic acid by hydrolysis:

$$\text{Gluconolactone} \longrightarrow \text{gluconic acid} \quad (4.7)$$

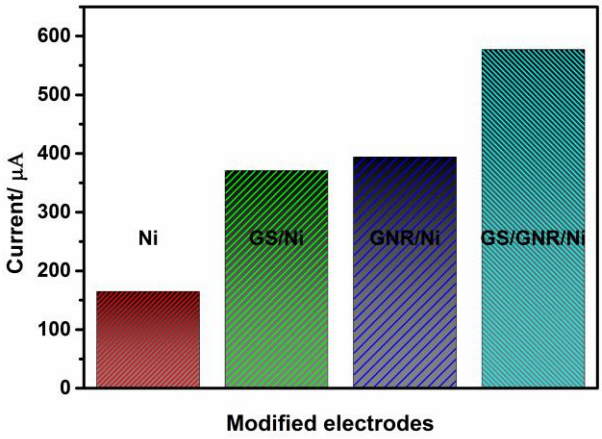

Figure 4.36 Peak current of GCE/Ni, GCE/GS/Ni, GCE/GNR/Ni and GCE/GS/GNR/Ni modified electrodes towards 0.1 M NaOH electrolyte in presence of 0.1 mM glucose.

The electro oxidation of glucose towards GCE/GS/GNR/Ni was investigated along with other electrodes such as GCE/Ni, GCE/GS/Ni, and GCE/GNR/Ni and illustrated in Figure 4.36. Among the modified electrodes GCE/GS/GNR/Ni shows significant enhancement in oxidation peak currents. The excellent electrochemical performance observed at GCE/GS/GNR/Ni was ascribed to GS/GNR hybrid network which improves the glucose sensing not only by large surface area and better dispersion of Ni nanoparticles, but also by high electrical conductivity and charge transfer capability.

Moreover during co-reduction of GOS, GOR and $Ni(OH)_2$ the ample functional groups available in both the edges and basal of GOS and GOR, provide more anchoring sites for the incorporation of more Ni nanoparticles i.e catalytic site and enhance the rate of electron transfer between glucose and the electrode. Also the homogeneously dispersed Ni nanoparticles over the GS/GNR matrix extended the electroactive surface area of Ni/GS/GNR material, which further improved the adsorption of analyte.

4.6.2 Electro-kinetic studies

To evaluate the kinetics of glucose oxidation on the surface of GCE/GS/GNR/Ni, CV were recorded at different scan rates ranging between 10 and 100 mV s^{-1} and depicted in Figure 4.37. The peak potential for the oxidation of glucose shifts to

positive values, along with increase in oxidation and reduction peak currents with increasing scan rate from 10 to 100 mV s^{-1} (Figure. 4.37 a and b).

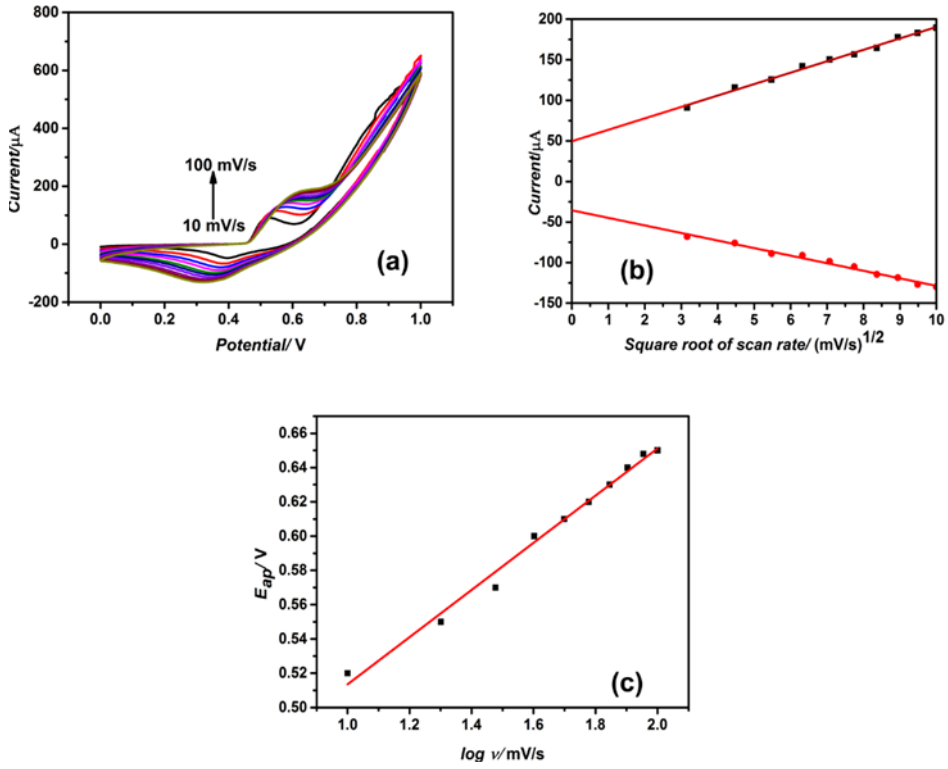

Figure 4.37 (a) CV of the GCE/GS/GNR/Ni electrode at different scan rates (10-100 mV/s), (b) I_p *vs* $v^{1/2}$ (c) E_p *vs* log (v).

The linear relationship between the peak current and square root of scan rate with a linear regression equation of

$$I_p = 4.9608 + 1.4076v^{\frac{1}{2}}\left(mv^{\frac{1}{2}}s^{-\frac{1}{2}}\right) R = 0.9972 \longrightarrow (4.8)$$

indicates that the oxidation of glucose on the surface of GCE/GS/GNR/Ni is diffusion controlled (Shen et al., 2016). As shown in Figure 4.37c, the E_{pa} was linearly dependent on the logarithm of the scan rate.

The electrochemical parameters for instance electron-transfer coefficient (α) and apparent charge-transfer constant (k_s) can be calculated using Laviron's model (Laviron, 1979).

$$E_{pa} = E^o + \frac{RT}{(1-\alpha)nF} ln \frac{(1-\alpha)}{m} \longrightarrow (4.9)$$

$$E_{pc} = E^o - \frac{RT}{\alpha nF} ln \frac{\alpha}{m} \longrightarrow (4.10)$$

$$\log k_s = \alpha \log(1-\alpha) + (1-\alpha)\log\alpha - \log\frac{RT}{nFv} - \frac{\alpha(1-\alpha)nF\Delta E_p}{2.3RT} \longrightarrow (4.11)$$

where m = (RT/F)(k_s/αn)------(4.12), n is the number of electrons transferred in the rate-determining step, ΔE_p is the peak potential separation, R is the gas constant (8.314 J mol^{-1} K^{-1}), T is the room temperature (298 K) and F is Faraday`s constant (96,485 C mol^{-1}), and v is the scan rate. α and k_s as determined from these plots and Eq. (4.13) to be 0.43 and 2.37 s^{-1}, respectively were higher than Nafion/SBA-15-Cu (II) modified GCE (Shamsipur, Karimi, Amouzadeh Tabrizi, & Rostamnia, 2017). This indicates that the GCE/GS/GNR/Ni electrode can effectively promote electron transfer.

4.6.3 Impedance studies of modified electrodes

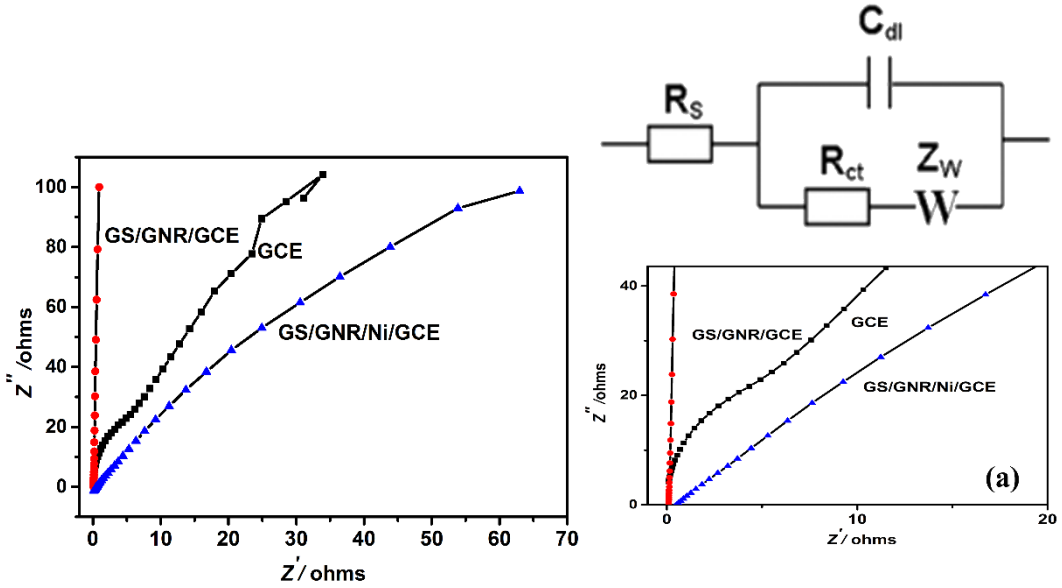

Figure 4.38 EIS spectra of GCE, GCE/GS/GNR and Ni/GS/GNR/ GCE electrodes in a 1 M KCl electrolyte with 5 mM $K_3[Fe(CN)_6]$ and 5 mM $K_4[Fe(CN)_6]$ with Randles circuit along with (a) magnified portion of Nyquist plot.

The impedance measurements of GCE, GCE/GS/GNR and GCE/GS/GNR/Ni were performed in 1 M KCl with 5 mM $K_3[Fe(CN)_6]$ and 5 mM $K_4[Fe(CN)_6]$ and shown in Figure 4.38. After fitting the data, among the three modified electrodes, the R_{ct} value of GCE/GS/GNR/Ni is found to be significantly less (17 Ω) compared to GCE/GS/GNR (140 Ω), and GCE (15700 Ω). The decreased charge transfer resistance was attributed to the hybrid network of graphene sheet and graphene nanoribbon which not only enhances the surface area available for Ni incorporation but also accelerates the rate of electron transfer, thereby increasing the electrical conductivity and decreasing the charge transfer resistance, effectively enhancing the detecting sensitivity and shortening the response time.

4.6.4 Optimization of potential in glucose sensing

The effect of increase in concentration of glucose towards GCE/GS/GNR/Ni was studied elaborately by amperometric method. Considering that the amperometric response of the sensor can strongly be influenced by the applied potential, we have investigated the optimum potential for the amperometric determination of glucose. The amperometric response of GCE/GS/GNR/Ni electrode with successive addition of 0.1 mM of glucose in 0.1 M NaOH in the potential range of +0.4 to +0.7 V vs. Ag/AgCl was illustrated in Figure 4.39. When the applied potential is increased from +0.4 V to +0.5 V, the oxidation current of glucose was increased gradually with the successive addition of 0.1 mM glucose. As shown in the inset, the response current reaches the maximum value at +0.5 V.

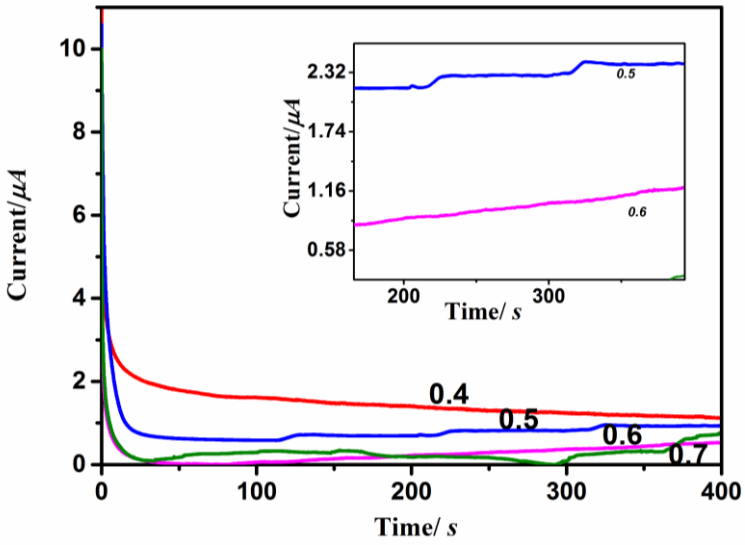

Figure 4.39 Amperometric response of the GCE/GS/GNR/Ni at different potentials with successive addition of 0.1 mM glucose into 0.1 M NaOH solution. Inset: Magnified view of current response.

However, the current response was decreased when the applied potential further increased. The reason for this phenomenon can be explained by the fact that the generation of many interfering substances interacted with the electrode, which leads to the decayed current. By comparison, the applied potential of +0.5 V enabled the best performance, which was selected as the suitable working potential for glucose detection in subsequent experiments, which is also potentially beneficial for elimination of interferences from electroactive substances such as DA, UA and AA.

4.6.5 Amperometric detection of glucose

The sensitivity of GCE/GS/GNR/Ni towards glucose detection was investigated by adding different concentrations of glucose into the electrolyte. Amperometric responses of GCE/GS/GNR/Ni upon successive addition of certain amount of glucose to 0.1 M NaOH was carried out under constant magnetic stirring at the optimum potential of 0.5 V. Figure 4.40 (a) illustrates the current response recorded with respect to time for the GCE/GS/GNR/Ni with the incremental addition of glucose. Figure 4.40 (b) represents calibration curve (current vs concentration) for the electrochemical responses of the GCE/GS/GNR/Ni with the successive injection of 10 µL glucose with concentration ranging between 5 nM and 5 mM. The wide linear range might be due to the larger surface area with more electro active sites for the oxidation of glucose at GCE/GS/GNR/Ni. We observed a step-like increase of responding current towards glucose and it attained 95% of the steady current within 5 s demonstrating its fast response. In addition, the fast response may be due to the promoted electron transfer and excellent catalytic activity provided by Ni nanoparticles and the hybrid structure of GS/GNR (Shamsipur et al., 2017).

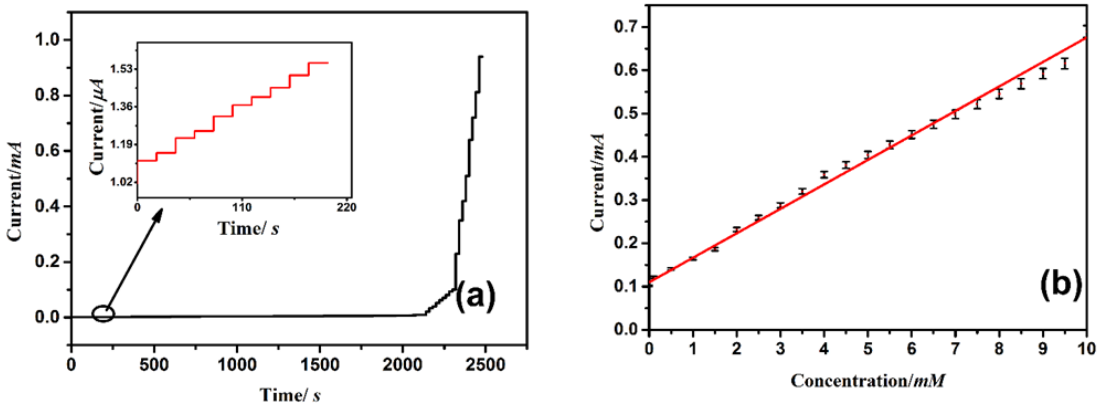

Figure 4.40 (a) Amperometric i-t response of GCE/GS/GNR/Ni with the successive addition of different concentrations of glucose in the range of 5 nM - 5mM in 0.1 M NaOH at an applied potential of 0.5 V vs. Ag/AgCl with time interval 20 s (Inset: Magnified view of time response from 0 - 220 s) and (b) Calibration curve for glucose concentration ranging between 5 nM and 5 mM with the error bars indicating the standard deviation of triplicate determinations.

The sensor displays a linear relationship between the current response and glucose concentration for a range of 5 nM - 5 mM glucose with a correlation coefficient of 0.9975, high sensitivity of 2.32 mA/mM cm^2 and detection limit of 2.5 nM with a

signal-to-noise ratio of 3. The high sensitivity and low detection limit of GCE/GS/GNR/Ni electrode can be attributed to the excellent electrocatalytic property toward the oxidation of glucose owing to the unique structure of hybridised graphene sheet and nanoribbon which provides enhanced area for loading more Ni nanoparticles which provide many active sites for the oxidation of glucose. The GS/GNR structure can also facilitate the diffusion of glucose molecules and accelerate the electron transfer.

A list of the reported non-enzymatic glucose sensors based on Ni is shown in Table 4.6; it can be seen that the analytical performance of the sensor proposed in this study is better than most of the previous studies in terms of sensitivity, LOD, and linear range.

Table 4.6 Comparison of performance of as-fabricated glucose sensor with other glucose sensors reported previously.

Electrode	Sensitivity	Linear range	LOD	Ref
Ni/GS/GNR	2.32 mA mM^{-1} cm^{-2}	5 nM-5 mM	2.5 nM	This work
PVP[a]/GS/NiNPs[c]-CS[b]	103.8 µA mM^{-1} cm^{-2}	0.1µM-0.5 mM	30 nM	(Z. Liu, Guo, & Dong, 2015)
CNT/Ni NAs[d]	1381 µA mM^{-1} cm^{-2}	0.5-10 mM	1µM	(J. Zhu et al., 2011)
Ni NWs[e]	367 µA mM^{-1} cm^{-2}	1 µM–5 mM	1µM	(Jinhong Wang, Bao, & Zhang, 2012)
CNT/Ni	1384.1 µA mM^{-1} cm^{-2}	5 µM–2 mM	2µM	(Choi et al., 2015)
PAA[f]/Ni	---------	5 µM-12 mM	0.65µM	(T. Liu et al., 2016)
NiNPs/GN[g]	865 µA mM^{-1} cm^{-2}	5µM-0.55mM	1.85µM	(B. Wang, Li, Liu, & Yu, 2014)
NiNPs/CNF[h]	420.4 µA mM^{-1} cm^{-2}	2µM-2.5mM	1µM	(Yang Liu, Teng, Hou, & You, 2009)

NiNPs/BDD[i]	1040 µA mM^{-1} cm^{-2}	10µM-10 mM	2.7µM	(Toghill, Xiao, Phillips, & Compton, 2010)
Ni/PSi[j]-CPE[k]	----------	2 µM-5000 µM	0.2 µM	(Ensafi et al., 2017)
RGO/$Ni(OH)_2$[l] /GCE	11.43 mA mM^{-1} cm^{-2}	2µM-3.1 mM	0.6µM	(Yue Zhang et al., 2011)
NiO[m]/HMS[n]/GCE	2.39 mA mM^{-1} cm^{-2}	1.67 µM–6.87 mM	0.53µM	(Ci et al., 2014)
AgNPs[o]/CPE	540.7 µA mM^{-1}	28.6 µM-9.80 mM	5.5 µM	(Ghiaci, Tghizadeh, Ensafi, Zandi-Atashbar, & Rezaei, 2015)
s-NiO[p]/GD[q]	36.13mA mM^{-1} mm^{-2}	Upto 10.0 mM	0.9µM	(Hu Liu et al., 2015)
AgNPs/F-MWCNTs[r] /GCE	1057.3 mA mM^{-1}	1.3 - 1000 mM	0.03 mM	(Ensafi et al., 2016)
$Ni(OH)_2$/NND[s]	3.20 and 1.41 mA mM^{-1} cm^{-2}	0.02–1 mM and 1–9 mM	1.2 µM	(Ko, Huang, Raina, & Kang, 2013)
Pd[t]/NiO/Nile–RGO/CPE	----------	0.020–20.0 mM	2.2 µM	(Ensafi, Ahmadi, Jafari-Asl, & Rezaei, 2015)

[a] PVP- poly vinyl pyrrolidene
[b] CS -chitoson
[c] NPs -nanoparticles
[d] NAs- nanostructuted arrays
[e] NWs -nanowires
[f] PAA -poly(azure A)
[g] GN -Graphene sheet
[h] NiNPs-CNF- Ni nanoparticles loaded carbon nanofiber.
[i] BDD- boron-doped diamond
[j] Psi-porous silicon
[k] CPE – carbon paste electrode

[l]$Ni(OH)_2$- nickel hydroxide
[m]NiO-nickel oxide
[n]HMS-hollow micro sphere
[o]Ag-Silver
[p]s-NiO- porous NiO nanosheets
[q]GD-graphite disks
[r]F-MWCNTs-functionalized multiwall carbon nanotubes
[s]NND-nitrogen-incorporated nanodiamonds
[t] Pd-palladium

4.6.6 Interference, stability and repeatability of the sensor

In physiological fluids, endogenous species such as ascorbic acid (AA), uric acid (UA), sodium chloride (NaCl), sucrose and dopamine (DA) generally co-exist with glucose. Hence, the effect of these species towards the selectivity of GCE/GS/GNR/Ni on glucose detection was investigated and illustrated in Figure 4.41. While, the normal physiological level of glucose in human blood is 4.4–6.6 mM (Ensafi et al., 2015) and various endogenous species which could hinder the performance of GCE/GS/GNR/Ni are below 0.1 mM. The interference experiment study was undertaken with the addition of 0.5 mM glucose, followed by consecutive injection of 0.01 mM of each ascorbic acid (AA), uric acid (UA), dopamine (DA), NaCl and sucrose by amperometric method. Negligible current response observed towards addition of interferents demonstrates that the glucose sensor based on GCE/GS/GNR/Ni has high selectivity for possible practical applications.

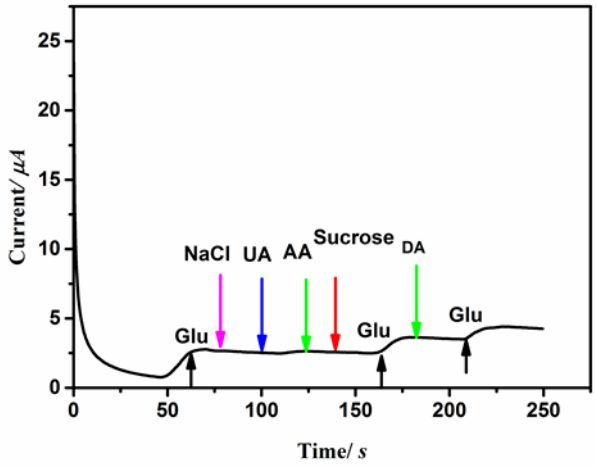

Figure 4.41 Effect of interferents, 0.01 mM of AA, UA, NaCl, sucrose and DA on the response of the GCE/GS/GNR/Ni to glucose of 0.5 mM in NaOH at 0.5 V.

Moreover, long-term stability of the fabricated Ni/GS/GNR/ GCE electrode was investigated by measuring the change in current response over 30 days period as depicted in Figure 4.42. The electrode was stored in air at room temperature and

their current response was investigated every three days after injecting 0.5 mM glucose to 0.1 M NaOH electrolyte. The response current was decreased by only 8.7% from its original current and became saturated after 30 days, which suggests that the fabricated GCE/GS/GNR/Ni has good long term stability.

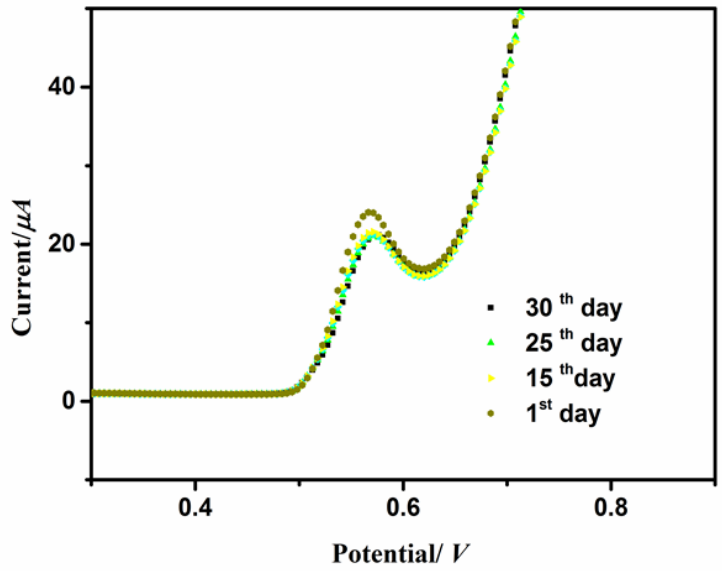

Figure 4.42 Long-term stability of GCE/GS/GNR/Ni modified electrode stored at 4°C after 30 days in 0.5 mM glucose.

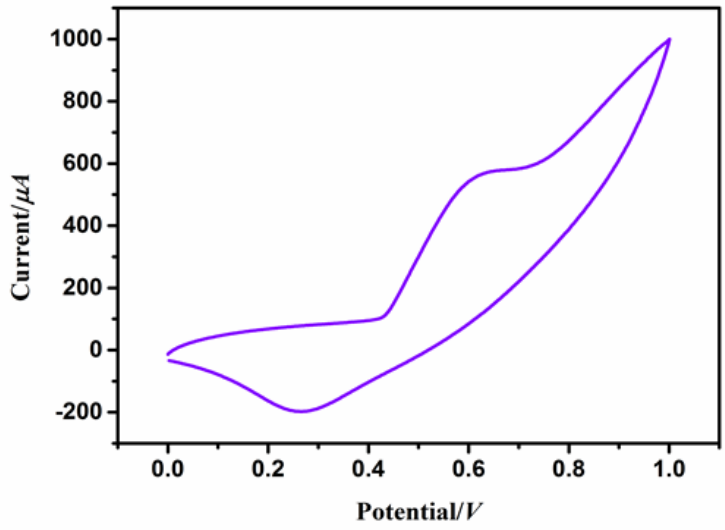

Figure 4.43 Repeatability of GCE/GS/GNR/Ni in 0.5 mM glucose by measuring 30 successive CV measurements.

Furthermore, the stability of sensor was also evaluated by measuring the response current of 30 successive CV measurements of 0.5 mM glucose in 0.1 M NaOH with single electrode. No obvious change in peak current was observed as shown in

Figure 4.43 which reveals that Ni nanoparticles incorporated with GS/GNR efficiently enhance the stability of the sensor material towards consecutive cycle. The repeatability of as-fabricated GCE/GS/GNR/Ni electrode was also verified using the amperometric responses of glucose (500.0 μmol L^{-1}) at a series of freshly prepared five electrodes. The RSD of 2.16%, indicates that the fabricated sensor possesses good repeatability.

4.6.7 Real sample analysis

The reliability of the GCE/GS/GNR/Ni sensor was also evaluated by determining the glucose level in human serum using standard addition method. In brief, five serum samples obtained from healthy donors were diluted with 10 mL of 0.1 M NaOH. The obtained results were consistent with the blood glucose meter (Figure 4.44) with recovery rates of glucose detection of ≥95%. This strongly suggests that the fabricated GCE/GS/GNR/Ni electrode can be successfully utilized for glucose detection in blood samples without any pre-treatment step.

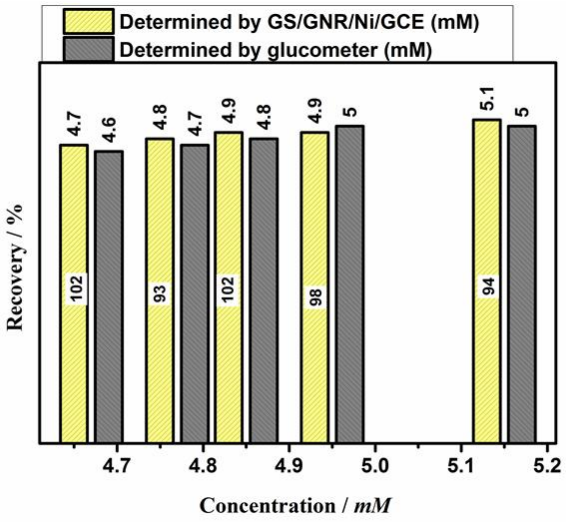

Figure 4.44 The bar chart showing the glucose recovery in human serum samples as determined between commercial glucose meter and GCE/GS/GNR/Ni.

This superior performance of Ni/GS/GNR based non-enzymatic glucose sensor can be ascribed to the excellent conductivity of GS/GNR, where the GNR incorporated between the GS layers could prevent the restacking of graphene sheets, thereby increases the electron transfer from electrode to electrolyte and *vice versa*. Furthermore, the incorporated GNR with GS effectively increases the surface area

of GS/GNR, provides more sites for Ni nanoparticles, and quickens the rate of glucose oxidation.

4.7 Conclusions

Novel hybrid material with large electroactive surface area was fabricated via chemical reduction method and functionalized by two approach one by RF N_2/Ar plasma and the other by incorporation Ni Nanoparticles in GS/GNR hybrid material.

Further, GCE/GS/GNR applied as a modified electrodes exhibited remarkable electrocatalytic performance towards AA with increased peak current and less overpotential than GCE/RGO, GCE/GS/CNT and GCE. It also exhibited high sensitivity of 22 nA/μM cm^2 for the electrochemical detection, with the lowest detection concentration of 230 nM.

Next, the same GS/GNR hybrid material on N_2/Ar plasma functionalization was found to be capable of detecting AA, DA and UA simultaneously. The modified electrode shows a well-resolved potential peak separation (ΔE_{AA-DA}= 220 mV, ΔE_{DA-UA}= 152 mV, ΔE_{AA-UA}= 372 mV), strong peak current response, high stability and good recovery in real serum sample analysis along with lowest detection limit.

Finally, the hybrid material of Ni nanoparticles incorporated in GS/GNR, applied to detect glucose, showed remarkably improved electrocatalytic response of glucose and exhibited excellent performances for the amperometric determination of glucose with rapid response, low detection limit, high sensitivity and selectivity, wide linear range and good long-term stability for the oxidation of glucose. These findings would be beneficial to the development of advanced electrode materials for novel electrochemical biosensors.

CHAPTER 6
CONCLUSIONS AND FUTURE PERSPECTIVE

6.1 Conclusions

GS is the interesting class of carbon based electrochemical nanomaterial which attracted scientific community in the recent past because of its intriguing properties such as low-toxicity, biocompatibility, large surface area, wide potential window, cheap and easy synthetic routes and so on. GS and its derivatives have been scrutinized in ample number of applications which include chemical and biosensors, supercapacitor, energy storage and conversion, bioimaging, etc. Although a variety of synthetic routes and technological possibilities of GS have been explored over the years, there are a few issues which need further attention. (i) The pristine GS possesses inertness to reaction, which exhibits poor dispersion in both water and organic solvents and weakens the competitive strength of graphene in the field of sensor (ii) due to van der Waals force GS tends to restack and reduce the surface area. (iii) Due to the structural complexity, the origin of the electrochemical property in GS are not well understood. Our work aims to address a few of the aforementioned issues and also to develop electrochemical biosensors using modified GS having high selectivity towards some biologically important molecules and ions.

Chapter 1 contains introduction and literature review. It gives an overview of the present status of various synthetic routes for GS and GNR, its electrochemical property and its electrochemical based sensor applications. The basics of electrochemistry, mechanisms of electrochemical sensing and general approaches to electrochemical sensing were discussed in this Chapter.

The material and methods, characterization techniques with theoretical background, fabrication of electrodes for electrochemical sensor and various electrochemical techniques are explained in chapter 2.

A DET based highly selective sensing of nitrite is demonstrated in Chapter 3. The GS synthesized by chemical reduction method called reduced graphene oxide (RGO) was functionalized by O_2, N_2 and NH_3 RF plasma. NH_3 plasma functionalized GS with enhanced electrocatalytic with the presence of nitrogen

heteroatom and immobilized with hemoglobin is used for sensing nitrite. The RGO-NH_3 acts as an electrode and immobilized hemoglobin binds to specifically to nitrite. The selectivity of this DET based nitrite sensor was studied by interacting the sensor system with AA, DA, UA and hydrogen peroxide. It was found that there is no significant response of sensor system towards these molecules.

The synthesis of hybridized GS, functionalization of hybridized GS, the electrochemical property and their application as electrochemical biosensor are detailed in Chapter 4. The synthesis was accomplished by introducing GNR with GS *via* chemical co-reduction method. Functionalization of GS/GNR was performed by two different approach: (i) generating nitrogen moieties on the GS/GNR skeleton by N_2/Ar RF plasma. (ii) Introducing Ni nanoparticles into GS/GNR *via* chemical reduction method. The detailed spectroscopic characterization of all the three materials reveals the well dispersed GS and GNR, effective functionalization of graphitic, pyridinic and pyrrolic nitrogen atoms at the core of the GS/GNR and NH_2 group at the surface and successful incorporation of Ni nanoparticles on GS/GNR.

The GS/GNR with increased surface area and enhanced electrical conductivity was utilized for the selective sensing of AA in the presence of other interferents like dopamine, uric acid and citric acid at a minimum potential of (0.08 V), with a detection limit of 230 nM and sensitivity of 22 nA/μMcm^2. N_2/Ar/GS/GNR with enhanced electronegativity provides a reagent less approach to detect AA, UA and DA with large peak separation potential and increased current response. Highly selective and sensitive determination of AA, DA and UA exhibits a detection limit of 5.3 nM, 2.5 nM and 5.7 nM respectively, with high stability, and satisfying recovery results in real serum samples. Ni nanoparticles dispersed uniformly in GS/GNR/Ni hybrid, provides higher specific surface area, enhanced electrical conductivity and more active sites, providing a facile transport pathways for ions and offers unhindered diffusion of OH^- during the electrochemical process. Due to these excellent properties, the hybrid material of GS/GNR/Ni showed remarkably improved electrocatalytic response of glucose with a detection limit of 2.5 nM and good long-term stability for the oxidation of glucose

In Chapter 5, a PGNR was synthesized *via* chemical etching of iron oxide GNR hybrid and electrochemically deposited by AuNPs. The obtained AuNPs/PGNR hybrid was applied to dignose HCC. Microscopic analysis clearly demonstrated the formation of porous structures and with AuNPs deposited on porous GNR. The fabricated electrode was applied to detect AFP, a biomarker to diagnosis HCC. Here porous GNR quicken the rate of electron transfer, whereas AuNPs deposited on the material acts as an immobilization platform for AFP and also enhances the electrocatalytic property. It was observed that AuNPs/PGNR shows high selectivity on AFP with the presence of other interfering biological species.

6.2 Future perspectives

Owing to the better graphitization, enhanced electrocatalytic property and increase in surface area, we propose to functionalize RGO by Ar/NH_3 RF plasma. Pores introduced by Ar plasma functionalization may increase the rate of electron transfer. Moreover, various nitrogen moieties introduced can increase the electronegative property of the material, also it may act as an immobilization platform for biomolecules and can be utilized in biosensing various biomarker.

Although there are several reports on the application of functionalized GS in energy storage, to the best of our knowledge, only few reports are available on dual plasma functionalization i.e with both nitrogen and sulphur. The dual plasma functionalized GS with large surface area and increased the chemical reactivity can be used in electrocatalytic oxygen reduction reaction and in lithium ion battery.

Biological applications of functionalized GS are yet to be explored in its capacity. The non-toxicity of GS make them alternative to traditional heavy metal based material in the field of biotechnology and drug delivery applications. It has the propensity to be modified according to the needs. Controlled functionalization of GS have the potential to become next generation electrochemical sensor, bioimaging agents and energy storage.

REFERENCES

1. Abdolhosseinzadeh, S., Asgharzadeh, H., & Seop Kim, H. (2015). Fast and fully-scalable synthesis of reduced graphene oxide. *Scientific Reports*, *5*, 10160. Retrieved from http://dx.doi.org/10.1038/srep10160

2. Abdullin, I. F., Turova, E. N., Ziyatdinova, G. K., & Budnikov, G. K. (2002). Potentiometric Determination of Ascorbic Acid: Estimation of Its Contribution to the Total Antioxidant Capacity of Plant Materials. *Journal of Analytical Chemistry*, *57*(4), 353–355. http://doi.org/10.1023/A:1014962617407

3. Ahirwal, G. K., & Mitra, C. K. (2010). Gold nanoparticles based sandwich electrochemical immunosensor. *Biosensors and Bioelectronics*, *25*(9), 2016–2020. http://doi.org/http://dx.doi.org/10.1016/j.bios.2010.01.029

4. Alpert, E., Starzl, T. E., Schur, P. H. & Isselbacher, K. J. (1971). Serum-fetoprotein in hepatoma patients after liver transplantation. *Gastroenterology*, *61*(2), 144–148.

5. Ambrosi, A., Chua, C. K., Bonanni, A., & Pumera, M. (2014). Electrochemistry of graphene and related materials. *Chemical Reviews*, *114*(14), 7150–7188. http://doi.org/10.1021/cr500023c

6. Arrigoni, O., & De Tullio, M. C. (2002). Ascorbic acid: much more than just an antioxidant. *Biochimica et Biophysica Acta (BBA) - General Subjects*, *1569*(1), 1–9. http://doi.org/http://dx.doi.org/10.1016/S0304-4165(01)00235-5

7. Artiles, M. S., Rout, C. S., & Fisher, T. S. (2011). Graphene-based hybrid materials and devices for biosensing. *Advanced Drug Delivery Reviews*, *63*(14), 1352–1360. http://doi.org/https://doi.org/10.1016/j.addr.2011.07.005

8. Baccarin, M., Janegitz, B. C., Berté, R., Vicentini, F. C., Banks, C. E., Fatibello-Filho, O., & Zucolotto, V. (2016). Direct electrochemistry of hemoglobin and biosensing for hydrogen peroxide using a film containing silver nanoparticles and poly(amidoamine) dendrimer. *Materials Science and Engineering C*, *58*, 97–102. http://doi.org/10.1016/j.msec.2015.08.013

9. Bard, A. J., & Faulkner, L. R. (2015). *Fundamentals and Fundamentals and Applications*. *Molecular Biology* (Vol. 8). http://doi.org/10.1016/B978-0-08-098353-0.00003-8

10. Becerril, H. A., Mao, J., Liu, Z., Stoltenberg, R. M., Bao, Z., & Chen, Y. (2008). Evaluation of Solution-Processed Reduced Graphene Oxide Films as Transparent Conductors. *ACS Nano*, *2*(3), 463–470.

http://doi.org/10.1021/nn700375n

11. Bianco, G. V, Losurdo, M., Giangregorio, M. M., Capezzuto, P., & Bruno, G. (2015). Chemical functionalization of graphene by plasma processes. *22nd International Symposium on Plasma Chemistry*, (September), 1–2.

12. Binnig, G., & Quate, C. F. (1986). Atomic Force Microscope. *Physical Review Letters*, *56*(9), 930–933. http://doi.org/10.1103/PhysRevLett.56.930

13. Bo, X., Zhou, M., & Guo, L. (2017). Electrochemical sensors and biosensors based on less aggregated graphene. *Biosensors and Bioelectronics*, *89*(Part 1), 167–186. http://doi.org/https://doi.org/10.1016/j.bios.2016.05.002

14. Bragg, W. L. (1929). The diffraction of short electromagnetic Waves by a Crystal. *Scientia*, *23*(45).

15. Brodie, B. C. (1859). On the Atomic Weight of Graphite. *Philosophical Transactions of the Royal Society of London*, *149*, 249–259. Retrieved from http://www.jstor.org/stable/108699

16. Brownson, D. A. C., & Banks, C. E. (2010). Graphene electrochemistry: an overview of potential applications. *Analyst*, *135*(11), 2768–2778. http://doi.org/10.1039/C0AN00590H

17. Brownson, D. A. C., Munro, L. J., Kampouris, D. K., & Banks, C. E. (2011). Electrochemistry of graphene: not such a beneficial electrode material? *RSC Advances*, *1*(6), 978–988. http://doi.org/10.1039/C1RA00393C

18. Brunauer, S., Emmett, P. H., & Teller, E. (1938). Adsorption of Gases in Multimolecular Layers. *Journal of the American Chemical Society*, *60*(2), 309–319. http://doi.org/10.1021/ja01269a023

19. Burany, S. (2003). Scanning Electron Microscopy and X-Ray Microanalysis. J. Goldstein, D. Newbury, D. Joy, C, Lyman, P. Echlin, E. Lifshin, L. Sawyer, and J. Michael. Kluwer Academic, Plenum Publishers, New York; 2003, 688 pages (Hardback, $75.00) ISBN 0-306-47292-9. *Microscopy and Microanalysis*, *9*(5), 484. http://doi.org/DOI: 10.1017/S1431927603030617

20. Campos, L. C., Manfrinato, V. R., Sanchez-Yamagishi, J. D., Kong, J., & Jarillo-Herrero, P. (2009). Anisotropic Etching and Nanoribbon Formation in Single-Layer Graphene. *Nano Letters*, *9*(7), 2600–2604. http://doi.org/10.1021/nl900811r

21. Cano-Márquez, A. G., Rodríguez-Macías, F. J., Campos-Delgado, J., Espinosa-González, C. G., Tristán-López, F., Ramírez-González, D., …

Vega-Cantú, Y. I. (2009). Ex-MWNTs: Graphene sheets and ribbons produced by lithium intercalation and exfoliation of carbon nanotubes. *Nano Letters*, *9*(4), 1527–1533.

22. Chang, L. H., Hsieh, C. K., Hsiao, M. C., Chiang, J. C., Liu, P. I., Ho, K. K., … Tsai, C. H. (2013). A graphene-multi-walled carbon nanotube hybrid supported on fluorinated tin oxide as a counter electrode of dye-sensitized solar cells. *Journal of Power Sources*, *222*, 518–525. http://doi.org/10.1016/j.jpowsour.2012.08.058

23. Chauhan, N., Narang, J., Rawal, R., & Pundir, C. S. (2011). A highly sensitive non-enzymatic ascorbate sensor based on copper nanoparticles bound to multi walled carbon nanotubes and polyaniline composite. *Synthetic Metals*, *161*(21–22), 2427–2433. http://doi.org/http://dx.doi.org/10.1016/j.synthmet.2011.09.020

24. Chen, X., Zhang, G., Shi, L., Pan, S., Liu, W., & Pan, H. (2016). Au / ZnO hybrid nanocatalysts impregnated in N-doped graphene for simultaneous determination of ascorbic acid , acetaminophen and dopamine. *Materials Science & Engineering C*, *65*, 80–89. http://doi.org/10.1016/j.msec.2016.03.106

25. Chen, X., Zhu, J., Xi, Q., & Yang, W. (2012). A high performance electrochemical sensor for acetaminophen based on single-walled carbon nanotube-graphene nanosheet hybrid films. *Sensors and Actuators, B: Chemical*, *161*(1), 648–654. http://doi.org/10.1016/j.snb.2011.10.085

26. Chen, Y., Jin, B., Guo, L.-R., Yang, X.-J., Chen, W., Gu, G., … Xia, X.-H. (2008). Hemoglobin on Phosphonic Acid Terminated Self-Assembled Monolayers at a Gold Electrode: Immobilization, Direct Electrochemistry, and Electrocatalysis. *Chemistry – A European Journal*, *14*(34), 10727–10734. http://doi.org/10.1002/chem.200801503

27. Chen, Z., Lin, Y.-M., Rooks, M. J., & Avouris, P. (2007). Graphene nano-ribbon electronics. *Physica E: Low-Dimensional Systems and Nanostructures*, *40*(2), 228–232. http://doi.org/http://dx.doi.org/10.1016/j.physe.2007.06.020

28. Chen, Z., Ren, W., Gao, L., Liu, B., Pei, S., & Cheng, H.-M. (2011). Three-dimensional flexible and conductive interconnected graphene networks grown by chemical vapour deposition. *Nature Materials*, *10*, 424. Retrieved from http://dx.doi.org/10.1038/nmat3001

29. Choi, T., Kim, S. H., Lee, C. W., Kim, H., Choi, S.-K., Kim, S.-H., … Kim, H. (2015). Synthesis of carbon nanotube–nickel nanocomposites using atomic layer deposition for high-performance non-enzymatic glucose sensing. *Biosensors and Bioelectronics*, *63*, 325–330. http://doi.org/http://dx.doi.org/10.1016/j.bios.2014.07.059

30. Chua, C. K., & Pumera, M. (2014). Chemical reduction of graphene oxide: a synthetic chemistry viewpoint. *Chemical Society Reviews*, *43*(1), 291–312. http://doi.org/10.1039/C3CS60303B

31. Ci, S., Huang, T., Wen, Z., Cui, S., Mao, S., Steeber, D. A., & Chen, J. (2014). Nickel oxide hollow microsphere for non-enzyme glucose detection. *Biosensors and Bioelectronics*, *54*, 251–257. http://doi.org/10.1016/j.bios.2013.11.006

32. Clark, L. C., & Lyons, C. (1962). Electrode systems for continuous monitoring in cardiovascular surgery. *Annals of the New York Academy of Sciences*, *102*(1), 29–45. http://doi.org/10.1111/j.1749-6632.1962.tb13623.x

33. Dar, R. A., Khare, N. G., Cole, D. P., Karna, S. P., & Srivastava, A. K. (2014). Green synthesis of a silver nanoparticle-graphene oxide composite and its application for As(iii) detection. *RSC Advances*, *4*(28), 14432–14440. http://doi.org/10.1039/C4RA00934G

34. Debye, P., & Scherrer, P. (1916). Interference of irregularly oriented particles in x-rays. *Phys. Ziet*, *17*, 277–283.

35. DeKalb, E. L., Kniseley, R. N., & Fassel, V. A. (1966). Optical emission spectroscopy as an analytical tooL*. *Annals of the New York Academy of Sciences*, *137*(1), 235–261. http://doi.org/10.1111/j.1749-6632.1966.tb49756.x

36. Ding, Y., Wang, Y., Li, B., & Lei, Y. (2010). Electrospun hemoglobin microbelts based biosensor for sensitive detection of hydrogen peroxide and nitrite. *Biosensors and Bioelectronics*, *25*(9), 2009–2015. http://doi.org/http://dx.doi.org/10.1016/j.bios.2010.01.024

37. Dutt, V. V. S. E., & Mottola, H. A. (1974). Determination of uric acid at the microgram level by a kinetic procedure based on a pseudo-induction period. *Analytical Chemistry*, *46*(12), 1777–1781. http://doi.org/10.1021/ac60348a041

38. Dutta, S., & Pati, S. K. (2010). Novel properties of graphene nanoribbons: a review. *Journal of Materials Chemistry*, *20*(38), 8207–8223. http://doi.org/10.1039/C0JM00261E

39. Edwards, R. S., & Coleman, K. S. (2013). Graphene synthesis: relationship to applications. *Nanoscale*, *5*(1), 38–51. http://doi.org/10.1039/C2NR32629A

40. Elias, D. C., Nair, R. R., Mohiuddin, T. M. G., Morozov, S. V, Blake, P., Halsall, M. P., … Novoselov, K. S. (2009). Control of Graphene's

Properties by Reversible Hydrogenation: Evidence for Graphane. *Science*, *323*(5914), 610 LP-613. Retrieved from http://science.sciencemag.org/content/323/5914/610.abstract

41. Engelhard, M. H., Droubay, T. C., & Du, Y. (2017). X-Ray Photoelectron Spectroscopy Applications A2 - Lindon, John C. In G. E. Tranter & D. W. B. T.-E. of S. and S. (Third E. Koppenaal (Eds.), (pp. 716–724). Oxford: Academic Press. http://doi.org/https://doi.org/10.1016/B978-0-12-409547-2.12102-X

42. Englert, J. M., Dotzer, C., Yang, G., Schmid, M., Papp, C., Gottfried, J. M., … Hirsch, A. (2011). Covalent bulk functionalization of graphene. *Nature Chemistry*, *3*(4), 279–286. http://doi.org/10.1038/nchem.1010

43. Ensafi, A. A., Ahmadi, N., & Rezaei, B. (2017). Nickel nanoparticles supported on porous silicon flour, application as a non-enzymatic electrochemical glucose sensor. *Sensors and Actuators, B: Chemical*, *239*, 807–815. http://doi.org/10.1016/j.snb.2016.08.088

44. Ensafi, A. A., Ahmadi, Z., Jafari-Asl, M., & Rezaei, B. (2015). Graphene nanosheets functionalized with Nile blue as a stable support for the oxidation of glucose and reduction of oxygen based on redox replacement of Pd-nanoparticles via nickel oxide. *Journal of Electroanalytical Chemistry*, *173*, 619–629. http://doi.org/10.1016/j.electacta.2015.05.109

45. Ensafi, A. A., Zandi-Atashbar, N., Rezaei, B., Ghiaci, M., Chermahini, M. E., & Moshiri, P. (2016). Non-enzymatic glucose electrochemical sensor based on silver nanoparticle decorated organic functionalized multiwall carbon nanotubes. *RSC Adv.*, *6*(65), 60926–60932. http://doi.org/10.1039/C6RA10698F

46. Farajzadeh, M. A., & Nagizadeh, S. (2002). A new simple and accurate turbidimetric method for determination of ascorbic acid in pharmaceuticals and fruits. *Journal of the Chinese Chemical Society*, *49*(5), 949–956.

47. Feng, J. J., Xu, J. J., & Chen, H. Y. (2007). Direct electron transfer and electrocatalysis of hemoglobin adsorbed on mesoporous carbon through layer-by-layer assembly. *Biosensors and Bioelectronics*, *22*(8), 1618–1624. http://doi.org/10.1016/j.bios.2006.07.022

48. Fernández-Merino, M. J., Guardia, L., Paredes, J. I., Villar-Rodil, S., Solís-Fernández, P., Martínez-Alonso, A., & Tascón, J. M. D. (2010). Vitamin C Is an Ideal Substitute for Hydrazine in the Reduction of Graphene Oxide Suspensions. *The Journal of Physical Chemistry C*, *114*(14), 6426–6432. http://doi.org/10.1021/jp100603h

49. Ferrari, A. C., & Basko, D. M. (2013). Raman spectroscopy as a versatile tool for studying the properties of graphene. *Nat Nano*, *8*(4), 235–246.

Retrieved from http://dx.doi.org/10.1038/nnano.2013.46

50. Fleischmann, M., Korinek, K., & Pletcher, D. (1971). The oxidation of organic compounds at a nickel anode in alkaline solution. *Journal of Electroanalytical Chemistry and Interfacial Electrochemistry*, *31*(1), 39–49. http://doi.org/http://dx.doi.org/10.1016/S0022-0728(71)80040-2

51. Foss Jr., C. A., & Martin, C. R. (1994). Chemically Modified Electrodes. *Laboratory Techniques in Electroanalytical Chemistry*, (95).

52. Fu, G., Tao, L., Zhang, M., Chen, Y., Tang, Y., Lin, J., & Lu, T. (2013). One-pot{,} water-based and high-yield synthesis of tetrahedral palladium nanocrystal decorated graphene. *Nanoscale*, *5*(17), 8007–8014. http://doi.org/10.1039/C3NR02179C

53. Fuller, M. P., & Griffiths, P. R. (1978). Diffuse reflectance measurements by infrared Fourier transform spectrometry. *Analytical Chemistry*, *50*(13), 1906–1910. http://doi.org/10.1021/ac50035a045

54. Gao, X., Li, Y., Zhang, Q., Li, S., Chen, Y., & Lee, J.-M. (2015). Polyethyleneimine-assisted synthesis of high-quality platinum/graphene hybrids: the effect of molecular weight on electrochemical properties. *J. Mater. Chem. A*, *3*(22), 12000–12004. http://doi.org/10.1039/C5TA02046H

55. Gao, X., Lu, Y., Liu, M., He, S., & Chen, W. (2015). Sub-nanometer sized Cu6(GSH)3 clusters: one-step synthesis and electrochemical detection of glucose. *Journal of Materials Chemistry C*, *3*(16), 4050–4056. http://doi.org/10.1039/C5TC00246J

56. García-Armada, P., Losada, J., & de Vicente-Pérez, S. (1996). Cation Analysis Scheme by Differential Pulse Polarography. *Journal of Chemical Education*, *73*(6), 544. http://doi.org/10.1021/ed073p544

57. Geim, A. K., & Novoselov, K. S. (2007). The rise of graphene. *Nat Mater*, *6*(3), 183–191. Retrieved from http://dx.doi.org/10.1038/nmat1849

58. Georgakilas, V., Otyepka, M., Bourlinos, A. B., Chandra, V., Kim, N., Kemp, K. C., … Kim, K. S. (2012). Functionalization of Graphene: Covalent and Non-Covalent Approaches, Derivatives and Applications. *Chemical Reviews*, *112*(11), 6156–6214. http://doi.org/10.1021/cr3000412

59. Georgakilas, V., Tiwari, J. N., Kemp, K. C., Perman, J. A., Bourlinos, A. B., Kim, K. S., & Zboril, R. (2016). Noncovalent Functionalization of Graphene and Graphene Oxide for Energy Materials, Biosensing, Catalytic, and Biomedical Applications. *Chemical Reviews*, *116*(9), 5464–5519. http://doi.org/10.1021/acs.chemrev.5b00620

60. George, P., & Hanania, G. (1953). A spectrophotometric study of ionizations in methaemoglobin. *Biochemical Journal*, *55*(2), 236–243. Retrieved from http://www.ncbi.nlm.nih.gov/pmc/articles/PMC1269226/

61. Ghanbari, K., & Hajheidari, N. (2015). ZnO – Cu x O / polypyrrole nanocomposite modified electrode for simultaneous determination of ascorbic acid , dopamine , and uric acid, *473*, 53–62. http://doi.org/10.1016/j.ab.2014.12.013

62. Ghiaci, M., Tghizadeh, M., Ensafi, A. A., Zandi-Atashbar, N., & Rezaei, B. (2015). Silver nanoparticles decorated anchored type ligands as new electrochemical sensors for glucose detection. *Journal of the Taiwan Institute of Chemical Engineers*, *0*, 1–7. http://doi.org/10.1016/j.jtice.2016.03.013

63. Gillespie, J. R., & Uversky, V. N. (2000). Structure and function of α-fetoprotein: a biophysical overview. *Biochimica et Biophysica Acta (BBA) - Protein Structure and Molecular Enzymology*, *1480*(1), 41–56. http://doi.org/http://dx.doi.org/10.1016/S0167-4838(00)00104-7

64. Gokus, T., Nair, R. R., Bonetti, A., Böhmler, M., Lombardo, A., Novoselov, K. S., … Hartschuh, A. (2009). Making Graphene Luminescent by Oxygen Plasma Treatment. *ACS Nano*, *3*(12), 3963–3968. http://doi.org/10.1021/nn9012753

65. Goodmans, L. (1963). Theory and Applications of Ultraviolet Spectroscopy. *Journal of the American Chemical Society*, *85*(24), 4056–4057. http://doi.org/10.1021/ja00907a057

66. Gorton, L., Lindgren, A., Larsson, T., Munteanu, F. D., Ruzgas, T., & Gazaryan, I. (1999). Direct electron transfer between heme-containing enzymes and electrodes as basis for third generation biosensors, *400*, 91–108.

67. Grieshaber, D., MacKenzie, R., Vörös, J., & Reimhult, E. (2008). Electrochemical Biosensors - Sensor Principles and Architectures. *Sensors (Basel, Switzerland)*, *8*(3), 1400–1458. Retrieved from http://www.ncbi.nlm.nih.gov/pmc/articles/PMC3663003/

68. Guo, H.-L., Wang, X.-F., Qian, Q.-Y., Wang, F.-B., & Xia, X.-H. (2009). A Green Approach to the Synthesis of Graphene Nanosheets. *ACS Nano*, *3*(9), 2653–2659. http://doi.org/10.1021/nn900227d

69. Hadi, M., & Rouhollahi, A. (2012). Simultaneous electrochemical sensing of ascorbic acid, dopamine and uric acid at anodized nanocrystalline graphite-like pyrolytic carbon film electrode. *Analytica Chimica Acta*, *721*, 55–60. http://doi.org/http://dx.doi.org/10.1016/j.aca.2012.01.051

70. Hammond, J. L., Formisano, N., Estrela, P., Carrara, S., & Tkac, J. (2016). Electrochemical biosensors and nanobiosensors. *Essays in Biochemistry*, *60*(1), 69–80. http://doi.org/10.1042/EBC20150008

71. Han, D., Han, T., Shan, C., Ivaska, A., & Niu, L. (2010). Simultaneous Determination of Ascorbic Acid, Dopamine and Uric Acid with Chitosan-Graphene Modified Electrode. *Electroanalysis*, *22*(17–18), 2001–2008. http://doi.org/10.1002/elan.201000094

72. Han, M. Y., Özyilmaz, B., Zhang, Y., & Kim, P. (2007). Energy Band-Gap Engineering of Graphene Nanoribbons. *Physical Review Letters*, *98*(20), 206805. Retrieved from https://link.aps.org/doi/10.1103/PhysRevLett.98.206805

73. Hayat, M. A. (1986). Preface BT - Basic Techniques for Transmission Electron Microscopy (pp. xxv–xxvii). Academic Press. http://doi.org/https://doi.org/10.1016/B978-0-12-333926-3.50003-8

74. Heinze, J. (1984). Cyclic Voltammetry—"Electrochemical Spectroscopy". New Analytical Methods (25). *Angewandte Chemie International Edition in English*, *23*(11), 831–847. http://doi.org/10.1002/anie.198408313

75. Higginbotham, A. L., Kosynkin, D. V, Sinitskii, A., Sun, Z., & Tour, J. M. (2010). Lower-defect graphene oxide nanoribbons from multiwalled carbon nanotubes. *ACS Nano*, *4*(4), 2059–2069.

76. Hoa, L. T., Thi, N., Linh, Y., Chung, J. S., & Hur, S. H. (2017). Green synthesis of silver nanoparticle-decorated porous reduced graphene oxide for antibacterial non-enzymatic glucose sensors. *Ionics*, 0–7. http://doi.org/10.1007/s11581-016-1954-0

77. Huang, H., Wei, D., Sun, J., Wong, S. L., Feng, Y. P., Neto, A. H. C., & Wee, A. T. S. (2012). Spatially Resolved Electronic Structures of Atomically Precise Armchair Graphene Nanoribbons. *Scientific Reports*, *2*, 983. http://doi.org/10.1038/srep00983

78. Huang, X., Fan, Z., Lin, C., Jia, L., Lin, B., Wang, J., … Zhuang, N. (2015). High electrochemical properties of graphene nanoribbons-hybridized manganese dioxide as cathode material for lithium battery. *Journal of Nanoparticle Research*, *17*(2), 97. http://doi.org/10.1007/s11051-015-2908-6

79. Hulicova, D., Kodama, M., & Hatori, H. (2006). Electrochemical Performance of Nitrogen-Enriched Carbons in Aqueous and Non-Aqueous Supercapacitors. *Chemistry of Materials*, *18*(9), 2318–2326. http://doi.org/10.1021/cm060146i

80. Hummers, W. S., & Offeman, R. E. (1958). Preparation of Graphitic Oxide. *Journal of the American Chemical Society*, *80*(6), 1339. http://doi.org/10.1021/ja01539a017

81. Hunter, R. J. (1981). Preface BT - Zeta Potential in Colloid Science (pp. v–vi). Academic Press. http://doi.org/https://doi.org/10.1016/B978-0-12-361961-7.50004-3

82. Jiao, L., Wang, X., Diankov, G., Wang, H., & Dai, H. (2011). Facile synthesis of high-quality graphene nanoribbons. *Nature Nanotechnology*, *6*, 132. Retrieved from http://dx.doi.org/10.1038/nnano.2011.2

83. Jiao, L., Zhang, L., Wang, X., Diankov, G., & Dai, H. (2009). Narrow graphene nanoribbons from carbon nanotubes. *Nature*, *458*(7240), 877–880.

84. Jirimali, H. D., Nagarale, R. K., Saravanakumar, D., Lee, J. M., & Shin, W. (2013). Hydroquinone modified chitosan/carbon film electrode for the selective detection of ascorbic acid. *Carbohydrate Polymers*, *92*(1), 641–644. http://doi.org/http://dx.doi.org/10.1016/j.carbpol.2012.09.024

85. Jokar, E., Shahrokhian, S., & zad, A. I. (2014). Electrochemical functionalization of graphene nanosheets with catechol derivatives as an effective method for preparation of highly performance supercapacitors. *Electrochimica Acta*, *147*, 136–142. http://doi.org/http://dx.doi.org/10.1016/j.electacta.2014.09.102

86. Jorio, A., Ferreira, E. H. M., Cançado, L. G., Achete, C. A., & Capaz, R. B. (2009). Measuring Disorder in Graphene with Raman Spectroscopy.

87. Kanchana, W., Sakai, T., Teshima, N., Katoh, S., & Grudpan, K. (2007). Successive determination of urinary protein and glucose using spectrophotometric sequential injection method. *Analytica Chimica Acta*, *604*(2), 139–146. http://doi.org/http://dx.doi.org/10.1016/j.aca.2007.10.010

88. Kang, H., Lee, Y., Lee, K. J., & Jung, B. (2008). Optical polarimetry probe system for glucose concentration monitoring (Vol. 6863, pp. 686307–686309).

89. Karahan, H. A., & Özdoğan, E. (2008). Improvements of surface functionality of cotton fibers by atmospheric plasma treatment. *Fibers and Polymers*, *9*(1), 21–26. http://doi.org/10.1007/s12221-008-0004-6

90. Keeley, G. P., O'Neill, A., McEvoy, N., Peltekis, N., Coleman, J. N., & Duesberg, G. S. (2010). Electrochemical ascorbic acid sensor based on DMF-exfoliated graphene. *Journal of Materials Chemistry*, *20*(36), 7864–7869.

91. Kim, K., Sussman, A., & Zettl, A. (2010). Graphene Nanoribbons Obtained by Electrically Unwrapping Carbon Nanotubes. *ACS Nano*, *4*(3), 1362–1366. http://doi.org/10.1021/nn901782g

92. Ko, C.-Y., Huang, J.-H., Raina, S., & Kang, W. P. (2013). A high performance non-enzymatic glucose sensor based on nickel hydroxide modified nitrogen-incorporated nanodiamonds. *The Analyst*, *138*(11), 3201–8. http://doi.org/10.1039/c3an36679k

93. Kosynkin, D. V, Higginbotham, A. L., Sinitskii, A., Lomeda, J. R., Dimiev, A., Price, B. K., & Tour, J. M. (2009). Longitudinal unzipping of carbon nanotubes to form graphene nanoribbons. *Nature*, *458*(7240), 872–876.

94. Kou, H., Jia, L., Wang, C., & Ye, W. (2012). A Nitrite Biosensor Based on the Direct Electron Transfer of Hemoglobin Immobilized on Carboxyl-Functionalized Multiwalled Carbon Nanotubes/Polyimide Composite. *Electroanalysis*, *24*(9), 1799–1803. http://doi.org/10.1002/elan.201200275

95. Kuang, D., Xu, L., Liu, L., Hu, W., & Wu, Y. (2013). Graphene–nickel composites. *Applied Surface Science*, *273*, 484–490. http://doi.org/http://dx.doi.org/10.1016/j.apsusc.2013.02.066

96. Kuila, T., Bose, S., Mishra, A. K., Khanra, P., Kim, N. H., & Lee, J. H. (2012). Chemical functionalization of graphene and its applications. *Progress in Materials Science*, *57*(7), 1061–1105. http://doi.org/https://doi.org/10.1016/j.pmatsci.2012.03.002

97. Kumar, A., Voevodin, A. A., Paul, R., Altfeder, I., Zemlyanov, D., Zakharov, D. N., & Fisher, T. S. (2013). Nitrogen-doped graphene by microwave plasma chemical vapor deposition. *Thin Solid Films*, *528*, 269–273. http://doi.org/10.1016/j.tsf.2012.07.142

98. Kumar, P., Panchakarla, L. S., & Rao, C. N. R. (2011). Laser-induced unzipping of carbon nanotubes to yield graphene nanoribbons. *Nanoscale*, *3*(5), 2127–2129. http://doi.org/10.1039/C1NR10137D

99. Lang, B. (1975). *A LEED study of the deposition of carbon on platinum crystal surfaces*. *Surface Science - SURFACE SCI* (Vol. 53). http://doi.org/10.1016/0039-6028(75)90132-6

100. Láng, G. (1994). Electrochemical impedance, analysis and interpretation (ASTM STP 1188). Hrsg. J. R. Scully, D. C. Silverman und M. W. Kendig, 480 S., American Society for Testing and Materials, Philadelphia, 1993. Vorträge anläßlich des Symposium am 4./5. 11. 1991 in San. *Materials and Corrosion*, *45*(10), 582. http://doi.org/10.1002/maco.19940451014

101. Lavanya, J., & Gomathi, N. (2015). High-sensitivity ascorbic acid sensor using graphene sheet / graphene nanoribbon hybrid material as an enhanced electrochemical sensing platform *Talanta*, *144*(July), 655–661. http://doi.org/10.1016/j.talanta.2015.07.018

102. Laviron, E. (1974). Adsorption, autoinhibition and autocatalysis in polarography and in linear potential sweep voltammetry. *Journal of Electroanalytical Chemistry and Interfacial Electrochemistry*, *52*(3), 355–393. http://doi.org/http://dx.doi.org/10.1016/S0022-0728(74)80448-1

103. Laviron, E. (1979). General expression of the linear potential sweep voltammogram in the case of diffusionless electrochemical systems. *Journal of Electroanalytical Chemistry and Interfacial Electrochemistry*, *101*(1), 19–28. http://doi.org/http://dx.doi.org/10.1016/S0022-0728(79)80075-3

104. Lee, Y.-H., Lee, Y.-F., Chang, K.-H., & Hu, C.-C. (2011). Synthesis of N-doped carbon nanosheets from collagen for electrochemical energy storage/conversion systems. *Electrochemistry Communications*, *13*(1), 50–53. http://doi.org/http://dx.doi.org/10.1016/j.elecom.2010.11.010

105. Li, C., & Shi, G. (2012). Three-dimensional graphene architectures. *Nanoscale*, *4*(18), 5549–5563. http://doi.org/10.1039/C2NR31467C

106. Li, D., Müller, M. B., Gilje, S., Kaner, R. B., & Wallace, G. G. (2008). Processable Aqueous Dispersions of Graphene Nanosheets. *Nat. Nanotechnol.*, *3*, 101.

107. Li, F., Li, J., Feng, Y., Yang, L., & Du, Z. (2011). Electrochemical behavior of graphene doped carbon paste electrode and its application for sensitive determination of ascorbic acid. *Sensors and Actuators, B: Chemical*, *157*(1), 110–114. http://doi.org/10.1016/j.snb.2011.03.033

108. Li, P., Ding, Y., Lu, Z., Li, Y., Zhu, X., Zhou, Y., … Lu, T. (2013). Direct electrochemistry of hemoglobin immobilized on the water-soluble phosphonate functionalized multi-walled carbon nanotubes and its application to nitric oxide biosensing. *Talanta*, *115*, 228–234. http://doi.org/https://doi.org/10.1016/j.talanta.2013.03.088

109. Li, P., Ding, Y., Wang, A., Zhou, L., Wei, S., Zhou, Y., … Lu, T. (2013). Self-Assembly of Tetrakis (3-Trifluoromethylphenoxy) Phthalocyaninato Cobalt(II) on Multiwalled Carbon Nanotubes and Their Amperometric Sensing Application for Nitrite. *ACS Applied Materials & Interfaces*, *5*(6), 2255–2260. http://doi.org/10.1021/am400152k

110. Li, S.-M., Yang, S.-Y., Wang, Y.-S., Lien, C.-H., Tien, H.-W., Hsiao, S.-T., … Hu, C.-C. (2013). Controllable synthesis of nitrogen-doped graphene and its effect on the simultaneous electrochemical determination of ascorbic

acid, dopamine, and uric acid. *Carbon*, *59*, 418–429. http://doi.org/http://dx.doi.org/10.1016/j.carbon.2013.03.035

111. Lim, J., Yeo, H., Goh, M., Ku, B.-C., Kim, S. G., Lee, H. S., … You, N.-H. (2015). Grafting of Polyimide onto Chemically-Functionalized Graphene Nanosheets for Mechanically-Strong Barrier Membranes. *Chemistry of Materials*, *27*(6), 2040–2047. http://doi.org/10.1021/cm5044254

112. Lin, Y.-C., Lin, C.-Y., & Chiu, P.-W. (2010). Controllable graphene N-doping with ammonia plasma. *Applied Physics Letters*, *96*(13), 133110. http://doi.org/10.1063/1.3368697

113. Liu, C., Alwarappan, S., Chen, Z., Kong, X., & Li, C.-Z. (2010). Membraneless enzymatic biofuel cells based on graphene nanosheets. *Biosensors and Bioelectronics*, *25*(7), 1829–1833. http://doi.org/https://doi.org/10.1016/j.bios.2009.12.012

114. Liu, F., Piao, Y., Choi, K. S., & Seo, T. S. (2012). Fabrication of free-standing graphene composite films as electrochemical biosensors. *Carbon*, *50*(1), 123–133. http://doi.org/10.1016/j.carbon.2011.07.061

115. Liu, H., Duan, C., Yang, C., Chen, X., Shen, W., & Zhu, Z. (2015). A novel nitrite biosensor based on the direct electron transfer hemoglobin immobilized in the WO<inf>3</inf> nanowires with high length-diameter ratio. *Materials Science and Engineering C*, *53*, 43–49. http://doi.org/10.1016/j.msec.2015.04.016

116. Liu, H., Wu, X., Yang, B., Li, Z., Lei, L., & Zhang, X. (2015). Three-Dimensional Porous NiO Nanosheets Vertically Grown on Graphite Disks for Enhanced Performance Non-enzymatic Glucose Sensor. *Electrochimica Acta*, *174*, 745–752. http://doi.org/10.1016/j.electacta.2015.06.062

117. Liu, K., Zhang, J., Yang, G., Wang, C., & Zhu, J.-J. (2010). Direct electrochemistry and electrocatalysis of hemoglobin based on poly(diallyldimethylammonium chloride) functionalized graphene sheets/room temperature ionic liquid composite film. *Electrochemistry Communications*, *12*(3), 402–405. http://doi.org/http://dx.doi.org/ 10.1016/j.elecom.2010.01.004

118. Liu, M., Liu, R., & Chen, W. (2013). Biosensors and Bioelectronics Graphene wrapped Cu 2 O nanocubes : Non-enzymatic electrochemical sensors for the detection of glucose and hydrogen peroxide with enhanced stability. *Biosensors and Bioelectronic*, *45*, 206–212. http://doi.org/10.1016/j.bios.2013.02.010

119. Liu, M., Miao, Y.-E., Zhang, C., Tjiu, W. W., Yang, Z., Peng, H., & Liu, T. (2013). Hierarchical composites of polyaniline-graphene nanoribbons-

carbon nanotubes as electrode materials in all-solid-state supercapacitors. *Nanoscale*, *5*(16), 7312–20. http://doi.org/10.1039/c3nr01442h

120. Liu, T., Luo, Y., Zhu, J., Kong, L., Wang, W., & Tan, L. (2016). Non-enzymatic detection of glucose using poly(azure A)-nickel modified glassy carbon electrode. *Talanta*, *156–157*, 134–140. http://doi.org/10.1016/j.talanta.2016.04.053

121. Liu, X., Niu, W., Li, H., Han, S., Hu, L., & Xu, G. (2008). Glucose biosensor based on gold nanoparticle-catalyzed luminol electrochemiluminescence on a three-dimensional sol–gel network. *Electrochemistry Communications*, *10*(9), 1250–1253. http://doi.org/http://dx.doi.org/10.1016/j.elecom.2008.06.009

122. Liu, Y., Su, Z., Zhang, Y., Chen, L., Gu, T., Huang, S., … Yao, S. (2013). Amperometric determination of ascorbic acid using multiwalled carbon nanotube-thiolated polyaniline composite modified glassy carbon electrode. *Journal of Electroanalytical Chemistry*, *709*(0), 19–25. http://doi.org/http://dx.doi.org/10.1016/j.jelechem.2013.09.027

123. Liu, Y., Teng, H., Hou, H., & You, T. (2009). Nonenzymatic glucose sensor based on renewable electrospun Ni nanoparticle-loaded carbon nanofiber paste electrode. *Biosensors and Bioelectronics*, *24*(11), 3329–3334. http://doi.org/http://dx.doi.org/10.1016/j.bios.2009.04.032

124. Liu, Z., Guo, Y., & Dong, C. (2015). A high performance nonenzymatic electrochemical glucose sensor based on polyvinylpyrrolidone–graphene nanosheets–nickel nanoparticles–chitosan nanocomposite. *Talanta*, *137*, 87–93. http://doi.org/http://dx.doi.org/10.1016/j.talanta.2015.01.037

125. Lu, L.-M., Zhang, L., Qu, F.-L., Lu, H.-X., Zhang, X.-B., Wu, Z.-S., … Yu, R.-Q. (2009). A nano-Ni based ultrasensitive nonenzymatic electrochemical sensor for glucose: Enhancing sensitivity through a nanowire array strategy. *Biosensors and Bioelectronics*, *25*(1), 218–223. http://doi.org/http://dx.doi.org/10.1016/j.bios.2009.06.041

126. Lu, X., Wang, P., Wang, X., & Guo, Y. (2016). Electrodeposition of gold nanoparticles on electrochemically reduced graphene oxide for sensitive hydrazine electrochemical determination in agriculture wastewater. *International Journal of Electrochemical Science*, *11*(6), 5279–5288. http://doi.org/10.20964/2016.06.94

127. Lu, X., Zou, G., & Li, J. (2007). Hemoglobin entrapped within a layered spongy Co3O4 based nanocomposite featuring direct electron transfer and peroxidase activity. *Journal of Materials Chemistry*, *17*(14), 1427–1432. http://doi.org/10.1039/B615467K

128. Luo, J., Jiang, S., Zhang, H., Jiang, J., & Liu, X. (2012). A novel non-enzymatic glucose sensor based on Cu nanoparticle modified graphene sheets electrode. *Analytica Chimica Acta*, *709*, 47–53. http://doi.org/10.1016/j.aca.2011.10.025

129. Lvovich, V. F. (2012). Fundamentals of Electrochemical Impedance Spectroscopy. In *Impedance Spectroscopy* (pp. 1–21). John Wiley & Sons, Inc. http://doi.org/10.1002/9781118164075.ch1

130. Ma, Y., Zhan, G., Ma, M., Wang, X., & Li, C. (2012). Direct electron transfer of hemoglobin in a biocompatible electrochemical system based on zirconium dioxide nanotubes and ionic liquid. *Bioelectrochemistry*, *84*, 6–10. http://doi.org/http://dx.doi.org/10.1016/j.bioelechem.2011.09.003

131. Mani, V., Chen, S. M., & Lou, B. S. (2013). Three dimensional graphene oxide-carbon nanotubes and graphene-carbon nanotubes hybrids. *International Journal of Electrochemical Science*, *8*(10), 11641–11660.

132. Marcano, D. C., Kosynkin, D. V, Berlin, J. M., Sinitskii, A., Sun, Z., Slesarev, A., … Tour, J. M. (2010). Improved synthesis of graphene oxide. *ACS Nano*, *4*(8), 4806–4814.

133. McAllister, M. J., Li, J.-L., Adamson, D. H., Schniepp, H. C., Abdala, A. A., Liu, J., … Aksay, I. A. (2007). Single Sheet Functionalized Graphene by Oxidation and Thermal Expansion of Graphite. *Chemistry of Materials*, *19*(18), 4396–4404. http://doi.org/10.1021/cm0630800

134. Mehrotra, P. (2016). Biosensors and their applications – A review. *Journal of Oral Biology and Craniofacial Research*, *6*(2), 153–159. http://doi.org/10.1016/j.jobcr.2015.12.002

135. Meyer, J. C., Geim, A. K., Katsnelson, M. I., Novoselov, K. S., Booth, T. J., & Roth, S. (2007). The structure of suspended graphene sheets. *Nature*, *446*(7131), 60–63. Retrieved from http://dx.doi.org/10.1038/nature05545

136. Mohandoss, M., Gupta, S. Sen, Nelleri, A., Pradeep, T., & Maliyekkal, S. M. (2017). Solar mediated reduction of graphene oxide. *RSC Adv.*, *7*(2), 957–963. http://doi.org/10.1039/C6RA24696F

137. Morinaga, T., Sakai, M., Wegmannt, T. G., & Tamaoki, T. (1983). Primary structures of human a-fetoprotein and its mRNA (cDNA clones/three-domain structure/molecular evolution). *Biochemistry*, *80*(August), 4604–4608.

138. Ni, Z., Wang, Y., Yu, T., & Shen, Z. (2010). Raman spectroscopy and imaging of graphene. *Nano Research*, *1*(4), 273–291. http://doi.org/10.1007/s12274-008-8036-1

139. Novoselov, K. S., Fal′ko, V. I., Colombo, L., Gellert, P. R., Schwab, M. G., & Kim, K. (2012). A roadmap for graphene. *Nature*, *490*, 192. Retrieved from http://dx.doi.org/10.1038/nature11458

140. Novoselov, K. S., Geim, A. K., Morozov, S. V, Jiang, D., Zhang, Y., Dubonos, S. V, … Firsov, A. A. (2004). Electric Field Effect in Atomically Thin Carbon Films. *Science*, *306*(5696), 666 LP-669. Retrieved from http://science.sciencemag.org/content/306/5696/666.abstract

141. Pacchioni, G. (2017). Graphene nanoribbons: Joining the pieces. *Nature Reviews Materials*, *2*, 17062. Retrieved from http://dx.doi.org/10.1038/natrevmats.2017.62

142. Paredes, J. I., Villar-Rodil, S., Solís-Fernández, P., Martínez-Alonso, A., & Tascón, J. M. D. (2009). Atomic Force and Scanning Tunneling Microscopy Imaging of Graphene Nanosheets Derived from Graphite Oxide. *Langmuir*, *25*(10), 5957–5968. http://doi.org/10.1021/la804216z

143. Park, S., & Ruoff, R. S. (2009). Chemical methods for the production of graphenes. *Nature Nanotechnology*, *4*, 217. Retrieved from http://dx.doi.org/10.1038/nnano.2009.58

144. Pei, S., & Cheng, H.-M. (2012). The reduction of graphene oxide. *Carbon*, *50*(9), 3210–3228. http://doi.org/https://doi.org/10.1016/j.carbon.2011. 11. 010

145. Pei, S., Zhao, J., Du, J., Ren, W., & Cheng, H.-M. (2010). Direct reduction of graphene oxide films into highly conductive and flexible graphene films by hydrohalic acids. *Carbon*, *48*(15), 4466–4474. http://doi.org/https://doi.org/10.1016/j.carbon.2010.08.006

146. Peng, H., Zhang, L., Soeller, C., & Travas-Sejdic, J. (2009). Conducting polymers for electrochemical DNA sensing. *Biomaterials*, *30*(11), 2132–2148. http://doi.org/https://doi.org/10.1016/j.biomaterials.2008.12.065

147. Pourfayaz, F., Khodadadi, A. A., Mortazavi, Y., & Jafari, S. (2010). Plasma Functionalization of MWCNTs in He Followed by NH 3 Treatment and its Application in PMMA Based Nanocomposites, 1001–1009. http://doi.org/10.1002/ppap.201000055

148. Pumera, M. (2009). The Electrochemistry of Carbon Nanotubes: Fundamentals and Applications. *Chemistry – A European Journal*, *15*(20), 4970–4978. http://doi.org/10.1002/chem.200900421

149. Pumera, M. (2013). Electrochemistry of graphene, graphene oxide and other graphenoids: Review. *Electrochemistry Communications*, *36*, 14–18. http://doi.org/10.1016/j.elecom.2013.08.028

150. Pumera, M., Šmíd, B., & Veltruská, K. (n.d.). Influence of Nitric Acid Treatment of Carbon Nanotubes on Their Physico-Chemical Properties. *Journal of Nanoscience and Nanotechnology*. Retrieved from http://www.ingentaconnect.com/content/asp/jnn/2009/00000009/00000004/art00064

151. Punckt, C., Pope, M. A., Liu, Y. M., & Aksay, I. A. (2016). Structure-Dependent Electrochemistry of Reduced Graphene Oxide Monolayers. *Journal of The Electrochemical Society* , *163*(7), H491–H498. Retrieved from http://jes.ecsdl.org/content/163/7/H491.abstract

152. Qi, H., Zhang, C., & Li, X. (2006). Amperometric third-generation hydrogen peroxide biosensor incorporating multiwall carbon nanotubes and hemoglobin. *Sensors and Actuators B: Chemical*, *114*(1), 364–370. http://doi.org/https://doi.org/10.1016/j.snb.2005.06.002

153. Qian, W., Hao, R., Hou, Y., Tian, Y., Shen, C., Gao, H., & Liang, X. (2009). Solvothermal-assisted exfoliation process to produce graphene with high yield and high quality. *Nano Research*, *2*(9), 706–712. http://doi.org/10.1007/s12274-009-9074-z

154. Raman, C. V, & Krishnan, K. S. (1928). A New Type of Secondary Radiation. *Nature*, *121*, 501. Retrieved from http://dx.doi.org/10.1038/121501c0

155. Ramesha, G. K., & Sampath, S. (2009). Electrochemical Reduction of Oriented Graphene Oxide Films: An in Situ Raman Spectroelectrochemical Study. *The Journal of Physical Chemistry C*, *113*(19), 7985–7989. http://doi.org/10.1021/jp811377n

156. Randles, J. E. B. (1947). Kinetics of rapid electrode reactions. *Discussions of the Faraday Society*, *1*(0), 11–19. http://doi.org/10.1039/DF9470100011

157. Reina, A., Jia, X., Ho, J., Nezich, D., Son, H., Bulovic, V., … Kong, J. (2009). Large Area, Few-Layer Graphene Films on Arbitrary Substrates by Chemical Vapor Deposition. *Nano Letters*, *9*(1), 30–35. http://doi.org/10.1021/nl801827v

158. Sahu, B. B., Yin, Y. Y., Tsutsumi, T., Hori, M., & Han, J. G. (2016). The role of plasma chemistry on functional silicon nitride film properties deposited at low-temperature by mixing two frequency. *Physical Chemistry Chemical Physics*, *18*, 13033–13044. http://doi.org/10.1039/C6CP00986G

159. Sato, S., Harada, N., Kondo, D., & Ohfuchi, M. (2010). Graphene - Novel material for nanoelectronics. *Fujitsu Scientific and Technical Journal*, *46*(1), 103–110.

160. Scenev, V. (2014). Electronic properties of graphene and other carbon-based hybrid materials for flexible electronics. Retrieved from http://edoc.hu-berlin.de/docviews/abstract. php?id=41072%5Cnurn:nbn: de:kobv:11-100221977

161. Segal, M. (2009). Selling graphene by the ton. *Nature Nanotechnology*, *4*(10), 612–614. http://doi.org/10.1038/nnano.2009.279

162. Shamsipur, M., Karimi, Z., Amouzadeh Tabrizi, M., & Rostamnia, S. (2017). Highly sensitive non-enzymatic electrochemical glucose sensor by Nafion/SBA-15-Cu (II) modified glassy carbon electrode. *Journal of Electroanalytical Chemistry*, *799*(Ii), 406–412. http://doi.org/10.1016/ j.jelechem.2017.06.029

163. Shan, C., Yang, H., Han, D., Zhang, Q., Ivaska, A., & Niu, L. (2009). Water-Soluble Graphene Covalently Functionalized by Biocompatible Poly-l-lysine. *Langmuir*, *25*(20), 12030–12033. http://doi.org/10.1021/la903265p

164. Shao, Y., Zhang, S., Engelhard, M. H., Li, G., Shao, G., Wang, Y., … Lin, Y. (2010). Nitrogen-doped graphene and its electrochemical applications. *Journal of Materials Chemistry*, *20*(35), 7491–7496. http://doi.org/10. 1039/C0JM00782J

165. Sharmila, T. K. B., Antony, J. V, Jayakrishnan, M. P., Beegum, P. M. S., & Thomas, E. (2016). Mechanical , thermal and dielectric properties of hybrid composites of epoxy and reduced graphene oxide / iron oxide. *JMADE*, *90*, 66–75. http://doi.org/10.1016/j.matdes.2015.10.055

166. Shen, Z., Gao, W., Li, P., Wang, X., Zheng, Q., Wu, H., … Ding, K. (2016). Highly sensitive nonenzymatic glucose sensor based on nickel nanoparticle-attapulgite-reduced graphene oxide-modified glassy carbon electrode. *Talanta*, *159*, 194–199. http://doi.org/10.1016/j.talanta.2016.06.016

167. Sheng, Z.-H., Shao, L., Chen, J.-J., Bao, W.-J., Wang, F.-B., & Xia, X.-H. (2011). Catalyst-Free Synthesis of Nitrogen-Doped Graphene via Thermal Annealing Graphite Oxide with Melamine and Its Excellent Electrocatalysis. *ACS Nano*, *5*(6), 4350–4358. http://doi.org/10. 1021/nn103584t

168. Sheng, Z.-H., Zheng, X.-Q., Xu, J.-Y., Bao, W.-J., Wang, F.-B., & Xia, X.-H. (2012). Electrochemical sensor based on nitrogen doped graphene: Simultaneous determination of ascorbic acid, dopamine and uric acid. *Biosensors and Bioelectronics*, *34*(1), 125–131. http://doi.org/http://dx.doi. org/10.1016/j.bios.2012.01.030

169. Shin, H.-J., Kim, K. K., Benayad, A., Yoon, S.-M., Park, H. K., Jung, I.-S., … Lee, Y. H. (2009). Efficient Reduction of Graphite Oxide by Sodium

Borohydride and Its Effect on Electrical Conductance. *Advanced Functional Materials*, *19*(12), 1987–1992. http://doi.org/10.1002/adfm.200900167

170. Shinde, D. B., Debgupta, J., Kushwaha, A., Aslam, M., & Pillai, V. K. (2011). Electrochemical Unzipping of Multi-walled Carbon Nanotubes for Facile Synthesis of High-Quality Graphene Nanoribbons. *Journal of the American Chemical Society*, *133*(12), 4168–4171. http://doi.org/10.1021/ja1101739

171. Si, P., Huang, Y., Wang, T., & Ma, J. (2013). Nanomaterials for electrochemical non-enzymatic glucose biosensors. *RSC Adv.*, *3*(11), 3487–3502. http://doi.org/10.1039/C2RA22360K

172. Singh, J., Khanra, P., Kuila, T., Srivastava, M., Das, A. K., Kim, N. H., … Lee, J. H. (2013). Preparation of sulfonated poly(ether–ether–ketone) functionalized ternary graphene/AuNPs/chitosan nanocomposite for efficient glucose biosensor. *Process Biochemistry*, *48*(11), 1724–1735. http://doi.org/http://dx.doi.org/10.1016/j.procbio.2013.07.025

173. Sivasakthi, P., Ramesh Bapu, G. N. K., & Chandrasekaran, M. (2016). Pulse electrodeposited nickel-indium tin oxide nanocomposite as an electrocatalyst for non-enzymatic glucose sensing. *Materials Science and Engineering: C*, *58*, 782–789. http://doi.org/http://dx.doi.org/10.1016/j.msec.2015.09.036

174. Song, S., Sun, L., Yuan, L., Sun, T., Zhao, Y., Zuo, W., … Wang, J. (2008). Method to determine enantiomeric excess of glucose by nonchiral high-performance liquid chromatography using circular dichroism detection. *Journal of Chromatography A*, *1179*(2), 125–130. http://doi.org/http://dx.doi.org/10.1016/j.chroma.2007.11.092

175. Song, S., Wang, L., Li, J., Zhao, J., & Fan, C. (2008). Aptamer-based biosensors, *27*(2). http://doi.org/10.1016/j.trac.2007.12.004

176. Sprinkle, M., Ruan, M., Hu, Y., Hankinson, J., Rubio-Roy, M., Zhang, B., … de Heer, W. A. (2010). Scalable templated growth of graphene nanoribbons on SiC. *Nature Nanotechnology*, *5*, 727. Retrieved from http://dx.doi.org/10.1038/nnano.2010.192

177. Stankovich, S., Dikin, D. A., Piner, R. D., Kohlhaas, K. A., Kleinhammes, A., Jia, Y., … Ruoff, R. S. (2007). Synthesis of graphene-based nanosheets via chemical reduction of exfoliated graphite oxide. *Carbon*, *45*(7), 1558–1565. http://doi.org/https://doi.org/10.1016/j.carbon.2007.02.034

178. Staudenmaier, L. (1898). Verfahren zur Darstellung der Graphitsäure. *Berichte Der Deutschen Chemischen Gesellschaft*, *31*(2), 1481–1487.

http://doi.org/10.1002/cber.18980310237

179. Štefanová, I., Hořejší, V., Krištofová, H., Angelisová, P., Žižkovský, V., & Hilgert, I. (1988). Monoclonal antibodies against human α-fetoprotein exploitation of an unusual calcium-dependent interaction with the antigen for analytical and preparative purposes. *Journal of Immunological Methods*, *111*(1), 67–73. http://doi.org/http://dx.doi.org/10.1016/0022-1759(88)90060-9

180. Stojek, Z. (2010). The electrical double layer and its structure. *Electroanalytical Methods: Guide to Experiments and Applications*, 3–8. http://doi.org/10.1007/978-3-642-02915-8_1

181. Stoller, M. D., Park, S., Zhu, Y., An, J., & Ruoff, R. S. (2008). Graphene-Based Ultracapacitors. *Nano Letters*, *8*(10), 3498–3502. http://doi.org/10.1021/nl802558y

182. Sun, C.-L., Lee, H.-H., Yang, J.-M., & Wu, C.-C. (2011). The simultaneous electrochemical detection of ascorbic acid, dopamine, and uric acid using graphene/size-selected Pt nanocomposites. *Biosensors and Bioelectronics*, *26*(8), 3450–3455.

183. Sun, J., Li, L., Zhang, X., Liu, D., Lv, S., Zhu, D., … You, T. (2015). Simultaneous determination of ascorbic acid{,} dopamine and uric acid at a nitrogen-doped carbon nanofiber modified electrode. *RSC Adv.*, *5*(16), 11925–11932. http://doi.org/10.1039/C4RA13857K

184. Sun, W., Cao, L., Deng, Y., Gong, S., Shi, F., Li, G., & Sun, Z. (2013). Direct electrochemistry with enhanced electrocatalytic activity of hemoglobin in hybrid modified electrodes composed of graphene and multi-walled carbon nanotubes. *Analytica Chimica Acta*, *781*(Supplement C), 41–47. http://doi.org/https://doi.org/10.1016/j.aca.2013.04.010

185. Sun, W., Dong, L., Deng, Y., Yu, J., Wang, W., & Zhu, Q. (2014). Application of N-doped graphene modi fi ed carbon ionic liquid electrode for direct electrochemistry of hemoglobin. *Materials Science & Engineering C*, *39*, 86–91. http://doi.org/10.1016/j.msec.2014.02.029

186. Sun, W., Gong, S., Shi, F., Cao, L., Ling, L., Zheng, W., & Wang, W. (2014). Direct electrochemistry and electrocatalysis of hemoglobin in graphene oxide and ionic liquid composite film. *Materials Science and Engineering C*, *40*, 235–241. http://doi.org/10.1016/j.msec.2014.03.035

187. Sun, W., Guo, Y., Ju, X., Zhang, Y., Wang, X., & Sun, Z. (2013). Direct electrochemistry of hemoglobin on graphene and titanium dioxide nanorods composite modified electrode and itselectrocatalysis. *Biosensors and Bioelectronics*, *42*, 207–213. http://doi.org/http://dx.doi.org /10.1016/j.bio

s.2012.10.034

188. Talyzin, A. V, Luzan, S., Anoshkin, I. V, Nasibulin, A. G., Jiang, H., Kauppinen, E. I., … Noréus, D. (2011). Hydrogenation, Purification, and Unzipping of Carbon Nanotubes by Reaction with Molecular Hydrogen: Road to Graphane Nanoribbons. *ACS Nano*, *5*(6), 5132–5140. http://doi.org/10.1021/nn201224k

189. Tejeda, A. C. and M. N. N. and A. T.-I. and E. H. C. and C. B. and W. A. de H. and A. (2016). Graphene nanoribbons: fabrication, properties and devices. *Journal of Physics D: Applied Physics*, *49*(14), 143001. Retrieved from http://stacks.iop.org/0022-3727/49/i=14/a=143001

190. Thévenot, D. R., Toth, K., Durst, R. A., & Wilson, G. S. (2001). Electrochemical biosensors: recommended definitions and classification1International Union of Pure and Applied Chemistry: Physical Chemistry Division, Commission I.7 (Biophysical Chemistry); Analytical Chemistry Division, Commission V.5 (Electroanalytical. *Biosensors and Bioelectronics*, *16*(1), 121–131. http://doi.org/https://doi.org/10.1016/S0956-5663(01)00115-4

191. Toghill, K. E., Xiao, L., Phillips, M. A., & Compton, R. G. (2010). The non-enzymatic determination of glucose using an electrolytically fabricated nickel microparticle modified boron-doped diamond electrode or nickel foil electrode. *Sensors and Actuators B: Chemical*, *147*(2), 642–652. http://doi.org/http://dx.doi.org/10.1016/j.snb.2010.03.091

192. Tomasi, T. B. (1977). Structure and Function of Alpha-Fetoprotein. *Annual Review of Medicine*, *28*(1), 453–465. http://doi.org/10.1146/annurev.me.28.020177.002321

193. Toral, M. I., Lara, N., Richter, P., Tassara, A., Tapia, A. E., & Rodriguez, C. (2001). Simultaneous determination of ascorbic acid and acetylsalicylic acid in pharmaceutical formulations. *Journal of AOAC International*, *84*(1), 37–42.

194. Tung, V. C., Chen, L. M., Allen, M. J., Wassei, J. K., Nelson, K., Kaner, R. B., & Yang, Y. (2009). Low-Temperature Solution Processing of Graphene-Carbon Nanotube Hybrid Materials for High-Performance Transparent Conductors. *Nano Lett.*, *9*(5), 2513. http://doi.org/10.1021/nl9001525

195. Wallace, P. R. (1947). The Band Theory of Graphite. *Physical Review*, *71*(9), 622–634. Retrieved from https://link.aps.org/doi/10.1103/PhysRev.71.622

196. Walton, S. G., Foley, B. M., Hernández, S. C., Boris, D. R., Baraket, M., Duda, J. C., … Hopkins, P. E. (2017). Plasma-based chemical

functionalization of graphene to control the thermal transport at graphene-metal interfaces. *Surface and Coatings Technology*, *314*(Supplement C), 148–154. http://doi.org/https://doi.org/10.1016/j.surfcoat.2016.12.085

197. Wang, B., Li, S., Liu, J., & Yu, M. (2014). Preparation of nickel nanoparticle/graphene composites for non-enzymatic electrochemical glucose biosensor applications. *Materials Research Bulletin*, *49*, 521–524. http://doi.org/http://dx.doi.org/10.1016/j.materresbull.2013.08.066

198. Wang, C., Du, J., Wang, H., Zou, C., Jiang, F., Yang, P., & Du, Y. (2014). A facile electrochemical sensor based on reduced graphene oxide and Au nanoplates modified glassy carbon electrode for simultaneous detection of ascorbic acid, dopamine and uric acid. *Sensors and Actuators B: Chemical*, *204*, 302–309. http://doi.org/10.1016/j.snb.2014.07.077

199. Wang, C., Xu, P., & Zhuo, K. (2014). Ionic Liquid Functionalized Graphene-Based Electrochemical Biosensor for Simultaneous Determination of Dopamine and Uric Acid in the Presence of Ascorbic Acid. *Electroanalysis*, *26*(1), 191–198. http://doi.org/10.1002/elan.201300345

200. Wang, C., Zhou, Y., He, L., Ng, T.-W., Hong, G., Wu, Q.-H., … Zhang, W. (2013). In situ nitrogen-doped graphene grown from polydimethylsiloxane by plasma enhanced chemical vapor deposition. *Nanoscale*, *5*(2), 600–605. http://doi.org/10.1039/C2NR32897F

201. Wang, G., He, X., Wang, L., Gu, A., Huang, Y., Fang, B., … Zhang, X. (2013). Non-enzymatic electrochemical sensing of glucose. *Microchimica Acta*, *180*(3), 161–186. http://doi.org/10.1007/s00604-012-0923-1

202. Wang, H., Kakade, B. A., Tamaki, T., & Yamaguchi, T. (2014). Synthesis of 3D graphite oxide-exfoliated carbon nanotube carbon composite and its application as catalyst support for fuel cells. *Journal of Power Sources*, *260*, 338–348. http://doi.org/10.1016/j.jpowsour.2014.03.014

203. Wang, J., Bao, W., & Zhang, L. (2012). A nonenzymatic glucose sensing platform based on Ni nanowire modified electrode. *Anal. Methods*, *4*(12), 4009–4013. http://doi.org/10.1039/C2AY25759A

204. Wang, J., Chen, G., & Chatrathi, M. P. (2004). Nickel Amperometric Detector Prepared by Electroless Deposition for Microchip Electrophoretic Measurement of Alcohols and Sugars. *Electroanalysis*, *16*(19), 1603–1608. http://doi.org/10.1002/elan.200302996

205. Wang, R., Xu, C., Sun, J., Gao, L., Jin, J., & Lin, C. (2013). Controllable synthesis of nano-LiFePO4 on graphene using Fe2O3 precursor for high performance lithium ion batteries. *Materials Letters*, *112*(Supplement C),

207–210. http://doi.org/https://doi.org/10.1016/j.matlet.2013.09.037

206. Wang, S.-F., Chen, T., Zhang, Z.-L., Shen, X.-C., Lu, Z.-X., Pang, D.-W., & Wong, K.-Y. (2005). Direct Electrochemistry and Electrocatalysis of Heme Proteins Entrapped in Agarose Hydrogel Films in Room-Temperature Ionic Liquids. *Langmuir*, *21*(20), 9260–9266. http://doi.org/10.1021/la050947k

207. Wang, W., Ruiz, I., Guo, S., Favors, Z., Bay, H. H., Ozkan, M., & Ozkan, C. S. (2014). Hybrid carbon nanotube and graphene nanostructures for lithium ion battery anodes. *Nano Energy*, *3*, 113–118. http://doi.org/10.1016/j.nanoen.2013.10.005

208. Wang, X., Tabakman, S. M., & Dai, H. (2008). Atomic Layer Deposition of Metal Oxides on Pristine and Functionalized Graphene. *Journal of the American Chemical Society*, *130*(26), 8152–8153. http://doi.org/10.1021/ja8023059

209. Wang, X., Wu, M., Tang, W., Zhu, Y., Wang, L., Wang, Q., … Fang, Y. (2013). Simultaneous electrochemical determination of ascorbic acid, dopamine and uric acid using a palladium nanoparticle/graphene/chitosan modified electrode. *Journal of Electroanalytical Chemistry*, *695*, 10–16. http://doi.org/http://dx.doi.org/10.1016/j.jelechem.2013.02.021

210. Wang, X., Zhi, L., & Müllen, K. (2008). Transparent, Conductive Graphene Electrodes for Dye-Sensitized Solar Cells. *Nano Letters*, *8*(1), 323–327. http://doi.org/10.1021/nl072838r

211. Wei, D., Liu, Y., Wang, Y., Zhang, H., Huang, L., & Yu, G. (2009). Synthesis of N-Doped Graphene by Chemical Vapor Deposition and Its Electrical Properties. *Nano Letters*, *9*(5), 1752–1758. http://doi.org/10.1021/nl803279t

212. Weng, Y.-C., & Hsiao, Y.-L. (2011). Comparison of Pt and Ni foil electrodes for amperometric sensing of ascorbic acid. *Journal of Electroanalytical Chemistry*, *651*(2), 160–165. http://doi.org/http://dx.doi.org/10.1016/j.jelechem.2010.11.031

213. Wightman, R. M., Amatorh, C., Engstrom, R. C., Hale, P. D., Kristensen, E. W., Kuhr, W. G., & May, L. J. (1988). Real-time characterization of dopamine overflow and uptake in the rat striatum. *Neuroscience*, *25*(2), 513–523. http://doi.org/http://dx.doi.org/10.1016/0306-4522(88)90255-2

214. Wild, S., Roglic, G., Green, A., Sicree, R., & King, H. (2004). Global Prevalence of Diabetes: Estimates for the year 2000 and projections for 2030 . *Diabetes Care* , *27*(5), 1047–1053. http://doi.org/10.2337/diacare.27.5.1047

215. Wilson, N. R., Pandey, P. A., Beanland, R., Young, R. J., Kinloch, I. A., Gong, L., … York, S. J. (2009). Graphene oxide: structural analysis and application as a highly transparent support for electron microscopy. *ACS Nano*, *3*(9), 2547–2556.

216. Wu, G., Wu, Y., Liu, X., Rong, M., Chen, X., & Chen, X. (2012). An electrochemical ascorbic acid sensor based on palladium nanoparticles supported on graphene oxide. *Analytica Chimica Acta*, *745*, 33–37.

217. Xiao, C., Chu, X., Yang, Y., Li, X., Zhang, X., & Chen, J. (2011). Biosensors and Bioelectronics Hollow nitrogen-doped carbon microspheres pyrolyzed from self-polymerized dopamine and its application in simultaneous electrochemical determination of uric acid , ascorbic acid and dopamine. *Biosensors and Bioelectronics*, *26*(6), 2934–2939. http://doi.org/10.1016/j.bios.2010.11.041

218. Xiao, X., Michael, J. R., Beechem, T., McDonald, A., Rodriguez, M., Brumbach, M. T., … Polsky, R. (2012). Three dimensional nickel-graphene core-shell electrodes. *J. Mater. Chem.*, *22*(45), 23749–23754. http://doi.org/10.1039/C2JM35506J

219. Xu, C., Shi, X., Ji, A., Shi, L., Zhou, C., & Cui, Y. (2015). Fabrication and Characteristics of Reduced Graphene Oxide Produced with Different Green Reductants. *PLoS ONE*, *10*(12), e0144842. http://doi.org/10.1371/journal.pone.0144842

220. Xu, C., Wang, X., & Zhu, J. (2008). Graphene−Metal Particle Nanocomposites. *The Journal of Physical Chemistry C*, *112*(50), 19841–19845. http://doi.org/10.1021/jp807989b

221. Xu, C., Yuan, R., & Wang, X. (2014). Selective reduction of graphene oxide. *Carbon*, *71*(Supplement C), 345. http://doi.org/https://doi.org/10.1016/j.carbon.2014.01.048

222. Yang, B., Wang, H., Du, J., Fu, Y., Yang, P., & Du, Y. (2014). Direct electrodeposition of reduced graphene oxide on carbon fiber electrode for simultaneous determination of ascorbic acid, dopamine and uric acid. *Colloids and Surfaces A: Physicochemical and Engineering Aspects*, *456*, 146–152. http://doi.org/10.1016/j.colsurfa.2014.05.029

223. Yen, M.-Y., Hsiao, M.-C., Liao, S.-H., Liu, P.-I., Tsai, H.-M., Ma, C.-C. M., … Ger, M.-D. (2011). Preparation of graphene/multi-walled carbon nanotube hybrid and its use as photoanodes of dye-sensitized solar cells. *Carbon*, *49*(11), 3597–3606.

224. Yoo, E., Okata, T., Akita, T., Kohyama, M., Nakamura, J., & Honma, I. (2009). Enhanced Electrocatalytic Activity of Pt Subnanoclusters on Graphene Nanosheet Surface. *Nano Letters*, *9*(6), 2255–2259.

http://doi.org/10.1021/nl900397t

225. Yu, C., Wang, Y., Wang, L., Zhu, Z., Bao, N., & Gu, H. (2013). Nanostructured biosensors built with layer-by-layer electrostatic assembly of hemoglobin and Fe3O4@Pt nanoparticles. *Colloids and Surfaces B: Biointerfaces*, *103*(Supplement C), 231–237. http://doi.org/https://doi.org/10.1016/j.colsurfb.2012.10.005

226. Yu, D., & Dai, L. (2009). Self-Assembled Graphene/Carbon Nanotube Hybrid Films for Supercapacitors. *The Journal of Physical Chemistry Letters*, *1*(2), 467–470. http://doi.org/10.1021/jz9003137

227. Zhang, H., Bo, X., & Guo, L. (2015). Sensors and Actuators B : Chemical Electrochemical preparation of porous graphene and its electrochemical application in the simultaneous determination of hydroquinone , catechol , and resorcinol. *Sensors & Actuators: B. Chemical*, *220*, 919–926. http://doi.org/10.1016/j.snb.2015.06.035

228. Zhang, H., Fan, L., & Yang, S. (2006). Significantly Accelerated Direct Electron-Transfer Kinetics of Hemoglobin in a C60-MWCNT Nanocomposite Film. *Chemistry – A European Journal*, *12*(27), 7161–7166. http://doi.org/10.1002/chem.200600055

229. Zhang, S., Tang, S., Lei, J., Dong, H., & Ju, H. (2011). Functionalization of graphene nanoribbons with porphyrin for electrocatalysis and amperometric biosensing. *Journal of Electroanalytical Chemistry*, *656*(1), 285–288. http://doi.org/https://doi.org/10.1016/j.jelechem.2010.10.005

230. Zhang, X., Ma, L., & Zhang, Y. (2015). Electrochimica Acta Electrodeposition of platinum nanosheets on C 60 decorated glassy carbon electrode as a stable electrochemical biosensor for simultaneous detection of ascorbic acid , dopamine and uric acid, *177*, 118–127.

231. Zhang, Y., Xu, F., Sun, Y., Shi, Y., Wen, Z., & Li, Z. (2011). Assembly of Ni(OH)2 nanoplates on reduced graphene oxide: a two dimensional nanocomposite for enzyme-free glucose sensing. *Journal of Materials Chemistry*, *21*(42), 16949. http://doi.org/10.1039/c1jm11641j

232. Zhang, Y., Yan, R., Zhao, F., & Zeng, B. (2009). Polyvinyl alcohol–ionic liquid composition for promoting the direct electron transfer and electrocatalysis of hemoglobin. *Colloids and Surfaces B: Biointerfaces*, *71*(2), 288–292. http://doi.org/http://dx.doi.org/10.1016/j.colsurfb.2009.03.001

233. Zhao, J., Pei, S., Ren, W., Gao, L., & Cheng, H.-M. (2010). Efficient Preparation of Large-Area Graphene Oxide Sheets for Transparent Conductive Films. *ACS Nano*, *4*(9), 5245–5252.

http://doi.org/10.1021/nn1015506

234. Zhao, M. Q., Zhang, Q., Huang, J. Q., Tian, G. L., Chen, T. C., Qian, W. Z., & Wei, F. (2013). Towards high purity graphene/single-walled carbon nanotube hybrids with improved electrochemical capacitive performance. *Carbon*, *54*, 403–411. http://doi.org/10.1016/j.carbon.2012.11.055

235. Zheng, X., Peng, Y., Yang, Y., Chen, J., Tian, H., Cui, X., & Zheng, W. (2017). Hydrothermal reduction of graphene oxide; effect on surface-enhanced Raman scattering. *Journal of Raman Spectroscopy*, *48*(1), 97–103. http://doi.org/10.1002/jrs.4998

236. Zhou, M., Wang, Y., Zhai, Y., Zhai, J., Ren, W., Wang, F., & Dong, S. (2009). Controlled Synthesis of Large-Area and Patterned Electrochemically Reduced Graphene Oxide Films. *Chemistry – A European Journal*, *15*(25), 6116–6120. http://doi.org/10.1002/chem.200900596

237. Zhou, M., Zhai, Y., & Dong, S. (2009). Electrochemical Sensing and Biosensing Platform Based on Chemically Reduced Graphene Oxide. *Analytical Chemistry*, *81*(14), 5603–5613. http://doi.org/10.1021/ac900136z

238. Zhou, X.-H., Liu, L.-H., Bai, X., & Shi, H.-C. (2013). A reduced graphene oxide based biosensor for high-sensitive detection of phenols in water samples. *Sensors and Actuators B: Chemical*, *181*(Supplement C), 661–667. http://doi.org/https://doi.org/10.1016/j.snb.2013.02.021

239. Zhu, J., Jiang, J., Liu, J., Ding, R., Li, Y., Ding, H., … Huang, X. (2011). CNT-network modified Ni nanostructured arrays for high performance non-enzymatic glucose sensors. *RSC Advances*, *1*(6), 1020. http://doi.org/10.1039/c1ra00280e

240. Zhu, Z., Qu, L., Li, X., Zeng, Y., Sun, W., & Huang, X. (2010). Direct electrochemistry and electrocatalysis of hemoglobin with carbon nanotube-ionic liquid-chitosan composite materials modified carbon ionic liquid electrode. *Electrochimica Acta*, *55*(20), 5959–5965. http://doi.org/http://dx.doi.org/10.1016/j.electacta.2010.05.050

241. Zuo, X., Zhang, H., & Li, N. (2012). An electrochemical biosensor for determination of ascorbic acid by cobalt (II) phthalocyanine–multi-walled carbon nanotubes modified glassy carbon electrode. *Sensors and Actuators B: Chemical*, *161*(1), 1074–1079.

LIST OF PUBLICATIONS BASED ON THE THESIS

International Journals

1. Lavanya J, Gomathi N. and Neogi, S (2014). Electrochemical performance of nitrogen and oxygen radio-frequency plasma induced functional groups on tri-layered reduced graphene oxide. *Materials Research Express*, *1*(2), 25604.
2. Lavanya J and Gomathi,N (2015). High-sensitivity ascorbic acid sensor using graphene sheet/graphene nanoribbon hybrid material as an enhanced electrochemical sensing platform. *Talanta*, *144*, 655–661.
3. Lavanya J, Subbiah A, Neogi S and Gomathi, N (2018). Direct electron transfer of hemoglobin at nitrogen incorporated reduced graphene oxide obtained by radio frequency ammonia plasma treatment. *Sensors and Actuators B: Chemical*, *255*, 536–543.
4. Lavanya J, Nithyaa N, Saravana Kumar J and Gomathi N (2018). Ultrasensitive and selective non-enzymatic electrochemical glucose sensor based on hybrid material of graphene nanosheets/graphene nanoribbons/nickel nanoparticle. *Materials Research Bulletin*, *98*, 300–307.
5. Lavanya J, Saravana Kumar J, Neogi. S, and Gomathi, N (2018). Simultaneous determination of ascorbic acid, dopamine and uric acid by a novel electrochemical sensor based on N_2/ Ar RF plasma assisted graphene nanosheet/graphene nanoribbon. *Biosensors and Bioelectronics 105, 236-242.*
6. Lavanya J, Saravana Kumar J, and Gomathi, N. Electrochemical immunosensor for detection of alpha fetoprotein based on electrodeposited Au/ porous graphene ribbon hybrid material. (*To be communicated*).

Conference Proceedings

1. Gayathry S, Thomas A. A, Lavanya J, Gomathi N, Joseph, K, Neogi S, and Nair, C. P. R (2016). Effect of carbon nanotubes on mechanical, electrical and thermal properties of plasma-modified multi-walled carbon nanotubes/polyimide nanocomposites. *AIP Conference Proceedings*, *1724*(1), 20037.
2. Lavanya J and Gomathi N (2016). Synthesis and characterization of nickel oxide/graphene sheet/graphene ribbon composite. *AIP Conference Proceedings*, *1724*(1), 20050.

Book Chapters

1. Yogesh, S. C, Lavanya, J and Gomathi, N (2017) Electrochemical Characterization, Spectroscopic Methods for Nanomaterials Characterization Volume 2 Edited by Sabu Thomas, Raju Thomas, Ajesh K Zachariah, Raghvendra Kumar Mishra Elsevier Pub
2. Lavanya J and Gomathi N. Plasma modified polymeric materials for biosensors/ biodevice applications for Non-thermal plasma technology for polymeric materials: applications in composites, nanostructured materials

and bio-medical fields edited by Sabu Thomos. Miran Mozetic, Uros Cvelbar, Petr Špatenka, CSc, Praveen K.M *(under production)*

CONFERENCES/SEMINARS

Oral Presentations

1. Lavanya J, Neogi S and Gomathi N 'Comparative study on Electrocatalytic activity of oxygen and nitrogen doped graphene for Electrochemical cancer biosensor' *International Conference on Stem Cells and Cancer (ICSCC-2013) International Centre for Stem Cells, Cancer and Biotechnology (ICSCCB), Pune, India 19-22, October 2013.*
2. Lavanya J, Neogi S and Gomathi N 'Electrochemical Characterization of Ammonia Radio Frequency Plasma Treated Reduced Graphene Oxide in Melamine Sensing' *29th National Symposium on Plasma Science & Technology and the International Conference on Plasma & Nanotechnology, Mahatma Gandhi University, Kottayam, Kerala, India. 8-11 December, 2014.*
3. Lavanya J, Neogi S and Gomathi N 'Enhanced Electrocatalytic Activity Of Ammonia Radio Frequency Plasma Modified Reduced Graphene Oxide, *NANO-2015, KSR engineering college Thirugengode, Tamilnadu 7-10 Dec 2015.*

Poster Presentations

1. Lavanya J and Gomathi N 'Synthesis and characterization of hybrid graphene' *ICRANN 2014, Jawaharlal Nehru University New Delhi 15-16, December 2014.*

2. Lavanya.J, Leena G. Nair, Neogi.S and Gomathi.N 'Study on RF plasma treated reduced graphene oxide' *Chemcon 2013, Indian Institute of Chemical Engineers (IIChE) Mumbai 27-30, December 2013.*

3. Lavanya J and Gomathi N 'Synthesis and characterization of nickel oxide/graphene sheet/graphene ribbon composite; I*nternational conference on emerging technologies: Micro to Nano 2015 Manipal university Jaipur 25-26, October 2015.*

Best poster award

1. Lavanya J and Gomathi N 'Synthesis and characterization of nickel oxide/graphene sheet/graphene ribbon composite; I*nternational conference on emerging technologies: Micro to Nano 2015 Manipal university Jaipur 25-26, October 2015.*